Summer 2017

An experimental study of the global and local flame features created by thermoacoustic instability

Jianan Zhang
University of Iowa

AN EXPERIMENTAL STUDY OF THE GLOBAL AND LOCAL FLAME FEATURES CREATED BY THERMOACOUSTIC INSTABILITY

by

Jianan Zhang

A thesis submitted in partial fulfillment
of the requirements for the Doctor of Philosophy
degree in Mechanical Engineering in the
Graduate College of
The University of Iowa

August 2017

Thesis Supervisor: Associate Professor Albert Ratner

Graduate College
The University of Iowa
Iowa City, Iowa

CERTIFICATE OF APPROVAL

_____

PH.D. THESIS

_____

This is to certify that the Ph.D. thesis of

Jianan Zhang

has been approved by the Examining Committee for
the thesis requirement for the Doctor of Philosophy degree
in Mechanical Engineering at the August 2017 graduation.

Thesis Committee:_____
Albert Ratner, Thesis Supervisor

_____
H.S. Udaykumar

_____
James H.J. Buchholz

_____
John A. Goree

_____
Pablo M. Carrica

ACKNOWLEDGEMENTS

First of all, I would like to express my sincere gratitude to my advisor Prof. Albert Ratner for his support of my Ph.D. study, for his patience, kindness, positive attitude, and expertise. I appreciate for all his guidance and help in my research at the University of Iowa. I also thank him for his encouragement whenever I encountered problems in my research and life.

I also would like to thank my committee members: Prof. H.S. Udaykumar, Prof. James Buchholz, Prof. John Goree, and Prof. Pablo Carrica, for their support, encouragement, and insightful comments. I appreciate their cooperation and help in my defense preparation.

I would like to acknowledge the current and prior group members in Prof. Ratner's lab: Tejasvi Sharma, Gurjap Singh, Kelsey Kaufman, Dr. Mohsen Ghamari, Matthew Panzer, Nate Wegger, and Dr. Majid Emadi, for all the pleasure time we have had together in the last five and half years.

I would like to acknowledge my family and my friends. I would like to thank my parents for their support of me in my entire life. I would also like to thank my parents-in-law for their help and support during the time of my graduation. In particular, I would like to thank my wife, Guiyan, for her love, support, and understanding in these years. I also thank my friends at the University of Iowa: Yuanming Luo and Dr. Jiajia Li.

Finally, I would like to thank the Department of Mechanical and Industrial Engineering at the University of Iowa. I appreciate the opportunity of working as a teaching assistant, which gives me a good understanding of how to teach and

communicate with students. I also thank the Graduate College for offering me a scholarship that helped me focus on my graduation preparation.

ABSTRACT

The current research focuses on the thermoacoustic instability of lean premixed combustion, which is a promising technique to inhibit Nitrogen Oxides (NOx) emission. Thermoacoustic instability describes the condition that the pressure oscillation is unusually high in the combustion device. It results from the coupling between pressure fluctuation and heat release oscillation, which experiences significant temporal and spatial variations. These variations are closely related to the flame shape deformation and critical in determining the trend of the global instability. Therefore, the current study aims to examine both the global and local flame features created by thermoacoustic instability.

The first part of the work is studying the unstable flame induced by artificial acoustic perturbation. The particular focus is on the global and local heat release rate oscillation. In the experiment, the global heat release rate oscillation was indicated by the hydroxyl (OH*) chemiluminescence captured with a photomultiplier tube (PMT). On the other hand, the flame shape and the local mean heat release rate were examined with flame surface density (FSD), which was calculated with the images captured with the planar laser-induced fluorescence of the hydroxide radical (OH-PLIF) method. The main analysis methods used in the current research are Rayleigh criterion and proper orthogonal decomposition (POD), which can efficiently capture the dominant oscillation mode of the flame.

The acoustic perturbation study first examined the effect of pressure variation (0.1 - 0.4 MPa) on the flame response to the acoustic perturbation. Results show that the elevated pressure intensifies the fundamental mode of heat release oscillation when the heat release oscillation is in phase with the pressure fluctuation; otherwise, the

fundamental oscillation tends to be inhibited. The pressure affects both the strength and the distribution of the local fundamental and the first harmonic oscillations. Furthermore, the effect of the pressure on the distribution is larger than that on the strength.

The study also investigated the role of Strouhal numbers in characterizing the flame oscillation induced by acoustic perturbation. Results show that the Strouhal number can characterize the changing trend of the oscillation amplitude, whereas the oscillation phase-delay is less dependent on the Strouhal number. The local analysis reveals that the nonlinear flame behavior results from the flame rollup induced by acoustic perturbation. Furthermore, the reconstruction of the global heat release shows that the cancellation of out-of-phase local oscillations can cause a low-level global oscillation. Results also demonstrate that the local heat release oscillation contains intense harmonic oscillations, which are closely associated with the flame rollup. However, the harmonic oscillation is less likely the main reason causing nonlinear flame behavior.

Besides the study with acoustic perturbation, the current study also conducted experimental and modeling studies on the self-excited thermoacoustic instability. The particular focus is examining the effects of hydrogen addition on the instability trend. Results demonstrate that the hydrogen concentration can affect both the oscillation frequency and amplitude. Pressure analysis shows that the low-frequency mode is triggered when the hydrogen concentration is low, whereas a high hydrogen concentration tends to excite a high-frequency mode. Moreover, the frequency tends to increase with an increasing hydrogen concentration. Modeling results illustrate that the change of the oscillation mode, which is determined by the turbulent flame speed, is mainly affected by the delay time between the heat release oscillation and the velocity

fluctuation. The modeling work shows that the one-dimensional model is not very efficient in capture the instability trend of the high-frequency mode. It may result from the lack of the knowledge of the mechanism of acoustic damping and flame dynamics.

PUBLIC ABSTRACT

The current research focuses on the thermoacoustic instability of lean premixed combustion, which is a promising technique to inhibit Nitrogen Oxides (NO_x) emission. Thermoacoustic instability describes the condition that the pressure oscillation is unusually high in the combustion device. It results from the coupling between pressure fluctuation and heat release oscillation, which experiences significant temporal and spatial variations. These variations are closely related to the flame shape deformation and critical in determining the trend of the global instability. Therefore, the current study aims to examine both the global and local flame features created by thermoacoustic instability.

The first part of the work is studying the unstable flame induced by artificial acoustic perturbation. The particular focus is on the global and local flame oscillation. The acoustic perturbation study shows that the elevated pressure can affect the flame shape deformation. The study also demonstrates that the Strouhal number can characterize the changing trend of the oscillation amplitude, whereas the oscillation phase-delay is less dependent on the Strouhal number.

Besides the study with acoustic perturbation, the current study also conducted experimental and modeling studies on the self-excited thermoacoustic instability. The particular focus is examining the effects of hydrogen addition on the instability trend. Results demonstrate that the hydrogen concentration can affect both the oscillation frequency and amplitude. Modeling results illustrate that the change of the oscillation mode, which is determined by the turbulent flame speed, is mainly affected by the delay time between the heat release oscillation and the velocity fluctuation.

TABLE OF CONTENTS

LIST OF TABLES

LIST OF FIGURES

NOMENCLATURE

ζ	Acoustic damping ratio	
ω	Angular frequency	rad/s
γ	Specific heat ratio	
τ	Time delay	s
ρ	Density	kg/m^3
ν	Kinematic viscosity	m^2/s
η_H	Hydrogen percentage	%
Σ	Flame surface density	mm^{-1}
φ	Phase	rad

$\vec{u}$	Velocity vector	
$\dot{m}$	Mass flow rate	kg/s
A^-	Complex amplitude of the upstream traveling wave	
A^+	Complex amplitude of the downstream traveling wave	
c	Speed of sound	m/s
c_p	Specific heat at constant pressure	J/(kg·K)
D	Burner inner diameter	m
e	Internal energy	J/kg
f	Frequency	Hz
g	Gravity acceleration	m/s^2
$\bar{h}$	Enthalpy	kJ/kmol

h	Convection heat transfer coefficient	$W/(m^2 \cdot K)$
H_l	Effective flame lift distance	m
K	Thermal conductivity	$W/(m \cdot K)$
k	Wavenumber	m^{-1}
L_c	Combustor chamber length	mm
l_f	Flame location	m
M	Mach number	
n	Flame gain	
Nu	Nusselt number	
P'	Pressure oscillation amplitude under atmospheric condition	pascal
p'	Pressure oscillation	pascal
P_A	Amplitude of the pressure oscillation under high pressure conditions	pascal
P_{atm}	Atmospheric pressure	pascal
P_c	Chamber pressure	pascal
Pr	Prandtl number	
q'	Heat release rate oscillation	J/m^3
Q'	Time-dependent heat release rate oscillation	J/m^3
q_A	Heat release oscillation amplitude	J/m^3
r	Radius of the tube	m
R^*	Non-dimensional Rayleigh Index	
Ra	Rayleigh number	
Re	Reynolds number	
S	Cross area of the tube	m^2

S_L	Laminar flame speed	m/s
S_T	Turbulent flame speed	m/s
St	Strouhal number	
t	Time	s
T	Temperature	K
T_b	Temperature of the burned gas	K
T_u	Temperature of the unburned gas	K
U	Bulk velocity	m/s
V	Volume	m^3

CHAPTER 1
INTRODUCTION

1.1 Background

Gas turbines are widely used in the electric power industry and transportation systems. For example, the electricity generated by gas turbine accounts for 27 percent of the total electricity produced in the United States. Unfortunately, gas turbines can produce a large amount of nitrogen oxides (NO_x) that are a major source of air pollution. NO_x can cause health and environmental problems and has been strictly regulated by emission laws. Great effort has been made by engineers and scientists to achieve the goal of an ultra-low level of NO_x emission. Because NO_x is formed during and after the combustion process, the combustor of gas turbines receives intensive attention. Research has revealed that there are three main sources of NO_x, which include thermal NO_x, fuel NO_x, and prompt NO_x. Among these sources, thermal NO_x is usually the major contributor to the total NO_x formation. To inhibit thermal NO_x, one of the most efficient methods used is decreasing the combustion temperature. When the combustion temperature is below 1300 °C, thermal NO_x can be significantly reduced.

Lean premixed combustion is an efficient technique to decrease the combustion temperature. The term of 'premixed' means that air and fuel have already been mixed before being supplied to the combustor. The term 'lean' indicates that the amount of air in the air-fuel mixture exceeds that needed for a stoichiometric reaction. The extra amount of air can actually be considered as a diluent, which absorbs the energy of combustion but does not contribute to the reaction. Lots of research has successfully demonstrated that by using lean premixed combustion, the combustion temperature can be controlled and the

NO_x emission can be subsequently reduced to an ultra-low level (several ppm). However, the application of lean premixed combustion in energy systems is still facing many technical challenges. One of the major challenges is thermoacoustic instability, which describes the situation that the pressure oscillation in the combustor is unusually high. Thermoacoustic instability can cause unsteady operating conditions that are detrimental to NO_x control. When the pressure oscillation is out of control, the local heat transfer can be significantly enhanced and consequently cause device failure [1].

Thermoacoustic instability results from the coupling between the heat release oscillation of the flame and the pressure fluctuation in the acoustic field. Researchers have discovered that the acoustic field can gain energy from the flame when the heat release oscillation is in phase with the pressure fluctuation. Thermoacoustic instability will result once the energy transferred into the acoustic field is larger than the energy losses of the acoustic field.

Because the flame is the only energy source that supports thermoacoustic instability, examination on the flame features is critical and necessary to understand the instability trend. The most important flame feature created by thermoacoustic instability is the heat release oscillation. Although tremendous experimental measurements and analytical modeling work have been conducted to examine the heat release oscillation, the mechanism of the instability trend is still not fully revealed.

The global heat release data is usually easy to measure, and it is useful in indicating the general instability trend. However, the global heat release result only provides limited information to reveal the instability mechanism. It is because that the

lean premixed flames, especially turbulent lean premixed flames, always experience a significant spatial variation. Figure 1.1 illustrates the examples showing the complex flame structure. The variation is related to the complex flame structure, which is caused by the highly turbulent and high pressure operating conditions in the combustor. Therefore, detailed examination on the local heat release oscillation is necessary to understand the global flame behavior and the instability mechanism. Although the local flame behavior is critical in understanding the global trend, only a very limited amount of work has been done on this topic. This is due to the difficulty of finding reliable measurement and data analysis methods. Investigation of both the global and local flame behavior can be a promising way to reveal the mechanism of the thermoacoustic instability in combustors using lean premixed techniques.

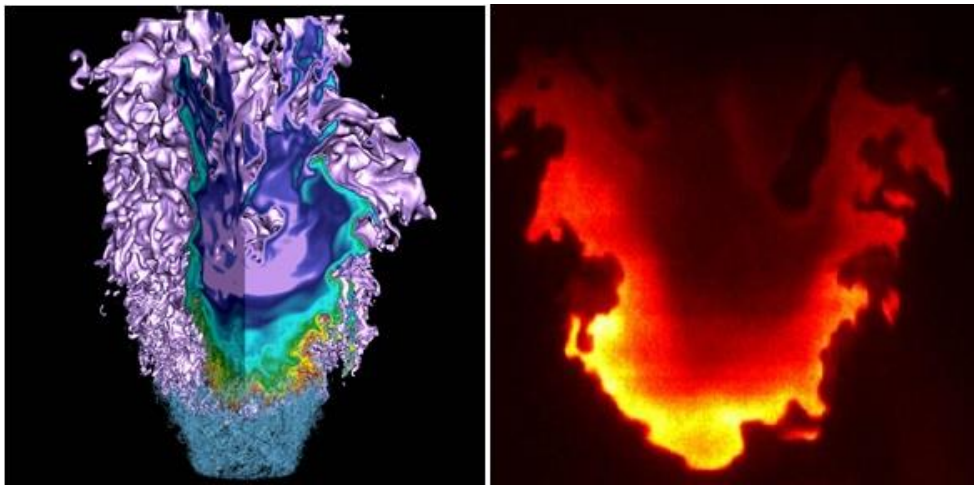

Figure 1.1. Profile of the concentration of OH molecules in a low swirl flame (simulation (left), experiment (right)).

The modeling work of thermoacoustic instability still relies on a simplified heat release model without considering flame features. Some successful work is limited to a

certain type of burner. It is hard to obtain general conclusion without considering the flame features.

1.2 Objectives and Outlines

The goal of the current research is to measure and understand the impact of thermoacoustic instability on the chemical and flow structures of premixed flames. The current research focuses on two topics, which are acoustically perturbed flames and the self-excited thermoacoustic instability. The research on the perturbed flame is aiming to examine the spatial and temporal variations of the flame. The particular focus is on the amplitude and phase of the global heat release rate oscillation, the amplitude and phase of the local oscillation, and the flame shape. To obtain the local information, a reliable local analysis method needs to be developed. Furthermore, bulk velocity and pressure are chosen as the main variables to build the bridge between the lab-scale study (low velocity, low pressure) and the realistic operating condition (high velocity, high pressure). The study on self-excited instability is for the purpose of understanding the coupling between the flame and the acoustical feature of the system. Furthermore, a modeling work is carried out to get an insight view of the effect of flame properties on the instability trend.

Chapter 1 will also present a literature review of the thermoacoustic instability related to large coherent structures, the effects of pressure on thermoacoustic instability, the global and local heat release measurement methods, and the modeling work on thermoacoustic instability. Chapter 2 introduces the experimental setup and the analysis methods. It gives a detailed description of the flame diagnostic methods that include

photomultiplier (PMT) and the planar laser-induced fluorescence of the hydroxide radical (OH-PLIF) method. Furthermore, it also examines the effect of pressure variation on the amplitude and phase of the global and local heat release oscillations. Part of the work presented in Chapter 2 is reproduced from our paper [2]. Chapter 3 investigates the local flame behaviors through Rayleigh criterion and a proper orthogonal decomposition (POD) method. Chapter 4 studies the global and local flame responses by changing the Strouhal number, which is characterized by the bulk velocity, the inner diameter of the burner, and the perturbation frequency. Chapter 4 is modified from our published work [3]. Chapter 5 presents an experimental and modeling work on self-excited thermoacoustic instability, which aims to understand the effect of flame features on thermoacoustic instability. Chapter 6 gives a short summary of the current research and a description of some proposed future work.

1.3 Introduction to Literature Review

The literature review first presents a general description of the thermoacoustic instability. In combustors, the heat release oscillation from the flame is the main source that transfers energy to the acoustic field. One common mechanism of heat release oscillation is related to the large coherent structures in the flow field. Therefore, the second part of the review focuses on the thermoacoustic instability related to the large coherent structures. The third part talks about the research of thermoacoustic instability under the elevated pressure condition. The fourth part presents the methods of measuring the global and the local heat release rate. The final part talks about the modeling work on the thermoacoustic instability.

1.4 A General Description of Thermoacoustic Instability

A common method for analyzing the thermoacoustic instability is Rayleigh criterion, which states that the thermoacoustic instability tends to be encouraged when the pressure oscillation and heat release fluctuation are in phase; otherwise, the instability will be damped [4]. The Rayleigh criterion can be expressed in an integral,

$$\int_{V_c}\int_{\xi} p'q'dtdV > 0 \tag{1.1}$$

where p' is the pressure oscillation, q' is the heat release oscillation, t is the time, V is the volume, ξ is the period of the oscillation, V_c is the combustor volume. Culick [5] has shown analytically that a positive Rayleigh Index indicates that the energy will transfer from flame to the acoustic field. The thermoacoustic instability will occur when the energy transferred into the acoustic field exceeds the energy losses from the acoustic field. Therefore, the energy gaining and damping mechanisms of the acoustic field are critical in determining the instability trend.

The main source that can transfer energy to the acoustic field is the unsteady heat release from the flame. The heat release oscillation can be induced by mass flow rate oscillation, equivalence ratio oscillation, and large coherent structures [1]. Mass flow rate and equivalence ratio oscillations can directly affect the amount of the fuel supplied to the system and consequently cause heat release oscillation. They usually result from the velocity fluctuation in fuel and air supply lines. Moreover, the insufficient mixing between fuel and air can also cause equivalence ratio oscillation [6]. In contrast, the large

coherent structure in flow field can induce heat release oscillation by inducing flame shape deformation [7].

The energy damping/dissipation of unstable acoustic field is related to the heat loss due to heat transfer and friction caused by viscous [8]. Furthermore, the energy exchange among different acoustic oscillation modes can also cause the energy damping of a particular oscillation mode [1]. In real systems, the energy dissipation is still hard to quantify with reliable techniques.

The current study will not focus on the mass flow rate oscillation and equivalence ratio oscillation, which play relatively minor roles in affecting the instability trend of lean premixed systems. Moreover, the effect of energy damping is out of the current scope. The following sections will mainly discuss the heat release oscillation related to coherent structures and related diagnostic and modeling work.

1.5 Heat Release Oscillation Induced by Large Coherent Structures

1.5.1 Non-swirling Flames

Non-swirling flames have a relatively simple shape, which gives researchers a great advantage in understanding the basic features of thermoacoustic instability. Researchers have investigated both self-excited and artificially triggered thermoacoustic instability.

Generally, the coherent structures in non-swirl burners are triggered by the shear layer instability [7, 9, 10]. Both low-frequency (< 1000 Hz) and high-frequency (> 1000 Hz) pressure oscillations have been detected in the self-excited thermoacoustic instability.

Low-frequency pressure oscillations are associated with the acoustic modes of the combustor. Smith and Zukoski [11] studied the thermoacoustic instability with a two-dimensional combustor. Notable pressure oscillations can be detected when large coherent structures generate with the frequency that is close to the acoustic mode. A similar phenomenon is also described by Candel [12] and Schadow et al. [13]. High-frequency pressure oscillations are directly related to the vortex shedding process. Rogers and Marble [14] show that high-frequency pressure pulses can be directly generated by the coupling between vortex formation and combustion. The phase delay between vortex formation and flame oscillation is critical in determining the oscillation trend. Figure 1.2 shows Schlieren images indicating that the large coherent structures are formed under the unstable conditions.

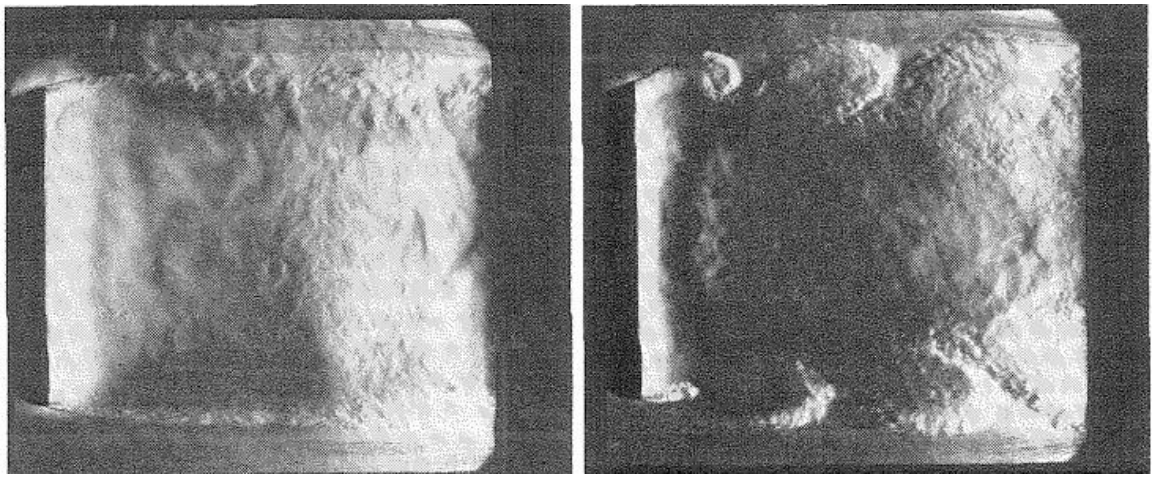

Figure 1.2. Schlieren images show the case under stable (left) and unstable (right) conditions (reproduced from [14]).

The method of using artificial perturbation is also widely used to study the thermoacoustic instability. Using a two-dimensional dump combustor, Mcmanus et al. [9] demonstrate that the vortex-induced heat release oscillation depends on the forcing frequency and amplitude. However, limited by the diagnostic technique, detailed

information about flame is not provided in the early stage of the study. Until in recent years, the local flame structure can be examined in detail with the development of using the laser in flame measurement. Shanbhogue et al. [15] used Mie scattering and PIV to show that artificial acoustic perturbation can induce vortices, which cause the flame shape deformation (shown in Figure 1.3).

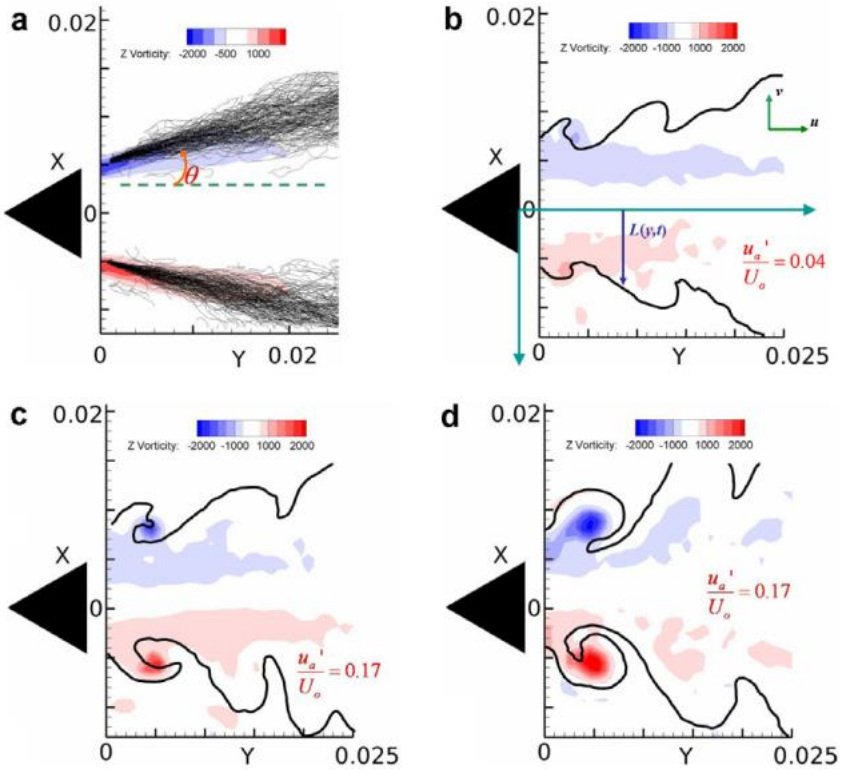

Figure 1.3. Instantaneous images of the flame-front (obtained from Mie scattering images) and vorticity field (calculated from PIV results) (a) without excitation and (b–d) with increasing amplitudes of excitation (reproduced from [15]).

Balachandran et al. [16] studied the flame response to acoustic perturbation with a circular bluff-body combustor. The flame response to velocity oscillation is found to be nonlinear, which is closely related to the flame roll-up process induced by the vortex formed in the shear layer. The flame-vortex interaction has been further examined with simulation conducted by Armitage at al. [17]. One of the results is illustrated in

Figure 1.4 to show the flame shape deformation induced by vortices formed in the shear layer.

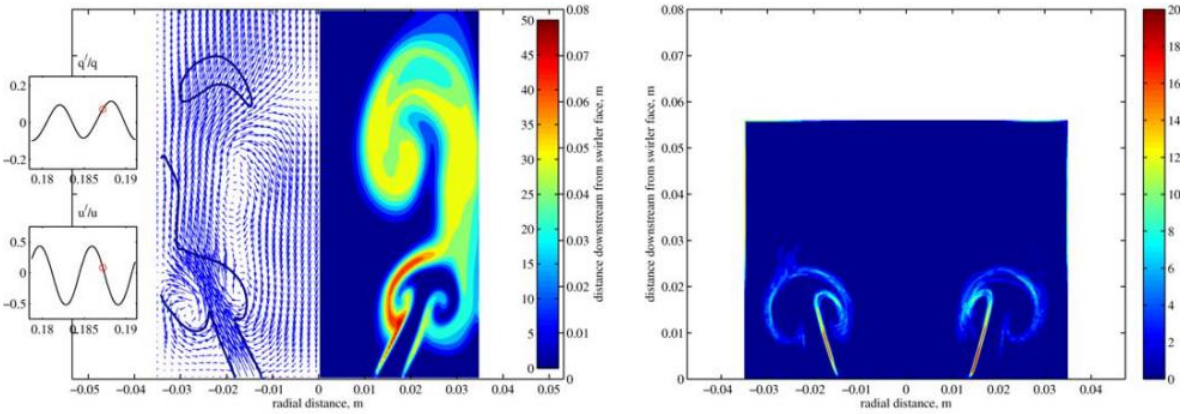

Figure 1.4. Snapshots of (a) velocity vectors and heat release from CFD and (b) phase-averaged flame surface density images from experiments (reproduced from [17]).

1.5.2 Swirling Flames

Because gas turbines widely use swirl burners to stabilize the flame, a considerable amount of work has been conducted on the thermoacoustic instability of swirling flames. For swirling flow, the problem is more complex because of the appearance of the helical and centrifugal instability [18, 19]. The swirl number, the burner geometry, and the operation condition can all impact the type of coherent structures [20], which subsequently affects the way of the flame deformation.

Both experimental and numerical studies have shown that the swirl number is one of the most important parameters that affect the type of vortex [18, 21, 22]. For burners with a swirl number less than 0.6, ring-like vortices are often detected once the system is unstable [23, 24]. It is because the vortex is still mainly induced by shear layer instability. As a result, the flame oscillation is usually quasi-symmetric around the center of the

burner [25]. In contrast, helical vortices are commonly formed in high swirl burners [24, 26, 27], which can cause asymmetric flame front oscillation. One of the examples showing the helical oscillation is shown in Figure 1.5.

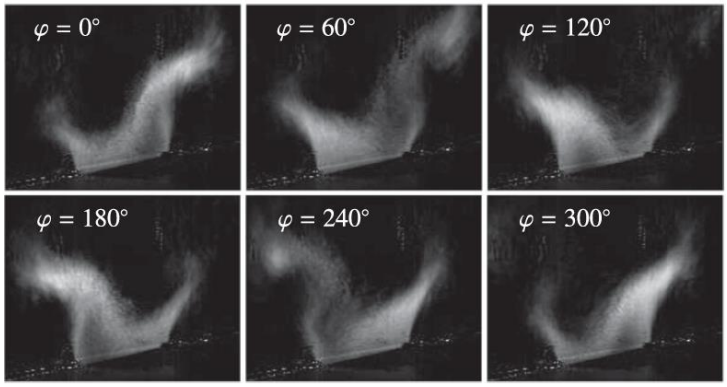

Figure 1.5. The evidence of the processing vortex core in a swirling burner (reproduced from reference [27]).

The type of the coherent structure is also dependent on the burner geometry, even for the burners with similar swirl numbers. As shown in A large eddy simulation of GE LM6000 combustor injector shows ring-like coherent structures in low swirl (Swirl number = 0.56) flow [1], whereas helical structures are found in the simulation of a centerbody swirling injector with a swirl number of 0.44 [28].

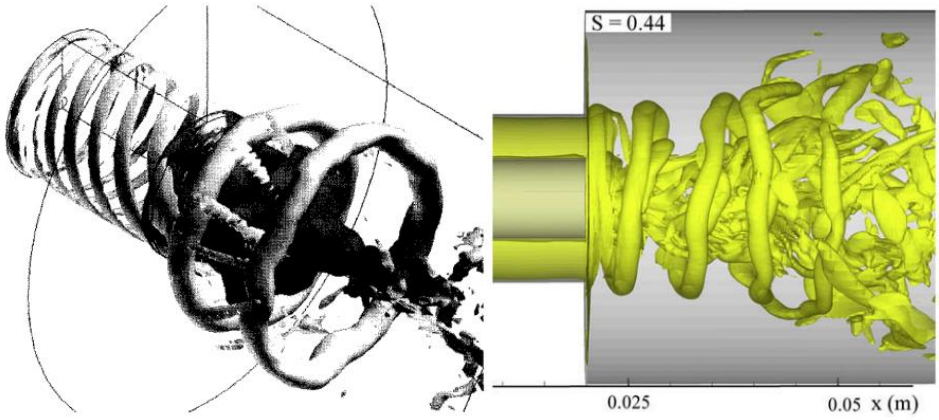

Figure 1.6. The vortex structure of burners without center-body (left, reproduced from [1]) and with center-body (right [28]).

Operating condition is another factor that impacts the vortices behavior. For the same swirl burner, semi-symmetric toroidal vortices dominate the flow in the cases with low power and high equivalence ratios; otherwise, helical coherent structures play a governing role [29].

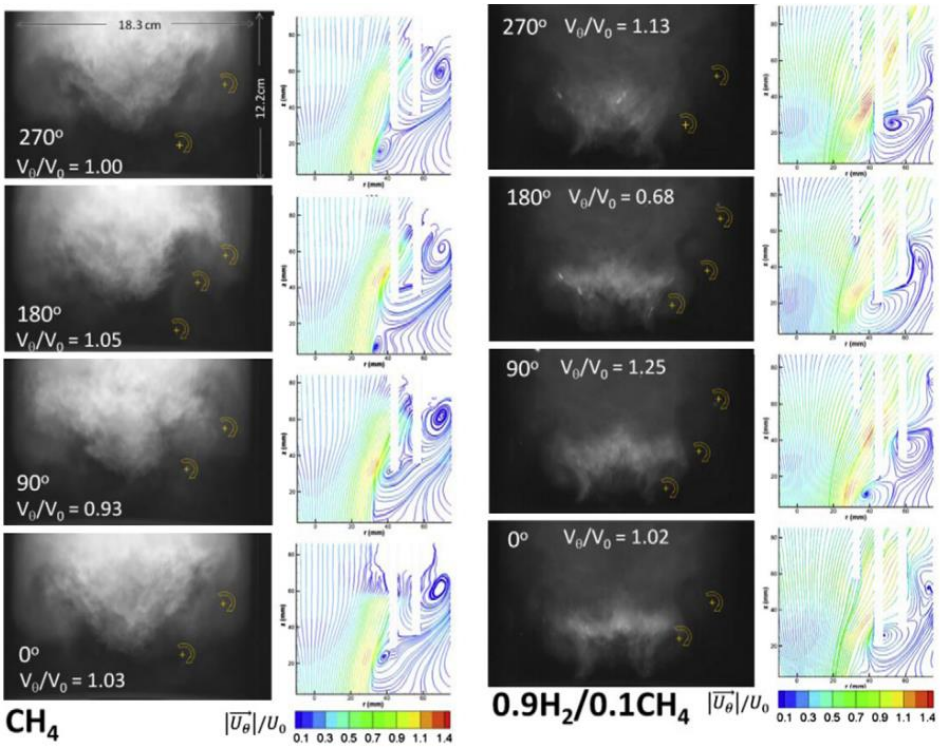

Figure 1.7. Effects of hydrogen addition on the flame shape and flow field (reproduce from [23]).

Moreover, the variation of the fuel property can change the flame structure, which subsequently affects vortex behaviors. Davis, et al. [23] found that hydrogen addition could significantly change the flame shape and consequently change the movement of the vortex. As shown in Figure 1.7, for pure methane flame, the flame is attached to the chamber wall, so the vortex is trapped below the flame edge. In contrast, the flame size decreases when hydrogen is added, and there is no flame-wall interaction. As a result, the

vortex can travel through the gap between the flame brush and the wall, which consequently induced a more intense flame oscillation.

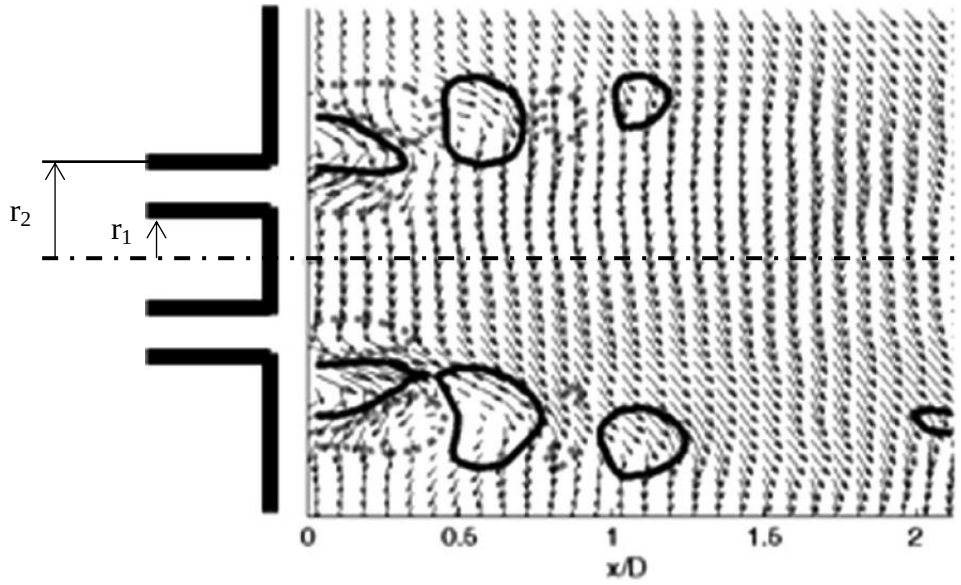

Figure 1.8. Velocity field and vorticity isocontours in a combustor perturbed by the acoustic forcing with an angular frequency $\omega = 1600\pi$. The dotted and solid vorticity isocontours represent values of $\omega U_0/(r_2 - r_1) = -0.1$ and 0.1, respectively (reproduced from [30]).

In addition to examining naturally occurring vortex-related combustion instability, the acoustic perturbation is also frequently applied to study swirling flames. O'Connor and Lieuwen have shown that vortices can be triggered by acoustic forcing [30] (shown in Figure 1.8). The behavior of coherent vortices is found to be sensitive to the perturbation frequency, the perturbation type, and the perturbation level. Vortex induced flame oscillation is only found in a certain frequency range [25, 31]. The vortices formed in the shear layer shrink in size when perturbation frequency increases in both non-reacting and reacting flows [30]. An experiment with a stratified swirl burner demonstrates that the flame rollup is only found in the high-frequency perturbation cases with a sufficient strength [32]. The longitudinal forcing can inhibit the asymmetric

oscillations in the flame [33], whereas the transverse perturbation still causes symmetric oscillation [30].

Some experimental work successfully inhibited the thermoacoustic instability with the knowledge that the flame-vortex interaction is critical in triggering the instability. Therkelsen, et al. [34] has demonstrated that the use of a divergent quarl can significantly inhibit the pressure oscillation in the combustor. It is because the quarl can destroy the formation of the vortex in the shear layer. Paschereit [35], et al. changed the pilot burner geometry to stabilize the vortex breakdown location, which consequently eliminated the thermoacoustic instability that used to happen during engine start-up. Moreover, work of Meadows and Agrawal shows that the acoustic oscillation can be weakened by adding a porous inert at the recirculation region, which prevents the formation of large coherent structures.

1.6 Thermoacoustic Instability Study under Elevated Pressure Conditions

General studies on the effect of pressure on lean premixed flame show that pressure can directly cause flame wrinkling [36] and change the turbulent burning velocity [37]. The pressure is always elevated in gas turbine combustors, so it is necessary to examine the effect of pressure on heat release oscillation. However, the research on unstable flame under elevated pressure conditions is still very limited.

The elevated pressure can affect the vortex formation mechanism. Using a dual-swirl burner, Boxx et al. [38] show that the processing vortex core, which appears in the atmospheric condition, cannot be detected when the pressure is elevated to 5 bar. Bunce et al. [39] and Cheung et al. [40] examined the effect of pressure on the flame transfer

function (FTF), which is defined as the ratio between the normalized heat release oscillation and the normalized artificial perturbation. Both of them conclude that pressure only has a limited effect on the general trend of the FTF. However, the amplitude and phase of the heat release oscillations at particular frequencies can be significantly changed. It implies that the elevated pressure can play a critical role in determining the instability trend. Yun [41] studied the effect of pressure elevation on the thermoacoustic instability of a low swirl burner. The Rayleigh criterion analysis shows that the flame-acoustic coupling is still Strouhal number dependent.

1.7 Diagnostic Methods of Heat Release Rate

1.7.1 Global Heat Release Rate Measurement

For lean premixed flames, the most common method of global heat release measurement is using OH*, CH*, or CO_2* chemiluminescence (here the * represents the electronically excited state) [42].

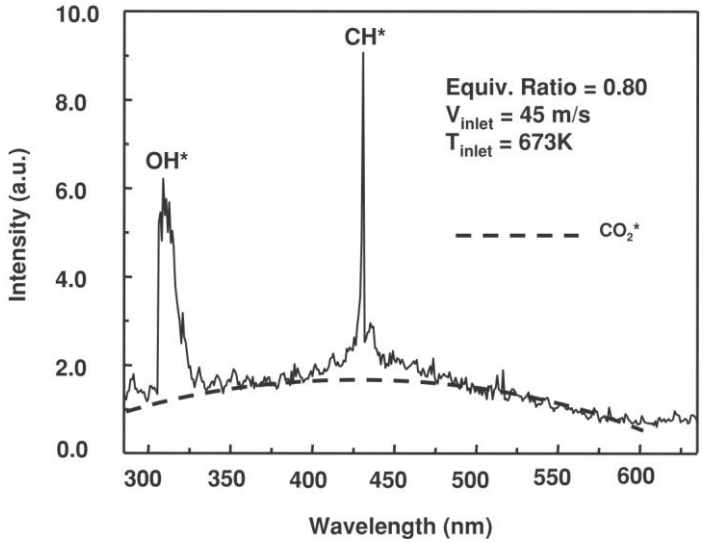

Figure 1.9. Chemiluminescence-emission spectrum from a lean premixed flame (reproduced from [1]).

Figure 1.9 shows the spectrum of the chemiluminescence from a lean premixed flame [42]. The wavelength of OH* is centered at 309 nm, whereas the wavelength of CH* is centered at 431 nm. CO_2* exists in a broadband range (350 – 600 nm). OH* is produced by the reaction $CH + O_2 \rightarrow CO + OH^*$ [43], CH* is from the reaction $C_2H + O \rightarrow CH^* + CO$, and CO_2* is generated from the reaction $CO + O + M \rightarrow CO_2^* + M$ [44].

The chemiluminescence signal can be acquired by the photomultiplier tube (PMT) equipped with a narrow-band optic filter [32, 45]. The chemiluminescence of different radicals can also be recorded with the camera equipped with optic filters [43, 46]. The sampling rate of the chemiluminescence is only dependent on the rate of the device, which can be easily above 10 kHz. It gives a good time resolution of the heat release oscillation.

1.7.2 Local Heat Release Rate Measurement

The local heat release measurement is more difficult than the global one because of the complex structure of flames. The non-intrusive measurement is the only way to obtain the local heat release information. The local heat release rate is dependent on the local equivalence ratio, the local temperature, local turbulence level and strain rates, etc. [44, 47]. Therefore, careful attention should be paid when the local information is needed.

Line-of-sight measurement of OH* or CH* chemiluminescence with the camera is widely used to obtain the quasi-local information. With the assumption that the flame is symmetric, Abel transform can be applied to chemiluminescence images to obtain the local information [6, 45, 48]. Although the chemiluminescence measurement is simple, the line-of-sight method is not appropriate when the flame oscillation is asymmetric.

To directly capture local flame information, the planar laser-induced fluorescence (PLIF) method is often employed to acquire a cross-sectional view of the flame. The PLIF system uses the laser beam to excite the interested electronic absorption in specific species. The electronically excited state of the species is not stable. When the species change from the excited state back to a lower electronic state, it will emit fluorescence. The emitted fluorescence can be subsequently captured with cameras equipped with band-filtered lens [49].

Direct heat release measurement using simultaneously CH_2O and OH PLIF is believed to be an accurate method to obtain the local heat release rate [16, 47]. It is because that the reaction of CH_2O and OH ($CH_2O + OH \rightarrow HCO + H_2O$) is the main source for producing HCO, which is closed related to the heat release. When the temperature variation is not significant, the product of the CH2O and OH fluorescence is proportional to the reaction rate. However, this measurement method needs two independent laser systems, which is complicated and expensive.

Another common PLIF methods used for studying unsteady flame is OH-PLIF [50]. OH is a radical that participates in many critical reactions in hydrocarbon flames. However, OH fluorescence intensity cannot be directly used to represent the local heat release rate because of its long-life characteristic [47, 51]. However, it has been experimentally proven that OH-PLIF can be utilized to reasonably identify the flame front based on the OH fluorescence gradient [43, 52]. Once the flame front is detected, flame surface density (FSD), which is directly related to the local mean heat release rate, can be obtained [53-57]. It has been shown with chemiluminescence and direct local heat

release imaging (simultaneous OH and CH_2O PLIF) measurements that FSD can qualitatively represent the mean local heat release rate [16, 43, 58].

In recent years, benefited from the development of high-speed lasers, measures on high-speed local heat release rate have been conducted to examine the heat release oscillation with high time-resolution. Allison et.al. [55] concluded that the flame surface density calculated from high-speed CH_2O PLIF can not only capture the dominant oscillation frequency but also the local heat release distribution.

The work on local heat release measurement is based on 1D or 2D diagnostic methods. Three-dimensional (3D) diagnostic methods are developed in recent years for 3D flame structure measurement [59]. Although 3D measurement shows some promising results of the flame structure, its reliability still needs more data to support. In the future, it can be predicted that reliable 3D diagnostic method can significantly prompt the understanding the relationship between flame structure and heat release rate.

1.8 Thermoacoustic Instability Modeling

Numerical and analytical work on thermoacoustic instability is also essential to understand the problem. The analytical work provides models to demonstrate the general thermoacoustic features under simplified conditions. In contrast, computational Fluid Dynamics (CFD) methods are used to consider complex combustor geometries, high-turbulent and high-pressure operating conditions, and detailed chemical reactions. Limited by the current research scope, the review will only focus on the analytical work on thermoacoustic instability. Based on the heat release model, there are roughly two types of approach toward analytical modeling. The first one neglects the flame structure

and treats the flame as a flat surface, whereas the other considers the simplified flame structure.

1.8.1 Modeling Work with a Minor Consideration of the Flame Structure

There are two types of modeling work that ignore the detailed flame structure; one is the zero-dimensional model (a Helmholtz resonator), and the other one is one-dimensional that only considers the longitudinal mode.

The zero-dimensional model works with the assumption that: 1) the flow is one-dimensional and incompressible, 2) the gas is inviscid and behaves as an ideal gas, 3) all variables in the control volume has negligible variations [8, 60]. The governing equation for the model is [8],

$$\frac{d^2 p'}{dt^2} + 2\zeta\omega \frac{dp'}{dt} + \omega^2 p' = \frac{\gamma - 1}{V} \frac{dq'}{dt} \tag{1.2}$$

where p' is the pressure oscillation, t is the time, ζ is the damping ratio, ω is the angular frequency, q' is the heat release rate oscillation, γ is the ratio of the specific heats, and V is the volume of the combustor. This model is useful for combustors whose inlet and outlet are connecting with small-size ducts [8, 61].

The flat flame assumption is widely used in the one-dimensional (1D) thermoacoustic analysis. 1D model has been proven to be efficient in detecting the acoustic modes associated with the combustor geometry [62]. In the 1D model, the flat flame is simplified further to a point. The 1D analysis is modified from the 1D acoustic model by considering the effect of heat addition on the acoustic feature of combustors. Poinsot, et. al. [7, 63] used a 1D model to calculate the acoustic modes of the combustion

system. Although the heat release from the flame is not directly modeled in their work, they considered the effect of flame on the system by including the temperature gradient. Their work demonstrated that the classical acoustic model could still capture the dominant acoustic modes. Dowling and Stow [64] have shown that the heat release oscillation $q'(x,t)$ can be introduced to the 1D model with the form,

$$q'(x,t) = Q'\delta(x - l_f) \tag{1.3}$$

where Q' is the time-dependent heat release oscillation and l_f is the flame location. They also demonstrate that the temperature gradient induced by flame needs to be considered to capture the instability trend.

The heat release oscillation can be related to velocity oscillation by a popular n-τ model [63],

$$Q' = \dot{Q}nu'(x,t-\tau) \tag{1.4}$$

where $\dot{Q}$ is the heat release rate per unit volume, n is the flame gain that is related to oscillation amplitude, and τ is the time delay between heat release oscillation and velocity fluctuation.

The advantage of Helmholtz resonator and 1D models is their fast response. However, a reliable prediction with these models needs accurate information of the flame gain (n) and time delay (τ), which need detailed tests of the flame transfer function (FTF). The FTF is known to be closely related to the flame structure, which is sensitive to the burner geometry, the fuel type, the operating condition, et al. Unfortunately, it is

extremely difficult to test the FTF under practical operating conditions. To solve this problem, the heat release oscillation models considering flame structure oscillation are developed to give an insight view of the flame oscillation mechanism.

1.8.2 Modeling Working Considering the Flame Structure

The most successful work on flame shape oscillation is related to the laminar flame [65-68]. The success of the modeling work on laminar flames is credited with the application of G-equation to compute the flame front movement. The G-equation stands for is defined as [69],

$$\frac{\partial G}{\partial t} + \vec{u} \cdot \nabla G = S_L \left| \nabla G \right| \tag{1.5}$$

where the flame front position is defined as $G(\vec{x}, t) = 0$, $\vec{u}$ represents the flow field, and S_L is the laminar burner velocity of the flame. For laminar flames that have a relatively simple shape, the equation of $G(\vec{x}, t) = 0$ can be accurately defined. As a result, the FTF computed with G-equation models shows an excellent agreement with the experiment result [65].

Since a successful application of the G-equation in laminar flames, turbulent flame modeling employed the similar idea with the consideration of the effect of turbulence [21, 70]. However, the modeling work on turbulent flame is still facing many challenges. One of the most significant challenges is the determination of the local turbulent burning velocity, which could experience significant spatial variation because it is affected by the local turbulence intensity, the local temperature field, and the local

equivalence ratio, et al. [71]. In fact, there is still no reliable model for computing the turbulent burner velocity of lean premixed flames.

Another limitation of the working using G-equation analysis is that it mainly focuses on the linear flame response to pressure oscillations. However, the nonlinear flame behavior caused by large-scale structures in the flow field is still not fully examined. Since the flame-vortex interaction is heavily dependent on the flow field, LES is still playing the dominant role in the relative research [28].

CHAPTER 2
EFFECT OF THE ELEVATED PRESSURE ON THE FLAME RESPONSE TO ACOUSTIC PERTURBATION

In this chapter, we investigated effects of the elevated pressure on the local and the global flame responses to acoustic perturbation. One of the major challenges faced by thermoacoustic instability research is that the practical systems are operating under high-pressure conditions, whereas most laboratory study is under the atmospheric condition. The elevated pressure can significantly change flame characteristics; for example, the flame front wrinkling is enhanced under the high-pressure condition. Unfortunately, there are only a few studies on thermoacoustic instability under elevated pressure conditions. The current study focuses on the effect of the elevated pressure on the global and local flame oscillation features induced by acoustic perturbation.

2.1 Experimental Configuration

The experimental system is schematically shown in Figure 2.1. The major part of the system is an acoustic chamber that enables perturbation of the flame with the designed frequency and amplitude. Figure 2.1 also shows the flow control system and the diagnostic facilities.

2.1.1 Acoustic Chamber

The photo of the acoustic chamber is illustrated in Figure 2.2. The acoustic chamber comprises a vertical part and a horizontal part. The vertical chamber has a height of 1850 mm and an inner diameter of 300 mm. Three electrically adjustable valves that are located at the downstream of the chamber can adjust the chamber pressure. A low swirl burner (LSB) is mounted to the bottom of the vertical chamber. Quartz windows

used for optical measurement are installed in the wall near the bottom of the vertical chamber.

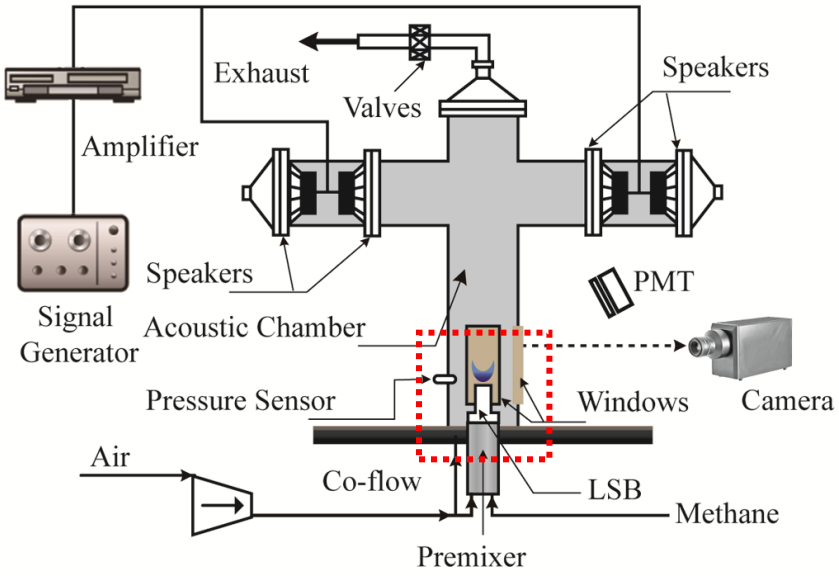

(a)

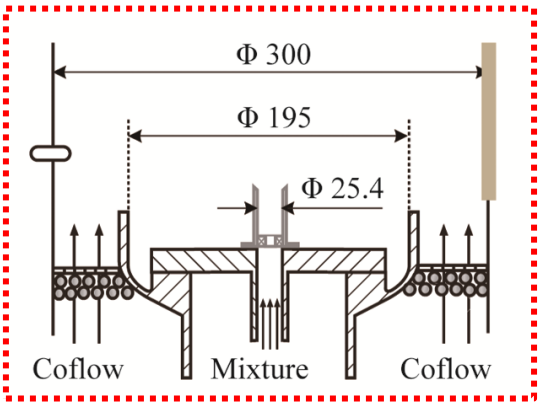

(b)

Figure 2.1. (a) Schematic view of the experiment setup, (b) the detailed geometry of the section marked with a dashed box in (a).

Four loudspeakers, which are mounted in the horizontal chamber, are used to supply in-phase acoustic perturbation from the downstream of the burner. During the test, a signal generator generated a continuous sinusoidal signal that inputs to a power

amplifier, which powers the four speakers with the designed frequency and amplitude. With the symmetric layout shown in Figure 2.1, the pressure oscillation near the burner is approximately a longitudinal wave with a minor variation in the radial direction. Moreover, the frequency used in the current research is relatively low (< 120 Hz), which results in a long wavelength (> 2 m). Considering the flame length (~ 5 cm) is much shorter than the pressure wavelength, the spatial variation of the pressure oscillation near the flame is assumed to be small and negligible. During the tests, the nitrogen gas from liquid nitrogen tank was used to prevent overheating of the speaker.

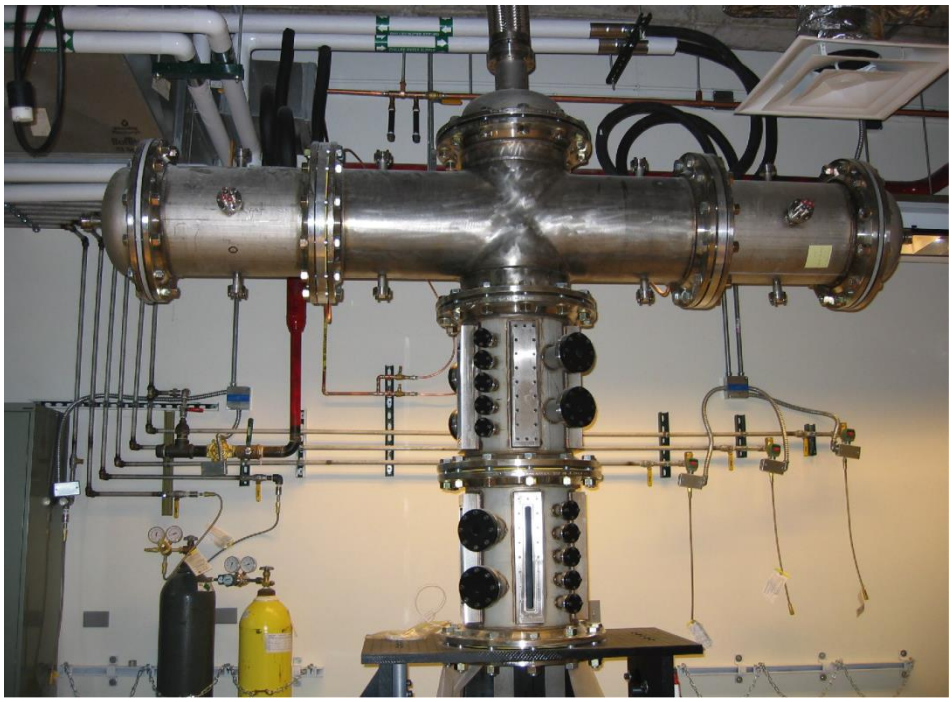

Figure 2.2. The acoustic chamber.

2.1.2 Burner and Flow Control System

The LSB, which is designed by Robert Cheng from Lawrence Berkeley National Laboratory, is used in the current research. The LSB has a swirl number of 0.5 and an inner diameter of 25.4 mm. It has been shown experimentally that this burner is capable

of ultra-low NOx operation (several ppm) [72]. In contrast to high swirl burners that stabilize combustion by recirculating hot burnt gas, low swirl burners stabilize the flame with a divergent flow field [73].

Air and fuel (methane) flows are controlled with Hastings flow controllers with an accuracy of 0.2% of full scale plus 0.5% of reading values. Before entering the burner, air and methane are premixed in a pipe containing a 50 mm-thick layer of small metal balls followed by a honeycomb mesh. In the current study, fuel and air are considered as fully mixed, so the equivalence ratio oscillation is neglected. Co-flow, with a velocity of approximately 1 m/s, is provided near the chamber wall to supply thermal shielding for the chamber and to dilute the combustion products downstream of the testing region.

2.1.3 Diagnostic Methods

A piezoelectric pressure sensor (PCB 106B) is installed in the chamber wall, at a position of 127 mm above the plate on which the LSB is mounted. The pressure oscillation is measured with a sampling rate of 20 kHz.

The global heat release rate is indicated with the OH* chemiluminescence captured by a photomultiplier tube (PMT) (Hamamatsu H8249-101) equipped with an bandpass ultraviolet (UV) filter (308 ± 10nm). The sampling rate of the PMT is 20 kHz to ensure a good time-resolution of the OH* chemiluminescence data.

The current study used an OH-PLIF technique to examine the local flame features. Figure 2.3 shows the OH-PLIF system, a Nd:YAG laser (Continuum Powerlite 9010), which supplies a 532 nm beam at 10 Hz, is used to pump a dye laser (Continuum ND6000) to product a 564 nm beam. Finally, a ultraviolet (UV) beam with a wavelength of 283 nm is used for exciting the A-X(1, 0) band of OH radical. The energy of the UV

beam in use is approximately 30 mJ/pulse. An ICCD (Intensified Charge-coupled Device) camera (Princeton Instruments) equipped with a narrow bandpass filter (312.6 nm ± 10 nm) is utilized to capture the distribution of OH radicals. The ICCD camera is set to capture images in an 80 mm × 80 mm region with a resolution of 512 × 512 pixels. In the data analysis process, only a 60 mm × 80 mm region is used because the flame length is less than 60 mm in the current tests. The ICCD camera is set to take pictures with an average frequency of 3 Hz and a gate time of 150 ns. The gate pulse signal from the camera is recorded simultaneously with the pressure signal.

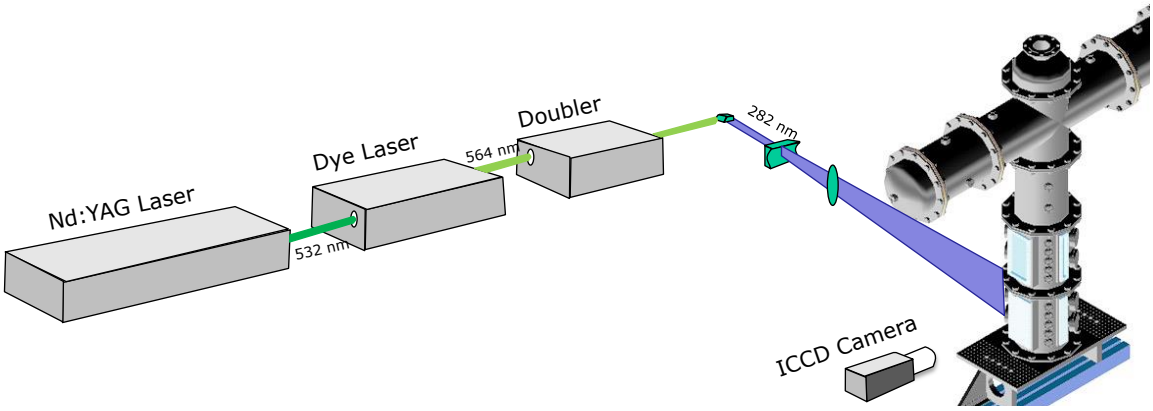

Figure 2.3. Schematic of the OH-PLIF system.

2.2 Data Analyzing Methods

2.2.1 Phase-average Method

To capture the oscillation trend of the flame, the diagnostic method usually needs a good time-resolution. For example, if the oscillation frequency is around 125 Hz, the measurement should have at least a sampling rate of 250 Hz to capture the oscillation trend. However, the current local measurement only has a rate of 3 Hz that is impossible to capture the oscillation independently. Therefore, a phase-averaged method is used with the assistance of the pressure signal to examine the flame oscillation.

The most important assumption of this method is that the dominant flame features are dependent on the phase angle of the pressure. Therefore, averaging all images at the same phase angle of the pressure can capture the dominant flame oscillation trend. In the current study, the camera gate signal and the pressure signal were saved simultaneously. The phase angle of each image can subsequently be determined by calculating the phase angle at which the image was captured.

2.2.2 Flame Surface Density

The OH fluorescence intensity is weakly related to the local heat release rate because OH radicals can be found in both the flame front and the burnt gas [30, 31]. However, OH-PLIF images can be used to detect the flame front, which can subsequently be used to calculate the flame surface density (FSD) that is directly related to the local mean heat release rate [13, 32, 33].

Figure 2.4 shows the steps of calculating FSD. The edge of the flame was first detected by a Canny method provided in Matlab Figure 2.4(a). The detected edges were then filtered with OH fluorescence and OH gradient thresholds that were set as 45% and 45% of the corresponding maximum values, respectively Figure 2.4(b-d). The local flame surface density was then calculated with a procedure similar to that described in Lee's work [43]. At different locations in the flame, the flame length in a small window (10 × 10 pixels, approximately 1.6 mm ×1.6 mm) was first calculated. The local FSD was then computed by dividing the total flame length in the window by the window area. With the simultaneously captured camera gate time and pressure signals, the phase angle of each image with respect to the pressure signal was determined. The FSD images were then

distributed to each 30-degree-wide phase bin, which results in approximately 200 images in each phase bin. Finally, the results in each phase bin were averaged to create a phase-averaged image Figure 2.4(e).

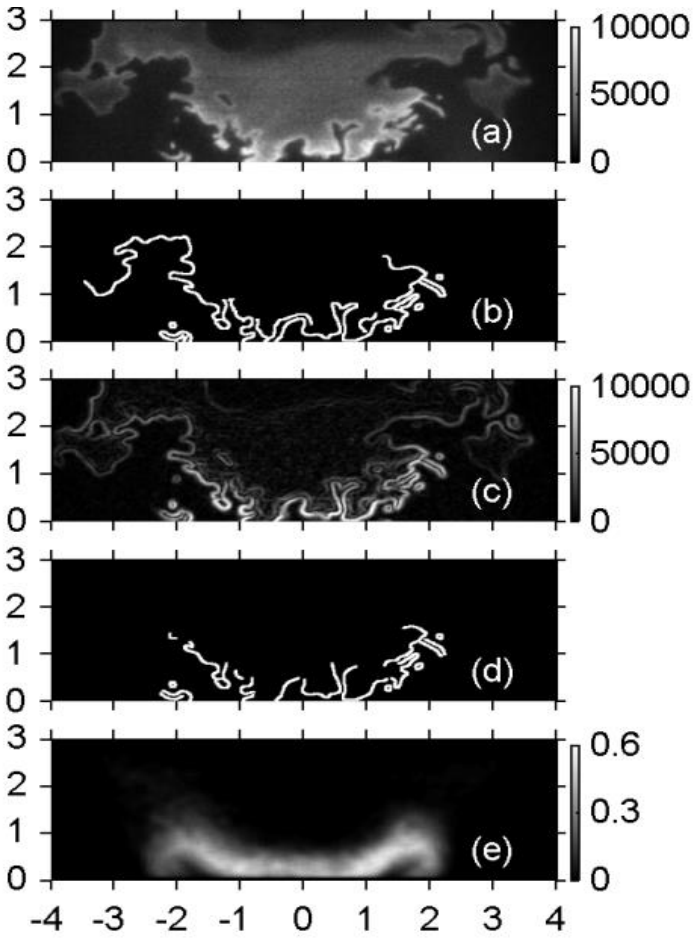

Figure 2.4. The steps of calculating FSD.

2.2.3 Local Analysis

The phase-averaged method and flame surface density are employed to obtain the local heat release rate distribution, and following that, a simple curve fitting method to compute the oscillation amplitude and phase of the local heat release rate. The current fitting sinusoidal functions applied to the phase-averaged FSD results are $A_1 \sin(2\pi f_1 t + \varphi_1) + A_2 \sin(2\pi f_2 t + \varphi_2)$, where A, f, and φ represent the amplitude, the

frequency, and the phase of the local oscillation, respectively. The subscripts *1* and *2* denote the fundamental mode and the first harmonic mode, respectively. A Gauss-Newton method was utilized to find the best curve fitting coefficients based on the least square rule. In the current study, the uncertainty of the fundamental mode is less than 8%, whereas the uncertainty of the harmonic mode is no larger than 20%.

2.3 Operating Conditions

The operating conditions are listed in Table 2.1, in which 0.1 MPa stands for the atmospheric pressure.

Table 2.1. Operating conditions

Pressure (MPa)	Forcing frequency (Hz)	P_A/P_c (%)
0.1	61	0.03 - 0.58
	86	0.02 - 0.56
	115	0.03 - 0.51
0.2	61	0.03 - 0.55
	86	0.05 - 0.37
	115	0.04 - 0.59
0.3	61	0.05 - 0.48
	86	0.04 - 0.33
	115	0.02 - 0.43
0.4	61	0.03 - 0.34
	86	0.04 - 0.32
	115	0.03 - 0.24

In all tests, the equivalence ratio and the bulk velocity were kept at 0.7 and 3 m/s, respectively. The prior work of Huang [31] and Kang [74] demonstrates that the flame shows different scales of shape deformation when the frequency changes in the range of 40 Hz – 135 Hz. Therefore, the current study chose three different forcing frequencies, which are 61 Hz, 86 Hz, and 115 Hz, to ensure the flame front experienced a notable deformation. The forcing amplitude increased until the global flame response shows nonlinear behaviors. The forcing amplitude (P_A/Pc) is calculated by normalizing the amplitude of the pressure fluctuation (P_A) with the chamber pressure (Pc).

2.4 Results

2.4.1 Global Flame Response

The OH* chemiluminescence signals were processed with the fast Fourier transform (FFT) method. In the current study, the flame fluctuation was induced by the artificial acoustic perturbation. The power spectral density (POD) was calculated with the Welch method to determine the dominant oscillation frequencies.

Figure 2.5 shows the PSD of the OH* signal and the phase-averaged OH* results. The frequency resolution is 0.05 Hz. It can be seen in Figure 2.5 that all cases have a strong mode at the perturbation frequency. Therefore, the perturbation frequency (f) is referred to as the fundamental frequency in the following sections. It can also be detected that the spectrum contains not only the fundamental mode but also the harmonic modes. A low-frequency mode (approximately 5.6 Hz) with an unchanging amplitude (-1 (a. u.)) can also be detected in all cases. It is related to the breathing mode of the burner, which depends on the bulk velocity and the burner geometry. Because the perturbation level is

very low (< 0.6% of the mean pressure), the amplitude of the breathing mode shows a comparable level with that of the fundamental mode.

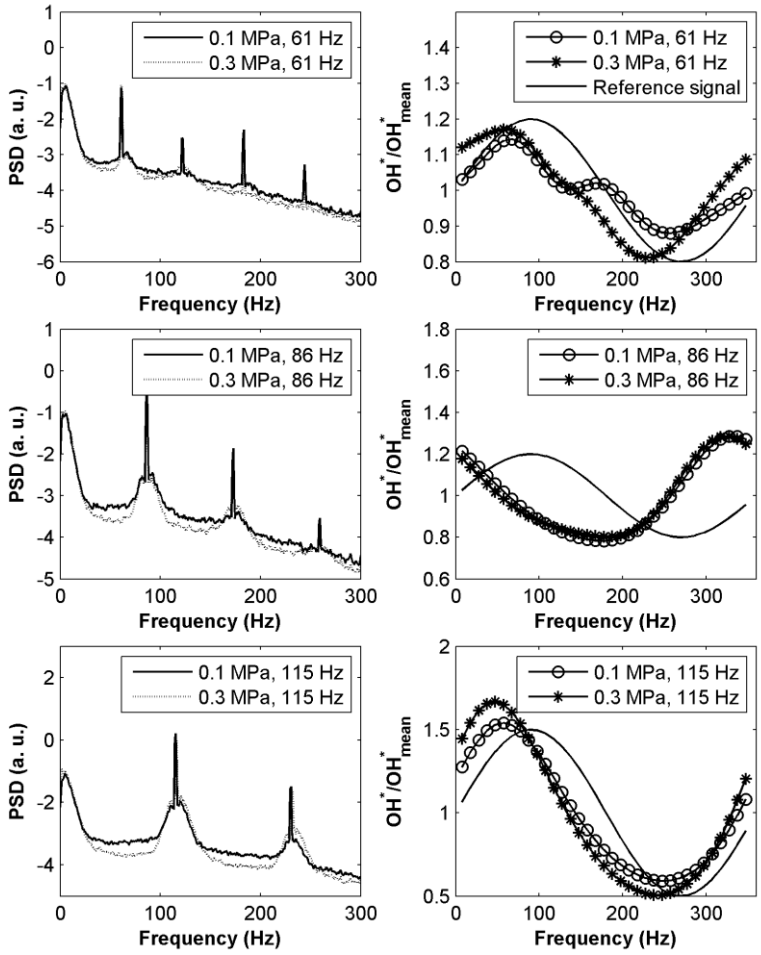

Figure 2.5. Power spectral density (PSD) of OH*. The perturbation levels (P_A/P_c) are 0.3%, 0.3%, and 0.4% in the cases with the frequencies of 61 Hz, 86 Hz, and 115 Hz, respectively.

The phase-averaged curves of OH* demonstrates that all cases are affected by harmonic oscillations, which are relatively strong in the cases with a forcing frequency of 61 Hz. It can also be noticed that the oscillation curves are similar in the cases with the same frequency even when the ambient pressure changes.

According to the work of Culick [5], the instability trend can be analyzed based the Rayleigh criterion,

$$R \propto \frac{1}{\xi}\int_V \int_0^{\xi} p'q'dtdv > 0 \tag{2.1}$$

where t is the time and ξ is the period, V is the volume, p' and q' are the pressure oscillation and the heat release fluctuation, respectively. According to the OH* power spectrum, q' can be expressed as,

$$q' \approx \sum_{i=1}^{n} q_{A,i} \cdot sin(2\pi f_i t + \phi_i) \quad (i = 1, 2, \ldots, n) \tag{2.2}$$

where $q_{A,i}$, f_i, and φ_i are the amplitude, the frequency, and the phase of the i^{th} mode, respectively. In the current test, p' showed a quasi-sinusoidal oscillation with the fundamental frequency because the pressure oscillation is only induced by loudspeakers. Therefore, p' can be approximately expressed as $P_A \cdot sin(2\pi ft + \varphi)$, where P_A is the oscillation amplitude and φ is the phase. Under this condition, only the component of q' with the fundamental frequency can contribute to the integral for calculating the Rayleigh Index. It implies that the fundamental heat release oscillation plays a critical role and needs a detailed examination. However, harmonic modes also need to be studied because they may affect the fundamental mode by sharing energy.

Figure 2.6 shows the effects of the perturbation level on the phase and the normalized amplitude (OH^*_f/OH^*_{mean}) of the fundamental mode. Using the pressure signal as the reference, the phase is defined as the phase difference between the processed OH* and pressure signals.

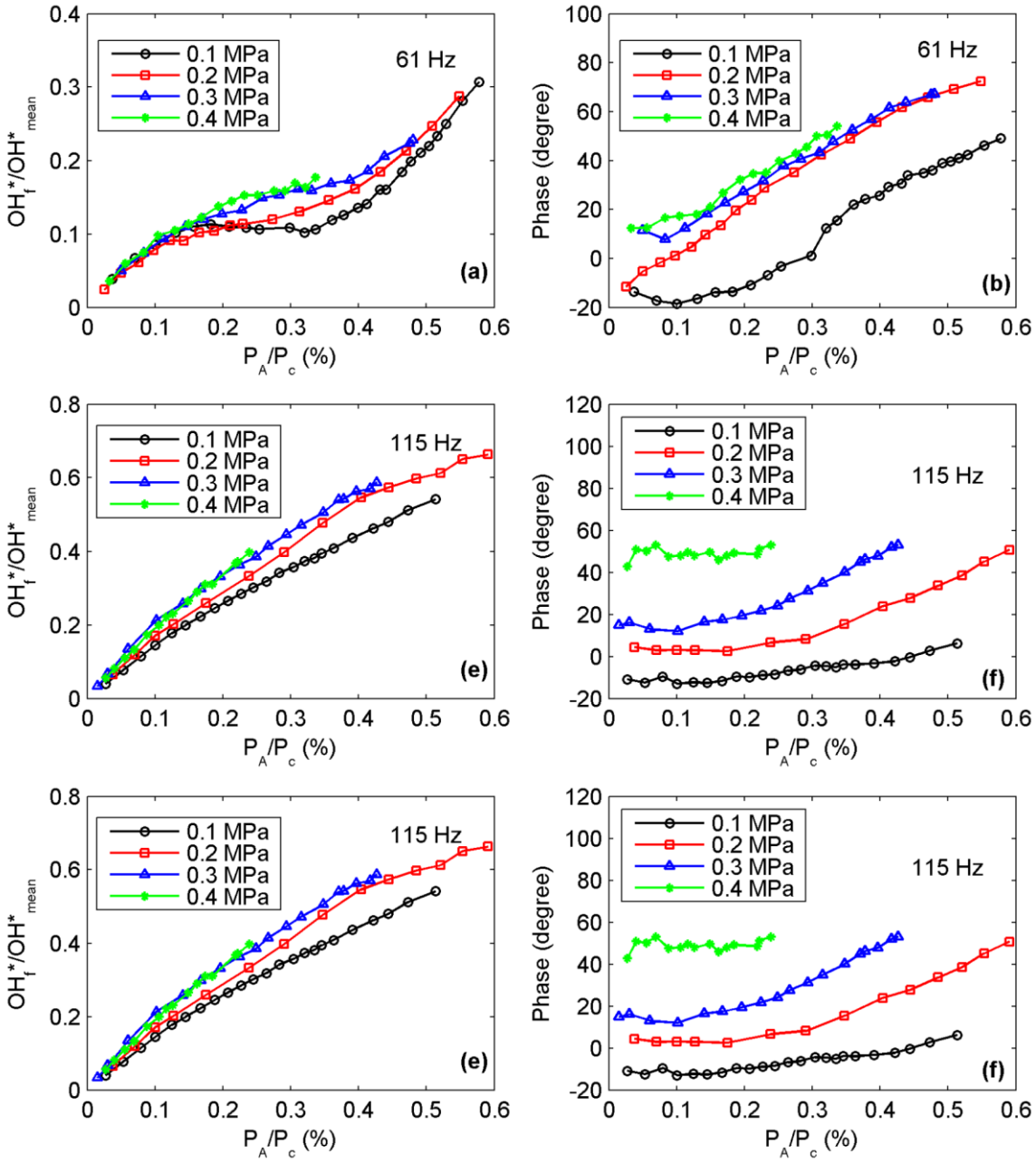

Figure 2.6. Response of the fundamental OH* oscillation under different levels of perturbation.

When f = 61 Hz, the curves of the oscillation amplitude show nonlinear trends in all cases. It can be seen in Figure 2.6(a) that the normalized amplitude increases with the pressure when P_A/P_c > 0.2%. Figure 2.6(b) illustrates that the phase increases with the increasing perturbation level and the pressure. Figure 2.6(c) and Figure 2.6(d)

demonstrate the cases with f = 86 Hz. Similar to the cases with f = 61 Hz, the curves of the normalized amplitude also experience nonlinear changes. The pressure only has a minor influence on the normalized amplitude when P_A/P_c < 0.15%, whereas the curves of the amplitude tend to diverge when the forcing amplitude is sufficiently high. The normalized amplitude initially increases when the pressure rises from 0.1 MPa to 0.2 MPa; then it decreases with the increasing pressure. Figure 2.6(d) illustrates that the dependence of the phase on pressure has a similar trend to that of the amplitude. When f = 115 Hz, the phase rises approximately monotonically with the pressure, which is similar to that shown in the cases with f = 61 Hz. The normalized amplitude shown in Figure 2.6(e) increases approximately linearly with the perturbation level, whereas only a weak nonlinear trend can be detected at 0.2 MPa when P_A/P_c > 0.4%. In general, both the phase and the normalized amplitude increase with the pressure when f = 115 Hz.

Figure 2.7 shows the dependence of the amplitude of the first harmonic mode on the perturbation level. The amplitude is normalized by the mean value of the OH* of the corresponding case. Figure 2.7(a) displays that when f = 61 Hz, the curves of the amplitude show similar trends when P_A/P_c < 0.2%, whereas the trend is more complex when the pressure increases further. It is related to the complex flame front deformation which will be discussed in a later section. In contrast, Figure 2.7(b) shows that the curves of the amplitude are approximately identical when P_A/P_c < 0.3%. Figure 2.6(c) demonstrates that when the forcing frequency is 115 Hz, the strength of the harmonic oscillation increases with the pressure when the perturbation level is sufficiently high.

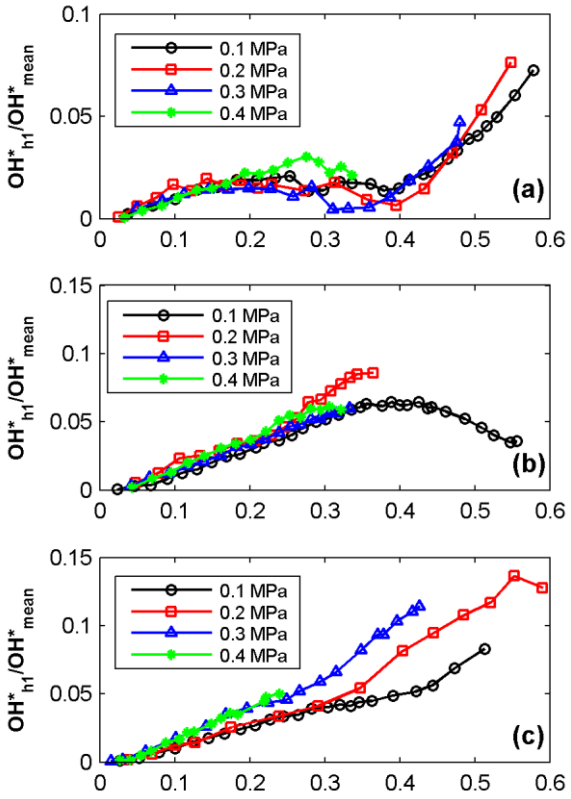

Figure 2.7. Change of the normalized amplitude (OH^*_{h1}/OH^*_{mean}) of the first harmonic oscillation with the perturbation level. (a) f = 61 Hz, (b) f = 86 Hz, and (c) f = 115 Hz.

The global analysis shows that both of the fundamental and the harmonic oscillations are affected by the pressure. For the lean premixed flames, the heat release oscillation is closely associated with the flame front deformation. Therefore, the examination of the behavior of flame is necessary, and it is analyzed through flame dynamics.

2.4.2 Flame Dynamics

Six cases, which are in or close to the nonlinear region shown in Figure 2.6, were chosen as representatives. The flow direction is from the bottom of the image to the top. Figure 2.8 shows the phase-averaged FSD images of the cases with f = 61 Hz. The general mean flame shapes show that the bottom of the flame becomes more intense

when the pressure is elevated. The general flame deformation trends are similar in both cases. However, the pressure can significantly change the flame shape at particular phase angles. For example, when P_c = 0.3 MPa, the figure at the phase angle of 15° shows intense local heat release in the center of the flame, whereas only weak heat release exists in the center region when the pressure is 0.1 MPa. Two instantaneous OH-PLIF images are shown in Figure 2.11(a) to explain the detected difference. Figure 2.11(a) shows that the flame front at 0.3 MPa can propagate further downstream in the center region. It is most likely related to the enhanced flame wrinkling [75] and the movement of convex flame front [36]. The change of the flame shape consequently leads to the global phase shift. Moreover, flame rollup can be noticed in both P_c = 0.1 MPa and P_c = 0.3 MPa cases. According to the work of Davis, et al. [23], the vortex triggered by the acoustic perturbation could be the reason causing the flame roll-up in the current study.

Figure 2.9 illustrates that the pressure also significantly changes the mean flame shape when f = 86 Hz. At phase angles of 135° to 195°, the 'wing-like' mean flame shapes at 0.1 MPa change to evenly distributed shapes at 0.3 MPa. As shown in Figure 2.11(b), it is still induced by the more wrinkled flame front under the elevated pressure condition. Furthermore, the flame roll-up, which occurs at 0.1 MPa, is weakened at 0.3 MPa.

When f = 115 Hz, Figure 2.10 shows that the flame roll-up has a relatively small scale. In the range of 195° - 315°, the flame is more condensed, and its length is reduced under the elevated pressure condition. Figure 2.11(c) shows that it is because the flame front is more wrinkled; however, the front has not moved far downstream.

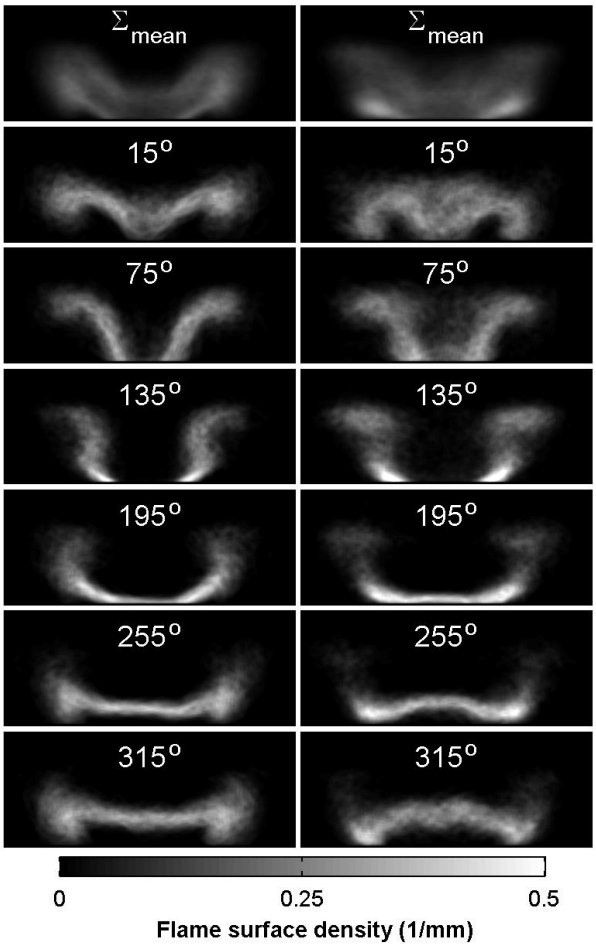

Figure 2.8. The phase-averaged FSD at the perturbation frequency of 61 Hz and the pressure of 0.1 MPa (left) and 0.3 MPa (right).

By comparing Figure 2.8 and Figure 2.9, an approximately 90-120° delay can be found between the flame rollup processes shown in the cases with f = 61 Hz and f = 86 Hz. For example, when f = 61 Hz, the flame roll-up ends at approximately 135°, whereas a similar phenomenon happens at a phase angle of 255° when f = 86 Hz. Furthermore, Figure 2.6(b) and Figure 2.6(d) illustrate that the global phases of the corresponding cases also show a phase delay with a similar scale. It has been demonstrated in Figure 2.6(d) that the heat release oscillation tends to be out-of-phase with the pressure oscillation when f = 86 Hz, whereas Figure 2.6(b) and Figure 2.6(f) show that the heat release oscillation is approximately in phase with the pressure fluctuation when f = 61 Hz and

115 Hz. By considering the effect of the pressure on the amplitude of the fundamental oscillation shown in Figure 2.6(a), (c), and (e), it can be concluded that the effect of pressure on the oscillation amplitude is more likely related to by the phase-delay. Once the pressure and the perturbation level are high enough, the pressure tends to inhibit the fundamental oscillation when the heat release oscillation is out-of-phase with the pressure oscillation; otherwise, the pressure tends to amplify the fundamental oscillation.

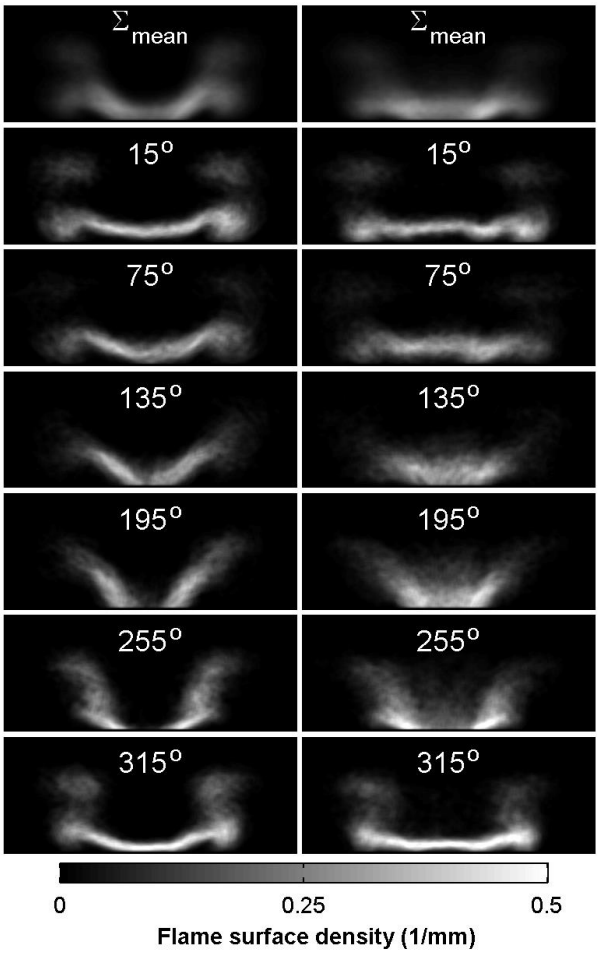

Figure 2.9. The phase-averaged FSD at the perturbation frequency of 85 Hz and the pressure of 0.1 MPa (left) and 0.3 MPa (right).

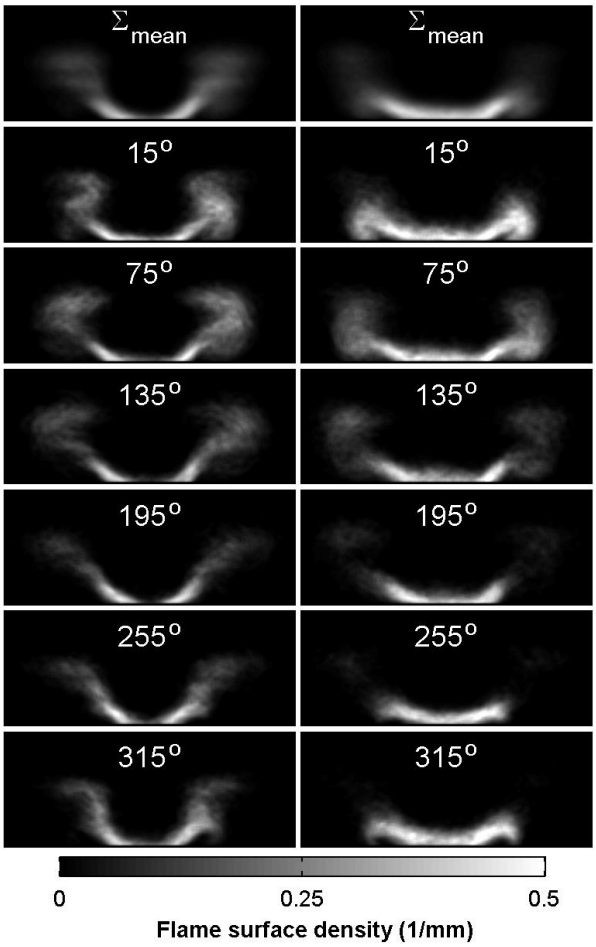

Figure 2.10. The phase-averaged FSD at the perturbation frequency of 115 Hz and the pressure of 0.1 MPa (left) and 0.3 MPa (right).

2.4.3 Local Flame Response

Although the results illustrated in Figure 2.5 show that the harmonic mode plays a minor role, there could be intense local harmonic oscillations that affect the local fundamental oscillation. Furthermore, it has been demonstrated in the work of Kim [32] and Balachandran [16] that participation of the first harmonic oscillations can affect the fundamental oscillation trend by sharing the energy. Therefore, it is necessary to examine the harmonic modes. Limited by the phase resolution of the phase-averaged FSD results, only the fundamental and the first harmonic modes were analyzed.

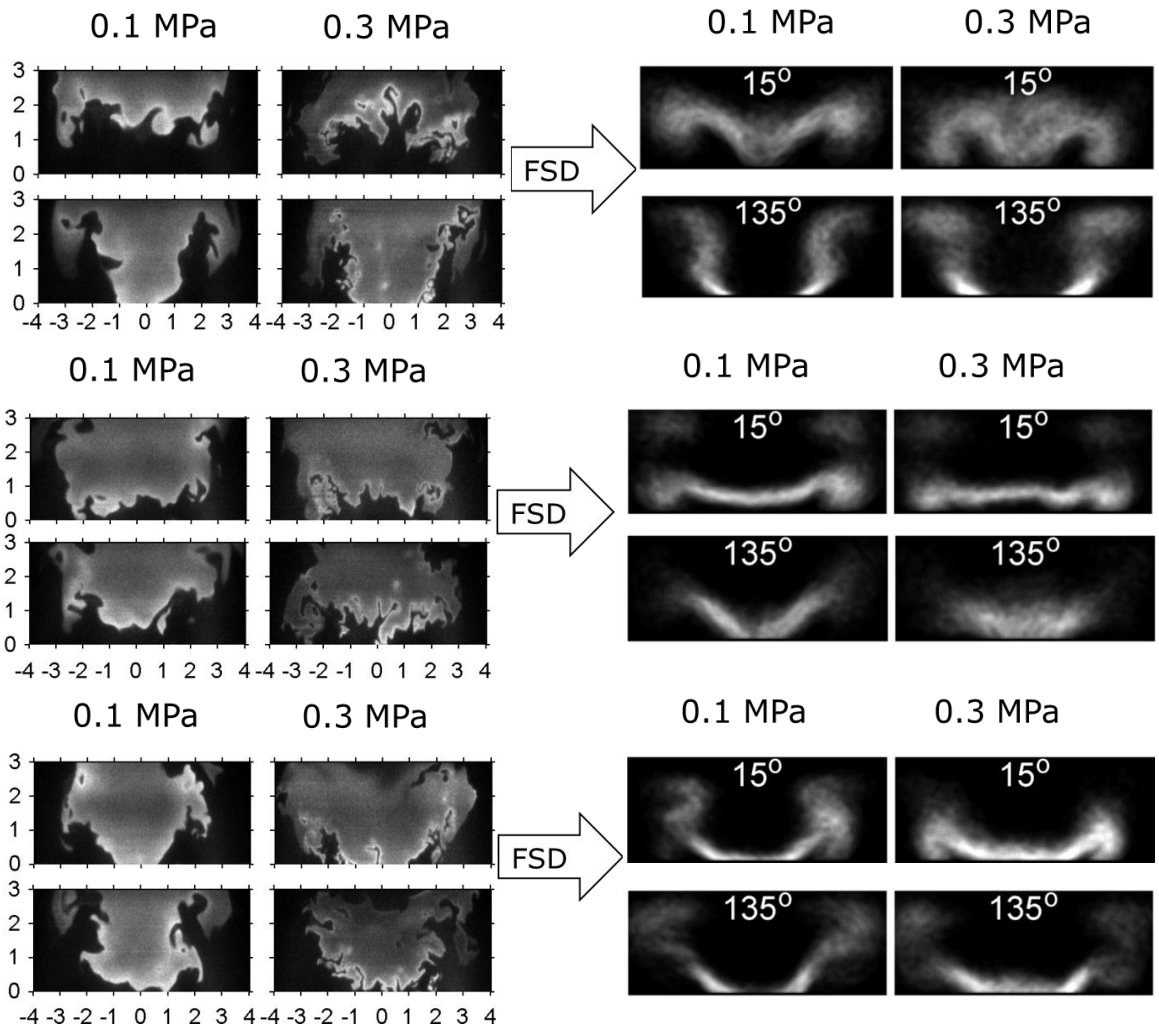

Figure 2.11. The instantaneous OH-PLIF images of the cases with different perturbation frequencies: (a) f = 61 Hz, (b) f = 86 Hz (c) f = 115 Hz at phase angles of 15° and 135°.

Figure 2.12, Figure 2.13, and Figure 2.14 demonstrate the maps of the amplitude and the phase of the local oscillations. When f = 61 Hz, Figure 2.12 shows that the amplitude maps of the fundamental oscillation have a two-layer structure that is separated by a near-zero amplitude region (node region). The upper layer is intensified when the pressure increases, which is the result of the extended reaction region shown in the phase-averaged FSD images (Figure 2.8 (a)). The local harmonic oscillations, which have comparable amplitudes with that of the fundamental mode, can also be detected in the node region. When the pressure is elevated, the strength of the local harmonic oscillation

has not been significantly changed, whereas the local phase distribution shows a notable difference.

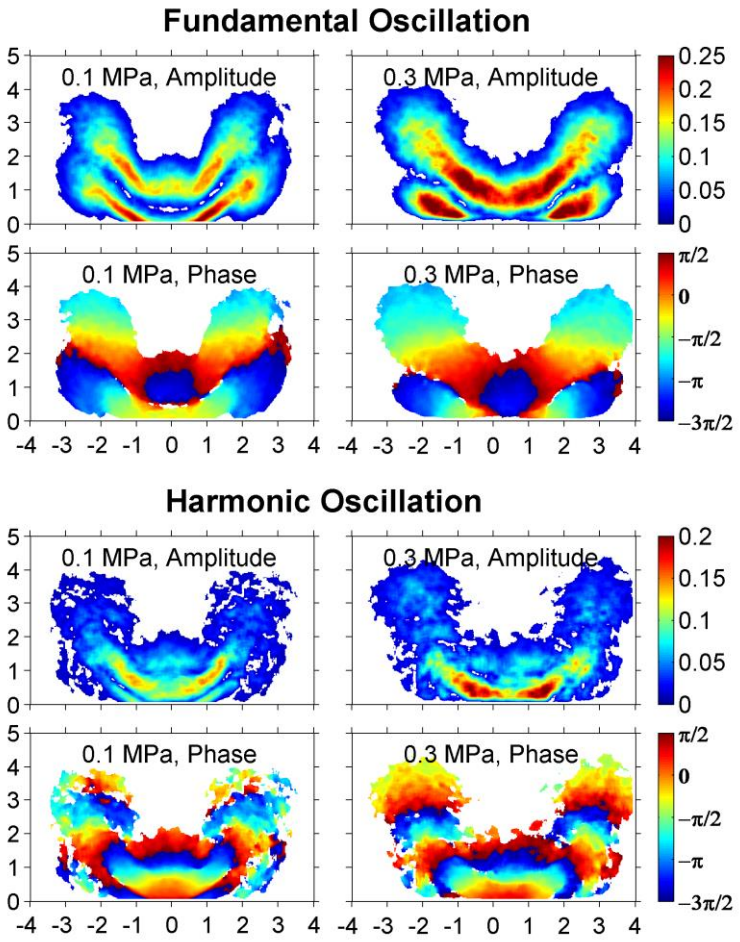

Figure 2.12. Local flame surface density oscillation of the cases with f = 115 Hz with P_A/P_c = 0.4%.

When f = 86 Hz, Figure 2.13 illustrates that the local amplitudes in different layers are comparable at 0.1 MPa, whereas the upper layer is broadened and weakened at P_c = 0.3 MPa. Furthermore, the phase distribution (especially that in the center region) can quantitatively show that the flame at f = 86 Hz oscillates out-of-phase with the flame at f = 61 Hz. It can also be noticed that the local harmonic oscillations are relatively weak and mainly exist near the bottom of the flame. With a minor effect of the local harmonic oscillation, the pressure affects the global fundamental oscillation mainly by changing the

phase and the amplitude distribution of the local fundamental oscillation. When f = 115 Hz, Figure 2.14 shows that the amplitude of the local fundamental oscillation has a similar distribution in both low and high-pressure conditions. A node region separating the upper and lower layer can be found under the low-pressure condition, whereas the node region is smaller when the pressure rises. Meanwhile, the harmonic oscillations are even weaker than the prior cases.

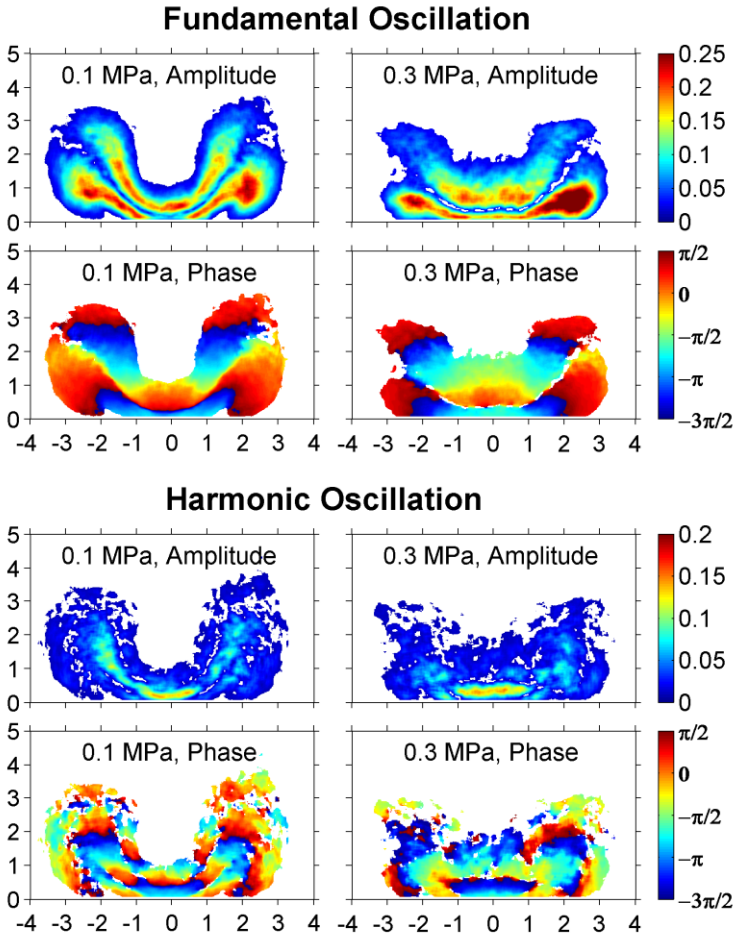

Figure 2.13. Local flame surface density oscillation of the cases with f = 86 Hz with P_A/P_c = 0.3%.

In all cases shown in local oscillation maps, a node region exists between the two layers found in the fundamental amplitude maps. This can happen in two situations. The first one is when the intense harmonic oscillations dominate the local oscillation, which

can be shown in the cases with f = 61 Hz. The other one is when the flame oscillates mildly around its neutral region, in which the heat release experiences near-zero changes. As shown in local oscillation maps, the strength of the local harmonic oscillation is closely associated with the scale of the flame rollup. The intense local harmonic oscillations, whose amplitudes are greater than 0.15 mm^{-1}, mainly exist in the node region shown in the local amplitude maps of the cases with f = 61 Hz and f = 86 Hz. When f = 115 Hz, only relatively weak harmonic oscillations can be detected.

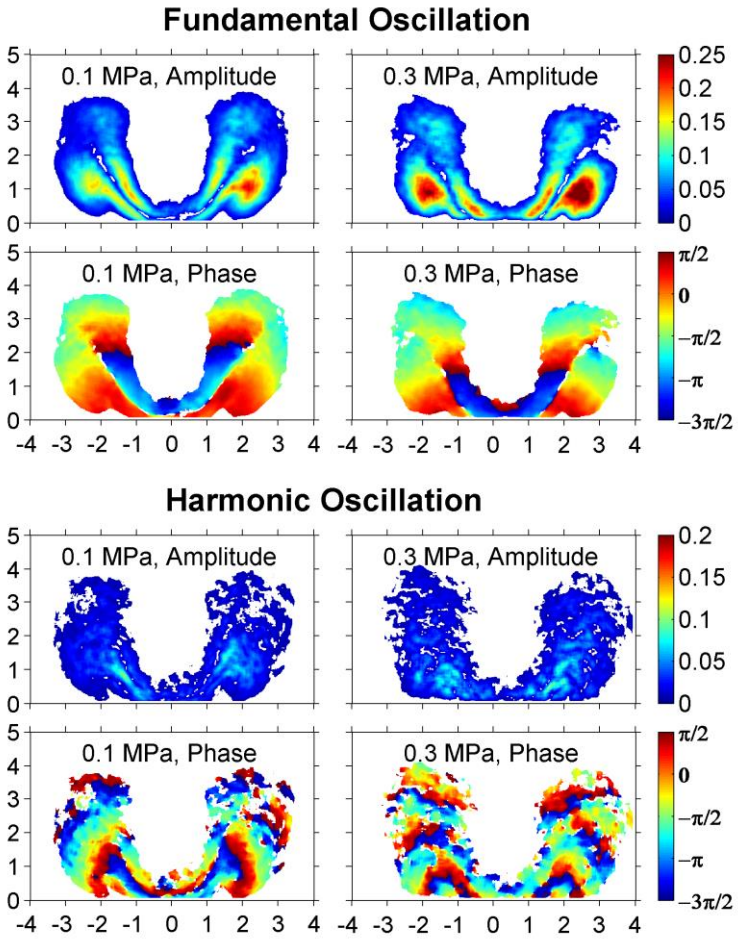

Figure 2.14. Local flame surface density oscillation of the cases with f = 61 Hz with P_A/P_c = 0.3%.

2.5 Conclusions

The current work examined the effects of pressure variation on the flame response to the acoustic perturbation with different frequencies. In the cases with perturbation frequencies of 61 Hz and 115 Hz, the heat release oscillation is found to be approximately in phase with the pressure fluctuation. In these two cases, the elevated pressure amplified the fundamental oscillation and changed the phase to a higher value. In contrast, when the pressure was sufficiently high, the elevated pressure tended to inhibit the fundamental oscillation in the cases with f = 86 Hz, at which the heat release oscillation was approximately out-of-phase with the acoustic perturbation.

Analysis of flame dynamics and local flame structures showed that the phase difference among different cases was caused by the delay in the different types of flame roll-up. The elevated pressure can increase flame front wrinkles. However, the influence of the pressure on flame propagation is strongly phase-dependent. In general, the pressure affected the strength and the distribution of the local fundamental and the local harmonic oscillations. Furthermore, the effect of the pressure on the distribution was larger than that on the strength, which could be the main way through which the pressure affected the global heat release oscillation.

CHAPTER 3
EXPERIMENTAL STUDY THE LOCAL FLAME FEATURES CREATED BY ACOUSTIC PERTURBATION

In this chapter, the effects of the acoustic perturbation level on the local flame features, such as the local heat release rate oscillation, are examined. This chapter presents the analysis methods employed in the current research for a modified local analysis with a proper orthogonal decomposition (POD) method, which aims to reduce the number of images needed for calculating low-uncertainty local oscillation information. The results are mainly demonstrated with Rayleigh Index maps and the maps of the local oscillation amplitude and phase.

3.1 Data Analyzing Method

The experimental configuration is the same as the one described in Chapter 2. All tests were under the atmospheric condition. This section will only describe the data analysis methods used in Chapter 3.

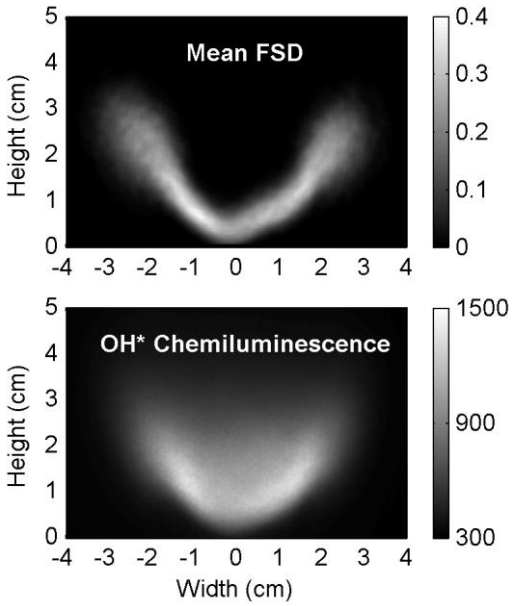

Figure 3.1. A comparison between the mean FSD (with units of mm^{-1}) and the mean OH* chemiluminescence image (with arbitrary units).

3.1.1 Flame Surface Density

The flame surface density was calculated based on the method introduced in Chapter 2. To ensure there is no significant difference between FSD images and OH* chemiluminescence images that are commonly used to show the flame shape, a comparison was made between the mean images obtained these two methods. Figure 3.1 shows a comparison example of a case with U = 5 m/s and f = 125 Hz.

3.1.2 Rayleigh Criterion Analysis

In the current study, q' is assumed to be proportional to FSD oscillation. Subsequently, a local non-dimensional Rayleigh Index ($R^*_{x,y}$) is defined as a discrete form,

$$R^*_{x,y} = \frac{1}{N \cdot \bar{\Sigma} \cdot P_{RMS}} \sum_{i=1}^{N} P'_i (\Sigma^i_{x,y})' \tag{3.1}$$

where $(\Sigma_{x,y})'$ is the local FSD oscillation of the i^{th} phase, P'_i is the pressure oscillation of the i^{th} phase, N is the number of phases, P_{RMS} is the root mean square of the pressure oscillation, and $\bar{\Sigma}$ is the averaged flame surface density. With the discrete form, the local Rayleigh Index can be calculated pixel by pixel. In the results, a positive value represents that local instability tends to be encouraged. In contrast, if local instability tends to be damped, the regions are marked with negative values. The absolute value of $R^*_{x,y}$, positive $R^*_{x,y}$, and negative $R^*_{x,y}$ are subsequently referred to as coupling intensity, positive coupling, and negative coupling, respectively.

Typical Rayleigh Index maps are illustrated in Figure 3.2 as examples, which show shaped patterns called coupling structures or coupling regions. In Figure 3.2, the zero (0) on the bottom edge represents the center of the burner, whereas the zero (0) on

the left edge denotes the outlet of the burner. It also shows that the Rayleigh Index distribution is quasi-symmetric around the centerline of the burner.

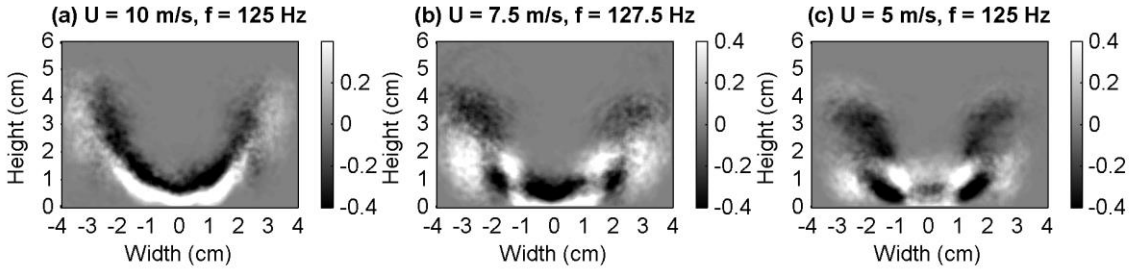

Figure 3.2. Rayleigh Index maps. (a) The case with a bulk velocity of 10 m/s and a forcing frequency of 125 Hz; (b) the case with a bulk velocity of 7.5 m/s and a forcing frequency of 127.5 Hz; (c) the case with a bulk velocity of 5 m/s and a forcing frequency of 125 Hz.

3.1.3 POD Analysis

The POD method used in the current study can be represented by an equation modified from Holmes' book [76],

$$\Sigma(\vec{x},t_k) = \sum_{i=1}^{M} \alpha_i(t_k)\varphi_i(\vec{x}) + \Sigma_{mean}(\vec{x}) \tag{3.2}$$

where $\Sigma(\vec{x},t_k)$ is the k^{th} phase-averaged FSD image that depends on time (t_k) and space ($\vec{x}$), $\Sigma_{mean}(\vec{x})$ is the mean FSD image, $\varphi_i(\vec{x})$ is the i^{th} mode related to spatial information, M is the phase-bin number, and $\alpha_i(t_k)$ is the i^{th} coefficient related to the time.

The fundamental modes $\varphi_i(\vec{x})$ can be calculated with a method called snapshot [76, 77],

$$\vec{\varphi} = \sum_{k=1}^{M} \alpha_k \vec{\Sigma}'^k \tag{3.3}$$

$$\vec{\Sigma}^k = \vec{\Sigma}^k - \vec{\Sigma}_{mean} \tag{3.4}$$

$$\sum_{k=1}^{M} \frac{1}{M} (\vec{\Sigma}'^{k}, \vec{\Sigma}'^{i}) \alpha_k = \lambda \alpha_i ; i = 1,2,3,..M \tag{3.5}$$

where $\vec{\Sigma}^k$ is the vector extracted from the k^{th} phase-averaged FSD image, $\vec{\Sigma}_{mean}$ is the vector extracted from the mean FSD image, $\vec{\Sigma}'^k$ is the difference between $\vec{\Sigma}^k$ and $\vec{\Sigma}_{mean}$, λ is the eigenvalue, and α_k is the coefficient used to calculate the modes. α_k can be obtained by finding the eigenvalues of the correlation matrix with equation (3.5). The role of the POD mode φ_i is determined by its energy percentage, which is calculated from eigenvalues,

$$\eta_i = \frac{\lambda_i}{\sum \lambda_k} \tag{3.6}$$

where η_i is the energy percentage of the i^{th} mode. The mode with larger eigenvalues contains more oscillation energy and subsequently plays a more important role in the global behavior.

3.1.4 Operating Conditions

As demonstrated in Kang's work [25], the change in the coupling structures is well represented by the wavenumber, which is proportional to the number of the coupling structures distributing along the flame edge. When perturbation frequency increases, the wavenumber shows both linear and nonlinear trends. In the current study, only the linear zone was examined because the nonlinear zone is related to more complex vortex behavior, and is not in the scope of the current work.

Prior work with the LSB has already examined the effects of the forcing frequencies on flame behavior at a constant perturbation level [25, 31]. As an extension,

the current work aims to examine the effects of the perturbation level on the low swirl flame with fixed perturbation frequencies.

Table 3.1. Operating conditions

U (m/s)	Equivalence Ratio	$\dot{m}_{Air}$ (g/s)	$\dot{m}_{Methane}$ (g/s)	f (Hz)	P'/P_{atm} (%)
10 m/s	0.85	5.44	0.27	125 ± 0.6	0.25 − 1.07
7.5 m/s	0.85	4.08	0.203	127.5 ± 0.6	0.06 − 1.04
5 m/s	0.85	2.72	0.135	125 ± 0.6	0.07 − 0.81

All test cases are listed in Table 3.1. The equivalence ratio is 0.85 for all cases. It can be noted that the range of forcing amplitudes varies in different cases. It is because that the dissipation rate of the acoustic power in the chamber changes with the perturbation frequencies.

3.2 Results

3.2.1 Pressure Spectrum

For the system using acoustic perturbation, it is important to verify that speakers are the only source that triggers the pressure oscillation. The pressure power spectral density (PSD_P) results of two cases are shown in Figure 3.3 to illustrate the leading modes at different forcing levels. It can be seen that the forcing frequency dominates the response of the chamber in both the lowest and highest perturbation conditions. Although harmonic modes can be detected at strong forcing conditions, they are approximately two

orders lower than that of the primary modes, so they are a minor factor. The acoustic forcing level is represented by the percentage of the forcing amplitude (*P'*) to the atmospheric pressure (*Patm*).

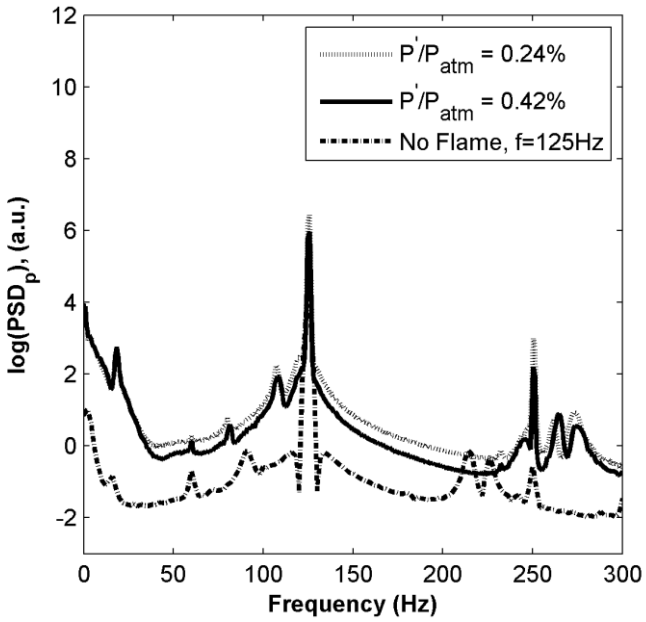

Figure 3.3. logarithm value of PSD of the cases with a bulk velocity of 5 m/s and a forcing frequency of 125 Hz.

3.2.2 Rayleigh Index Maps

Figure 3.4 shows the effects of perturbation level on the Rayleigh Index maps when the bulk velocity changes. The left border of each image is the centerline of the burner outlet, whereas the bottom border is just above the outlet of the burner. The range of the colorbar is adjusted to give a better view of the coupling structures.

As the forcing level increases, similar coupling structures appear in the 10 m/s cases. It is also apparent that when the forcing amplitude rises, the intensity and clarity of the coupling structures increase. In all cases shown in Figure 3.4, the negative coupling

regions lie just adjacent to the positive coupling regions, and this phenomenon has previously been observed in the work of Huang [28].

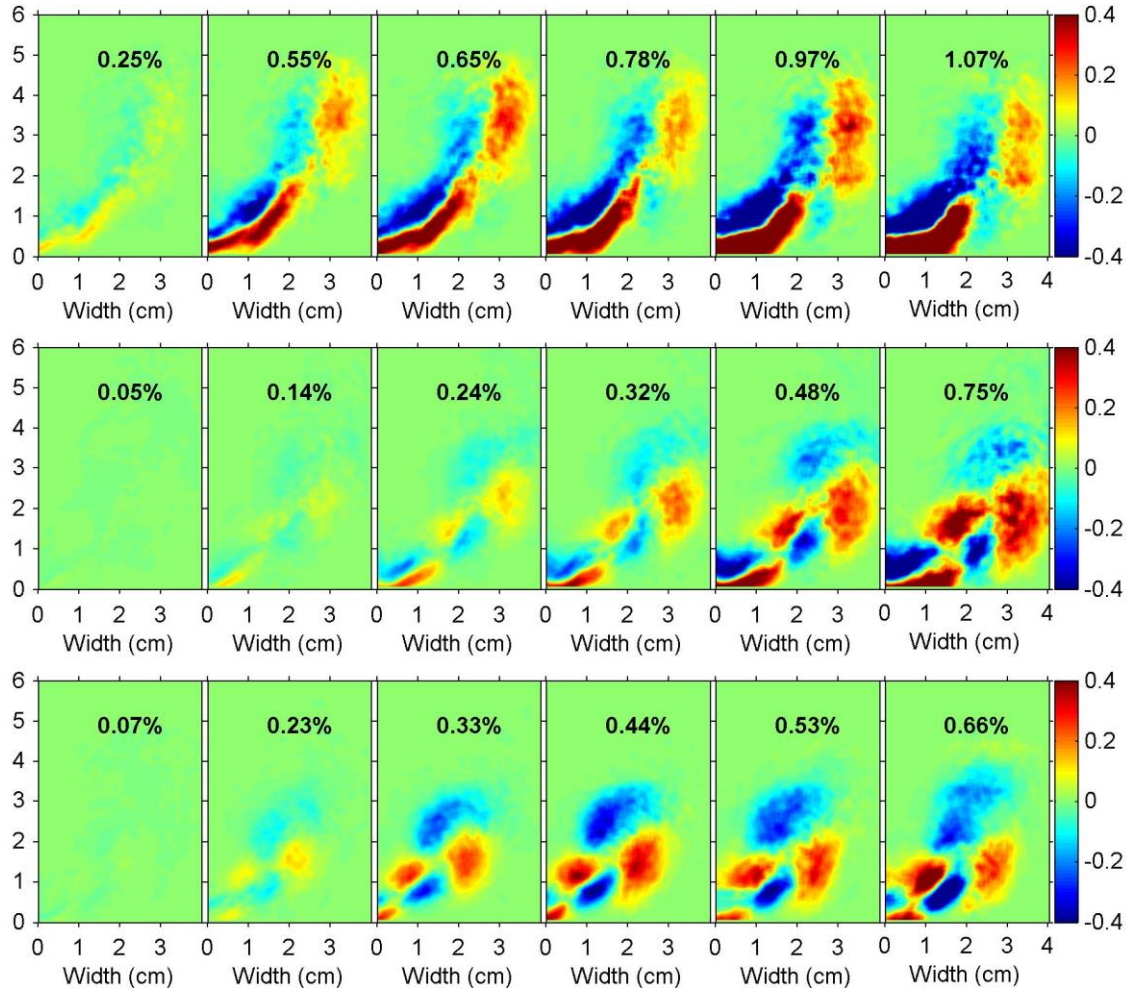

Figure 3.4. Rayleigh Index maps of the cases with U = 10 m/s (top), U = 7.5 m/s (middle), and U = 5 m/s (bottom).

Figure 3.4 also shows the Rayleigh Index maps for the cases with a bulk velocity of 7.5 m/s. In contrast to the coupling structures shown in cases with U = 10 m/s, periodically distributed coupling structures with different signs are found when U = 7.5 m/s. These coupling structures are believed to be the result of the flame front deformations induced by the local vortex, which is the result of the shear layer instability triggered by the acoustic perturbation. In cases where U = 7.5 m/s, the coupling structures

not only vary in their intensity and size but also change their locations with forcing level. For example, the largest positive coupling region expands towards the bottom of the flame when the forcing level increases. This upstream-shifting trend is believed to be caused by the upstream movement of the vortex when the acoustic perturbation is enhanced [78].

It is also shown in Figure 3.4 that the number of coupling structures increases further when the bulk velocity decreases to 5 m/s. It is believed to result from a further decrease in the vortex convection velocity. Similar to the results seen in the cases with U = 10 m/s and U = 7.5 m/s, the coupling structures increase in size and intensity when the perturbation level rises. Nevertheless, different from the cases with U = 7.5 m/s, the distribution of the coupling structures is relatively stable at U = 5 m/s.

The Rayleigh Index maps confirm that the local instability trend shows a significant variation. They provide general information about the local coupling between local heat release rate and pressure oscillation. However, the local heat release rate oscillation, which is important in understanding the local instability trend, is still not fully demonstrated. The next section will discuss several methods used for calculating the local heat release rate oscillation.

3.3 Local Analysis of Heat Release Rate

3.3.1 Curve Fitting Method with Raw Phase-averaged FSD

As a first attempt, a curve fitting method that uses two sinusoidal functions $A_1 \cdot Sin(\xi_1 \cdot t + \varphi 1) + A_2 \cdot Sin(\xi_2 \cdot t + \varphi_2)$ (where A_1 and A_2 represent the amplitude, ξ_1 and ξ_2 represent the period, and φ_1 and φ_2 denote phase) was applied to the phase-averaged FSD data. However, this method will introduce a high uncertainty because of the appearance

of harmonic oscillations. A case with U = 5 m/s and P'/P_{atm} = 0.44% is used as an example.

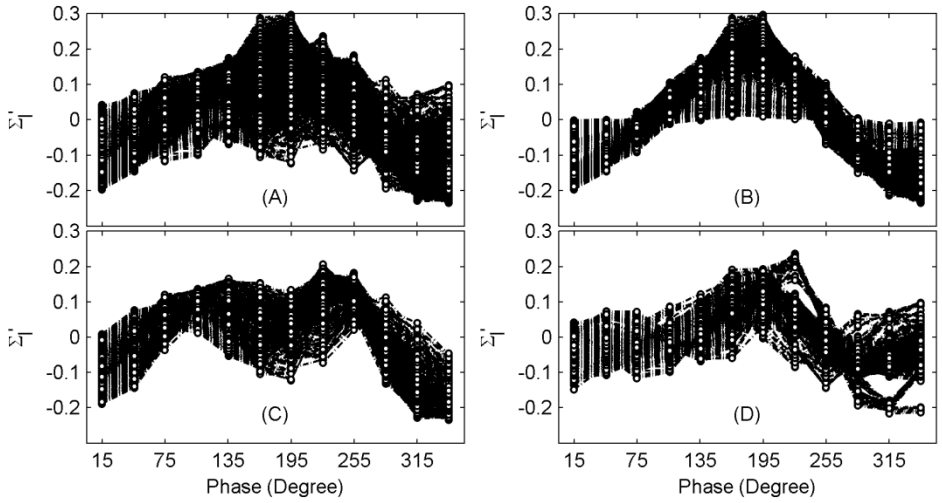

Figure 3.5. Plots of the local FSD oscillations with a phase of -90 ± 3° with respect to the pressure signal: (A) all oscillations (1516 locations), (B) fundamental frequency dominated oscillations (715 locations), (C) the oscillations with non-fundamental frequency, type 1 (323 locations), (D) the oscillations with non-fundamental frequency, type 2 (477 locations) (Σ_l' represents the local FSD oscillation).

Figure 3.5A shows the plots all of the local oscillations (1516 locations) with a phase angle of -90 ± 3° and a dominant frequency of 125 Hz. As seen in Figure 3.5B, only 715 (47.2%) locations show approximately single-frequency oscillations. Figure 3.5C and Figure 3.5D show non-fundamental frequency oscillations, where the energy provided by the acoustic perturbation is split between frequencies. This implies that the non-fundamental frequency oscillations could play an important role in the local flame response. Therefore, it is necessary to examine the behavior of the fundamental and non-fundamental frequencies separately. Although the regular curve fitting can capture the general trend observed at an individual location, the global contribution of each oscillation is difficult to compute. Furthermore, the noise in the raw data makes it difficult to obtain accurate curve fitting results. For example, the uncertainty in the

computed value of the non-fundamental frequency is higher than 30% at approximately 40% of locations.

To address these problems, the first option is to replace the pressure-based phase-averaged method with a new phase-averaged method to capture single-frequency oscillations, whereas the other is to decompose the current pressure-based phase-averaged results into single-frequency oscillations. In the current research, the POD method is used to capture the single-frequency oscillations and estimate their role in the global trend.

3.3.2 Determination of the Phase Angle of the Image with the POD Method

The POD method was first applied to the time series of FSD images to obtain the POD-based phase without considering the pressure signal. 300 images were used in a single case. With the method described in the work of M. Stöhr [79] and K. Oberleithner [80], the phase of each image was detected from the scatter plots of the normalized mode coefficients shown in Figure 3.6.

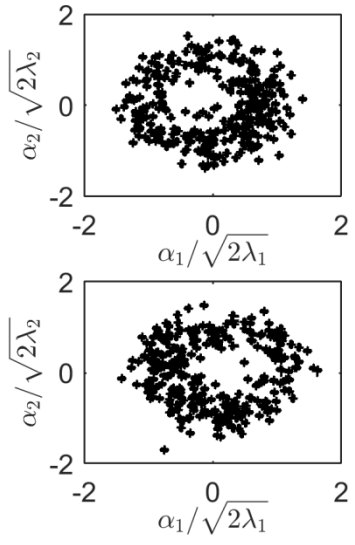

Figure 3.6. Scatter-plot of the normalized mode coefficients a1 vs. a2, (Left) P'/P_{atm} = 0.37%, (Right) P'/P_{atm} = 0.66%.

Once the phase was defined, the FSD images were distributed to a 30-degree-wide phase bin. The POD-based phase-averaged results were then compared with the pressure-based results and the comparison is shown in Figure 3.7. It shows that the phase obtained from POD does not always match with that of the pressure-based method. This implies that the phase defined with POD is not closely coupled to the pressure information, which is critical in the current analysis. Nevertheless, the desire to confidently identify the structures present at the dominant frequencies motivates the need for a modified analysis technique that can identify the structures at the frequencies of interest.

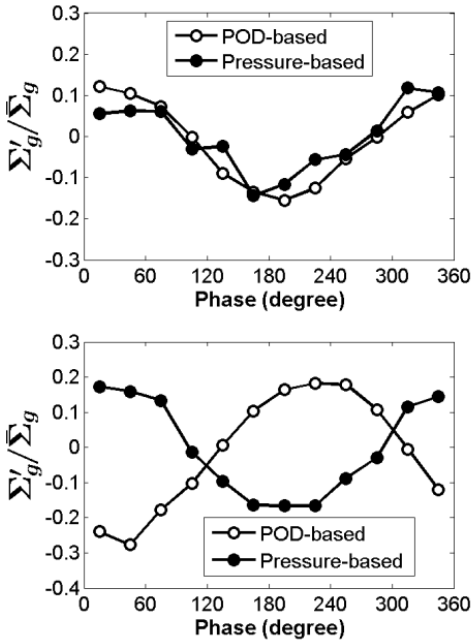

Figure 3.7. Phase-averaged FSD oscillation based on -defined phase and pressure-defined phase, (Top) P'/P_{atm} = 0.37%, (Bottom) P'/P_{atm} = 0.66%.

3.4 Application of POD method on Phase-averaged FSD Results

As an alternative, a phase-averaged (POD) method was proposed to provide a means of extracting the relevant structures that occur at a selected frequency with a phase angle defined by the pressure signal. It is known that the phase-averaged process filters other types of oscillation and highlights the oscillation with the 'chosen' frequency. This

may cause problems when all oscillation features are needed. However, the current flame oscillation is mainly induced by the acoustic perturbation, so the phase-averaging process will not lose the main oscillatory information. Consequently, the POD method is configured so that the key features, which are contained in the dominant modes underlying the original POD method, are unchanged, whereas the mode coefficients (eigenvalues) are re-normalized. As the POD method is applied to the phase-averaged results, the natural image-to-image noise level can also be reduced by filtering out the low-energy modes.

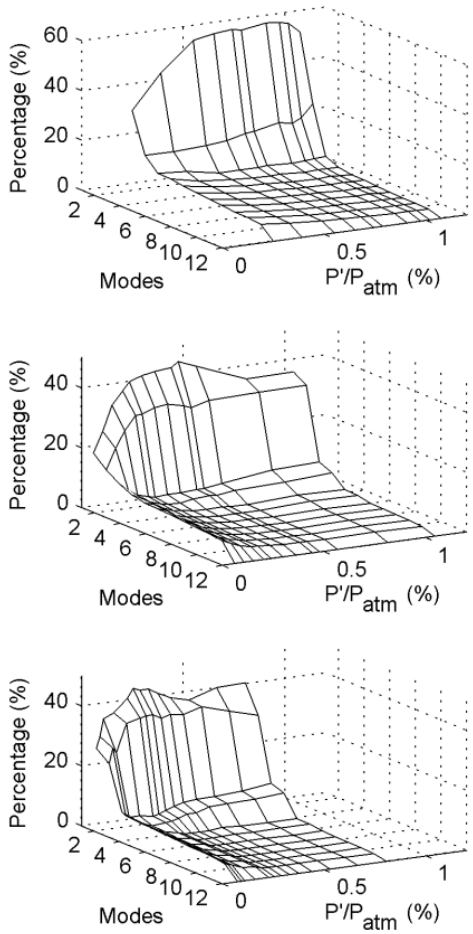

Figure 3.8. The POD energy spectra obtained from the phase-averaged FSD data of the cases with (top) U = 10 m/s, f = 125 Hz; (middle) U = 7.5 m/s, f = 127.5 Hz; (bottom) U = 5 m/s, f = 125 Hz.

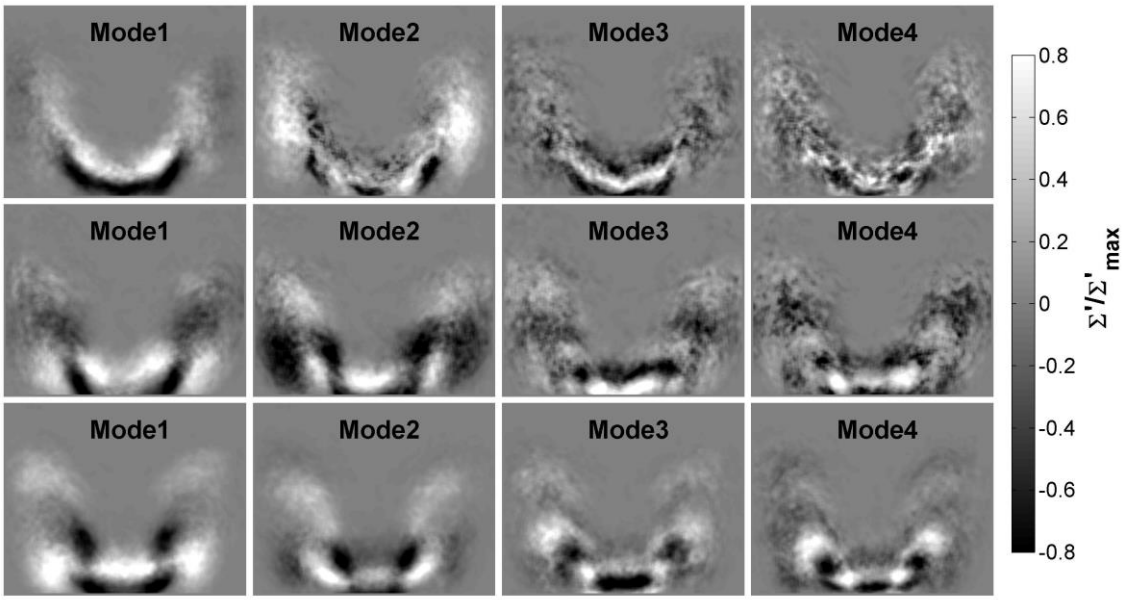

Figure 3.9. The first four POD modes of the cases with (top) U = 10 m/s, f = 125 Hz, and P'/P_{atm} = 0.55%; (middle) U = 7.5 m/s, f = 127.5 Hz, and P'/P_{atm} = 0.56%; (bottom) U = 5 m/s, f = 125 Hz, and P'/P_{atm} = 0.53%.

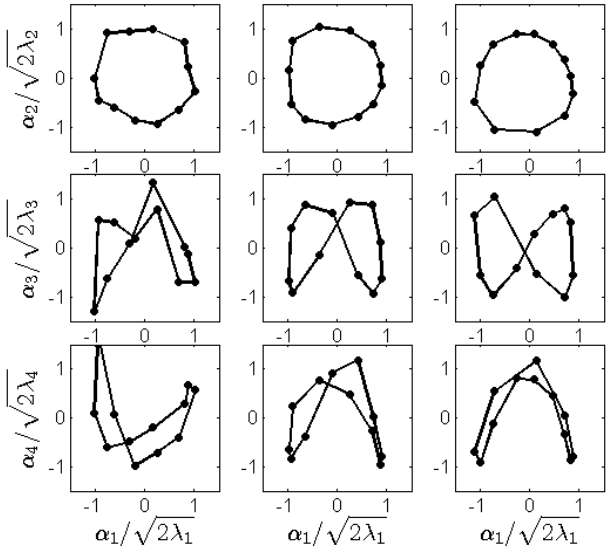

Figure 3.10. Scatter-plots of the normalized mode coefficients, (First column) U = 10 m/s, f = 125 Hz, and P'/P_{atm} = 0.55%; (Second column) U = 7.5 m/s, f = 127.5 Hz, and P'/P_{atm} = 0.56%; (Third column) U = 5 m/s, f = 125 Hz, and P'/P_{atm} = 0.53%.

Figure 3.8 shows the energy spectra for cases with different velocities. It can be seen that the first two modes take most (approximately 70%) of the energy. Figure 3.9

illustrates the first four POD modes. The negative sign indicates that the value is less than the local mean value, whereas a positive sign represents that the value is higher than the local mean value. Regular structures can be detected in modes 1 and 2 in all three cases. On the other hand, modes 3 and 4 illustrate only regular structures in the cases when U = 7.5 m/s and U = 5 m/s.

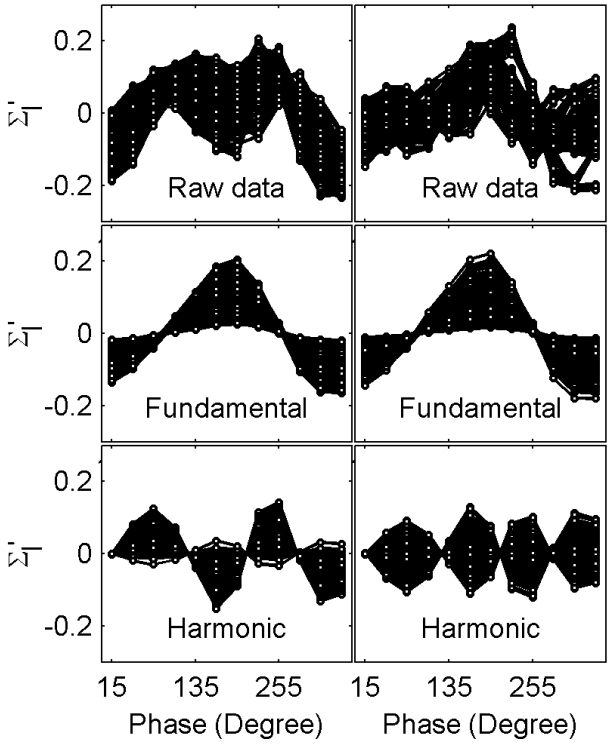

Figure 3.11. Location oscillations (shown as C and D in Figure 3.5) and their fundamental and harmonic components obtained with the POD method: type 1 (left) and type 2 (right).

Figure 3.10 shows the normalized mode coefficients. By comparison with Lissajous curves [81], it can be concluded that modes 1 and 2 represent the oscillation with the fundamental frequency (the perturbation frequency). In contrast, modes 3 and 4 when U = 5 m/s and 7.5 m/s denote the oscillations with the first harmonic frequency, whereas the case in which U = 10 m/s contains a relatively weak harmonic oscillation.

Therefore, modes 1 and 2 are referred to as the fundamental modes. Modes 3 and 4 are called harmonic modes, even though the harmonic oscillation could be easily overwhelmed by noise under low-level perturbation conditions. With the POD method, the local oscillation can be easily decomposed into fundamental and harmonic components. Figure 3.11 shows the decomposed results of the same cases shown in Figure 3.5C and D. It can be seen that the POD results can be used to confidently identify the fundamental and the harmonic components.

3.4.1 Energy of POD Modes

As discussed in the work of K.T. Kim [32], the participation of harmonic oscillation could be a reason that is responsible for the nonlinear flame behavior. Therefore, the energy proportions of the fundamental and harmonic modes are used to qualitatively illustrate their role in global oscillation. It is known that the phase-averaged process highlights the 'chosen' frequency. Therefore, the trend, rather than the absolute value, of the energy percentage is the useful information. Figure 3.12 shows the curves of the energy percentage of the fundamental modes. All curves initially increase with the rising perturbation amplitude. When the perturbation level increases further, the energy of the fundamental mode tends to saturate when U = 10 m/s, whereas the fundamental mode is weakened at U = 5 m/s and U = 7.5 m/s.

In contrast, Figure 3.13 shows the energy percentages of the harmonic modes under different levels of perturbation. The change in the energy percentage of the harmonic modes is illustrated to be dependent on the bulk velocity. When the perturbation level is not sufficiently high, all three curves decrease with increasing perturbation level because the noise in the harmonic modes is inhibited. However, when

the perturbation level increases further, the percentage curve remains stable with fluctuations when U = 10 m/s; in contrast, the percentage curves of the other two cases show an increasing trend, which indicates an increasing role in the global oscillation. This can be an indicator that the harmonic frequency oscillations can absorb part of the oscillation energy and result in the nonlinear behavior of the fundamental frequency oscillation.

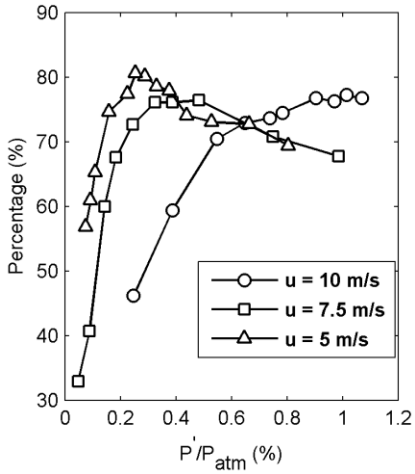

Figure 3.12. The energy percentage curves of the fundamental POD modes.

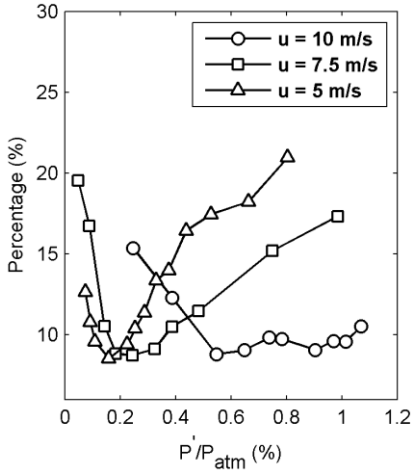

Figure 3.13. Energy percentages of the harmonic modes under different levels of perturbation.

3.4.2 Uncertainty Analysis

Energy analysis shows that the first four modes take most (approximately 90%) of the energy. Therefore, these four modes were chosen as the dominant modes, whereas other modes were considered as the 'noise' that plays a minor role. A single sinusoidal function $A_1 \cdot Sin(\omega_1 \cdot t + \theta_1)$ was then applied to each reconstructed result to calculate the period, the amplitude, and the phase of the local oscillation.

An example was shown with cases at U = 5 m/s (P'/P_{atm} = 0.66%). The number of images was increased by a step of 300 until it reaches 4500. The effect of the number of images on uncertainty is shown in Figure 3.14, which indicates that the uncertainty for fundamental oscillation is acceptable. However, the uncertainty of identifying the harmonic oscillation is high. In contrast, once the POD method is applied to filtered out the low-energy modes that contain noise, Figure 3.14 shows that the uncertainty drops significantly.

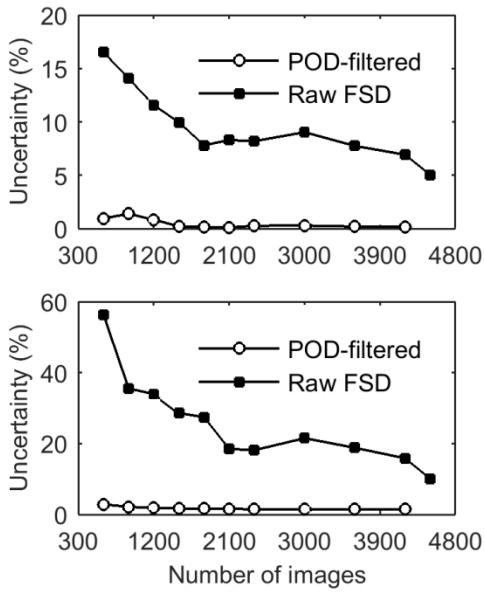

Figure 3.14. The effect of the number of images on uncertainties of the curve fitting of the fundamental oscillation (top) and the first harmonic oscillation (bottom).

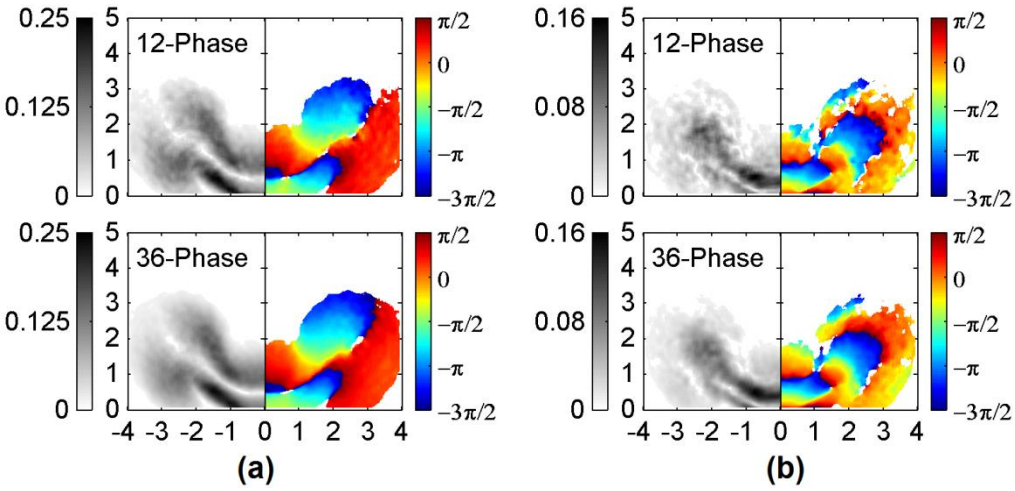

Figure 3.15. Comparison of the amplitude (left in the image) and phase (right in the image) maps between 12-phase results and 36-phase results: (a) the local fundamental oscillation; (b) the local first harmonic oscillation.

The accuracy of the current method is also verified by comparing with the 36-phase bin result. Figure 3.15 shows a comparison between a 12-phase (1200 images) result and a 36-phase (4500 images) result. Good similarities are found in the maps of both fundamental and harmonic oscillations. It shows that 12-phase results with 1200 images are sufficient to capture the key characteristics of the local oscillation.

3.5 Local Analysis Based on POD Analysis

For the fundamental oscillation, a threshold of the coefficient of determination (R-squared) is set as 0.9 to filter out the relatively poor fitting results. In the phase maps, values between $-3\pi/2$ and $-\pi/2$ can result in negative coupling, whereas phases between $-\pi/2$ and $\pi/2$ will induce positive coupling. The forcing level (P'/P_{atm}) of each case is located in the upper-left corner of each image.

Figure 3.16 shows the local amplitude and phase maps when U = 10 m/s. When perturbation level is less than 0.78%, the amplitude maps demonstrate two oscillation layers separated by a node region that is similar to the flame shape. Meanwhile, a

boundary can be detected between the positive and negative coupling phases around the same location where the node exists. Phase distributions with similar shapes can be detected under different levels of forcing. When the perturbation level is sufficiently high, the out-layer of the flame is no longer continuous, and a similar phenomenon can be detected in the phase maps. Moreover, it can be noticed that the negative coupling phase region is weaker than the positive coupling phase region.

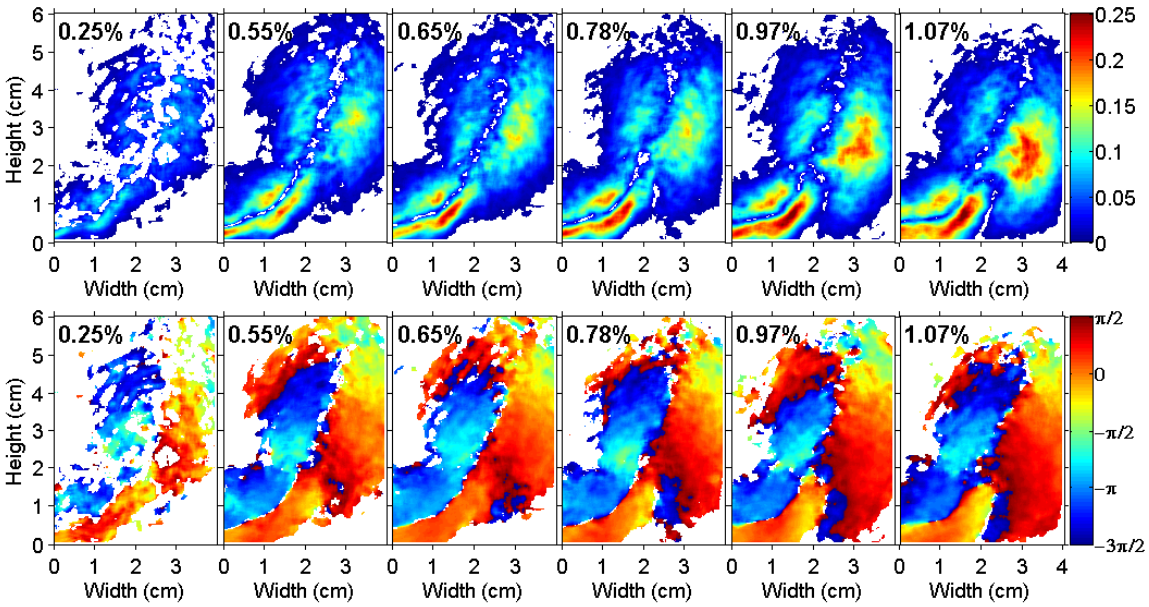

Figure 3.16. Local heat release oscillation amplitude (top) and phase (bottom) maps for the cases with U = 10 m/s, and f = 125 Hz.

Figure 3.17 illustrates the local results when U = 7.5 m/s. At the initial stage of perturbation (P'/P_{atm} = 0.15% and 0.24%), the amplitude maps demonstrate a similar shape to the cases when U = 10 m/s. Nevertheless, an additional oscillation region forms near the flame bottom under high-level perturbation conditions (P'/P_{atm} = 0.81% and 1.04%). In contrast, phase maps illustrate periodically distributed regions. Another important feature found when U = 7.5 m/s is the weakening downstream oscillation under high-level perturbation conditions (P'/P_{atm} = 0.81% and 1.04%).

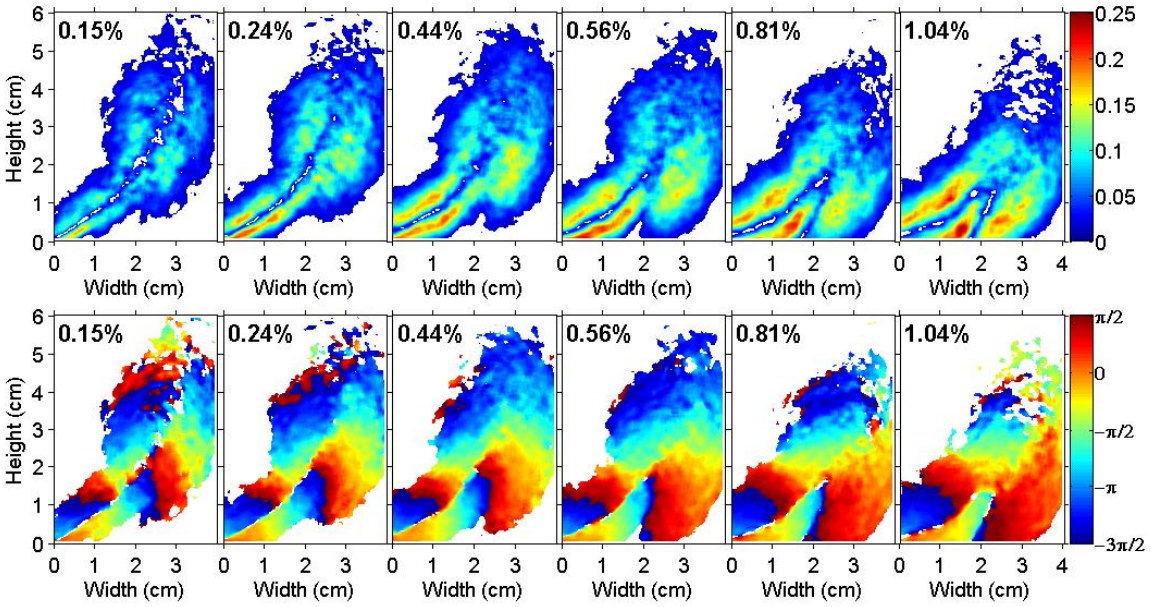

Figure 3.17. Local heat release oscillation amplitude (top) and phase (bottom) maps for the cases with U = 7.5 m/s, and f = 127.5 Hz.

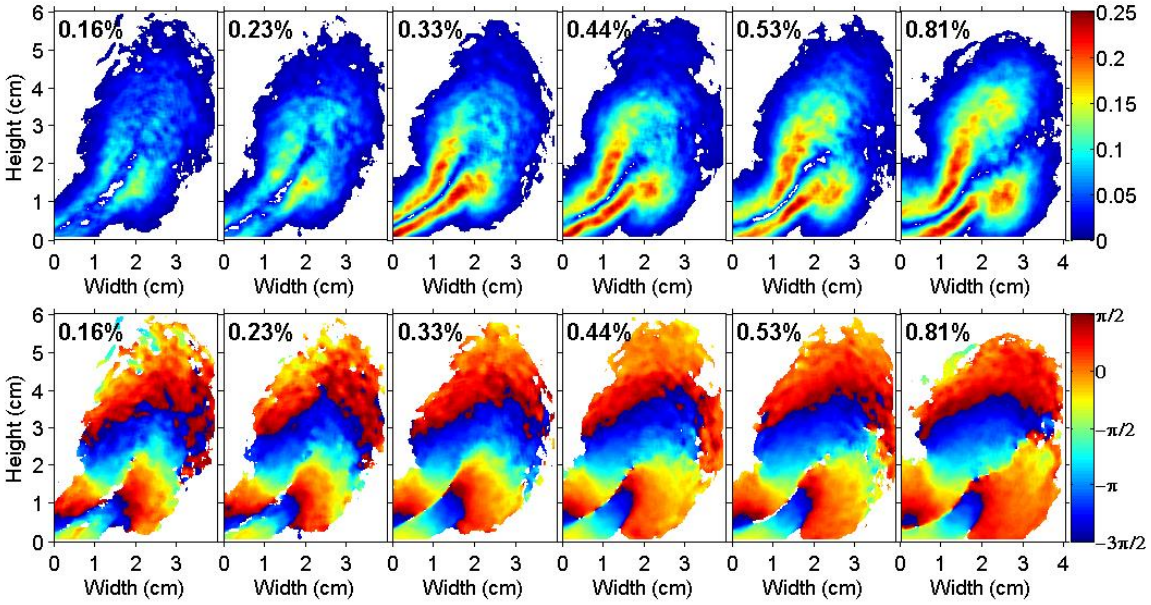

Figure 3.18. Local heat release oscillation amplitude (top) and phase (bottom) maps for the cases with U = 5 m/s, and f = 125 Hz.

Figure 3.18 shows the local results when U = 5 m/s. The maps show a bent node region that separates two oscillation layers shown in the amplitude maps when P'/P_{atm} >

0.44%. Different from previous cases that experience significant shape change, phase maps in the current case illustrate a similar shape in all cases. Nevertheless, in each phase map, the types of phase distribution upstream and the downstream of the flame are different. In the upstream region with a vertical position less than approximately 3 cm, the phase periodically varies in each oscillation layer, whereas the downstream phase mainly changes vertically.

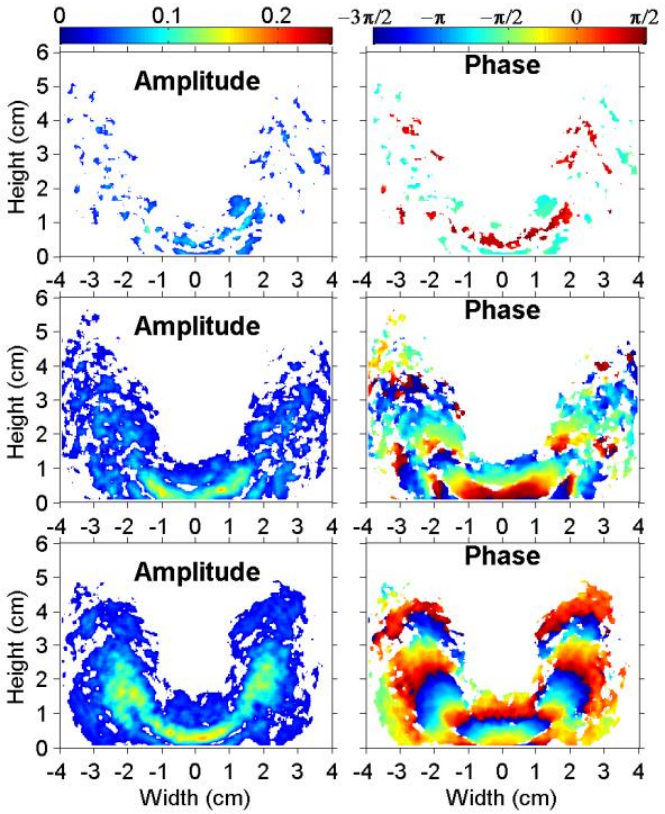

Figure 3.19. Maps of the local oscillations (with an R-square threshold of 0.85) with the harmonic frequency at (top) U = 10 m/s, f = 125 Hz, and P'/P_{atm} = 1.07%; (middle) U = 7.5 m/s, f = 127.5 Hz, and P'/P_{atm} = 1.04%; (bottom) U = 5 m/s, f = 125 Hz, and P'/P_{atm} = 0.81%.

Beyond the amplitude and phase maps of the fundamental-frequency oscillation, three local harmonic oscillation maps, shown in Figure 3.19, were chosen to illustrate the key features. It can be noticed that the strong harmonic oscillations mainly exist in the

cases with a relatively low bulk velocity. Furthermore, the harmonic oscillations mostly exist near the node region found in the amplitude maps of the fundamental oscillations. When U = 7.5 m/s because the flame oscillation is weakened in the downstream portion of the flame, the harmonic oscillations are also significantly weakened.

3.6 Conclusions

The current study uses the Rayleigh criterion and a POD method to examine the thermoacoustic features, which are related to the acoustic perturbation level, of the low swirl flame.

Rayleigh criterion analysis illustrates that the perturbation level plays an important role in determining the intensity and shape of the coupling structures. In all cases, the local Rayleigh Index distribution shows a significant spatial variation. To quantify the effects of local heat release on the local flame-acoustic coupling, a POD method was proposed to decompose the phase-averaged FSD into fundamental and harmonic oscillation. The POD-based local analysis has been proven to be efficient in inhibiting the data noise and capturing the dominant oscillation mode. Results show that the fundamental oscillation dominates the flame response, whereas the harmonic oscillation affects the flame response by sharing oscillation energy.

The POD method is not limited to the LSB but is applicable in other cases when the sinusoidal pressure oscillation information can be identified. Consequently, the current method can be useful in capturing accurate spatial information for thermoacoustic instability in flames. More generally, theoretical and numerical work can also benefit from better understanding of the spatial behavior of flame fluctuations.

CHAPTER 4
EFFECTS OF THE STROUHAL NUMBER ON THE LOCAL AND GLOBAL FLAME RESPONSES TO ACOUSTIC PERTURBATION

One of the challenges faced by the study of thermoacoustic instability is that the real system is operating under high-velocity (~ 70 m/s), which is hard to achieve for the laboratory study. The Strouhal number (*St*) is expected to be the key non-dimensional parameter that can match low-velocity and high-velocity results. The Strouhal number is defined as $St = fD/U$, where f is the oscillation frequency, D is the characteristic dimension, and U is the bulk velocity. In fact, the Strouhal number is widely used in combustion instability modeling to characterize the flame oscillation. However, there is still very limited experimental study on verifying the reliability of using Strouhal number. Moreover, the role of Strouhal number is closely related to the flame shape deformation, which implies that a local analysis is necessary to fully examine whether the Strouhal number can characterize the flame oscillation or not. In the current study, the local flame features (such as the local heat release rate oscillation) are examined together with the global flame behaviors (for example, the global heat release rate oscillation) to understand the flame oscillation behavior of cases with different Strouhal numbers. This study used the same experimental configuration as the one described in Chapter 2.

4.1 Data Analyzing Methods

Both pressure and OH* chemiluminescence data were processed with a Fast Fourier Transfer (FFT) method to detect the dominant oscillation frequency. OH* chemiluminescence captured with a PMT was employed to indicate the global heat release rate. The phase-averaged FSD was employed to obtain the local heat release rate distribution, which is used for flame structure demonstration. The current work used 12

phase bins with approximately 100 images in each phase bin. Moreover, the POD method described in Chapter 3 was still used in the current study to reduce the image number used to calculate the amplitude and phase of local heat release oscillation.

4.2 Operating Conditions

In the current study, the Strouhal number used in the current research was defined as,

$$St = \frac{fD}{U} \tag{4.1}$$

where f is the perturbation frequency of the speaker, U is the bulk velocity in the burner, and the inner diameter of the LSB (D) is chosen as the characteristic length.

Table 4.1. Operating conditions

Forcing Frequency	U (m/s)	Strouhal Number	P'/P_{atm} (%)
90 Hz	2.5	0.91	0.06 − 0.71
	3.6	0.64	0.06 − 0.72
	4.6	0.5	0.06 − 0.63
	5.4	0.43	0.05 − 0.65
	7.2	0.32	0.04 − 0.56
125.6 Hz	3.5	0.91	0.06 − 0.7
	5	0.64	0.1 − 0.8
	6.4	0.5	0.06 − 0.86
	7.5	0.43	0.12 − 0.84
	10	0.32	0.12 − 0.86

Table 4.1 shows all test conditions. In the tests, the Strouhal number is changed by varying the bulk velocity while keeping the perturbation frequency is the same. The overall experimental uncertainty is estimated to be less than 3%. Due to the dissipation rate of the acoustic power changes with the perturbation frequencies, the range of the forcing amplitude varies in different cases. When the input power is the same, the cases with the forcing frequency closer to the natural frequency of the chamber, which is around 125 Hz, have a relatively wider range.

4.3 Results

4.3.1 Global Flame Response

Figure 3.3 illustrates the Power Spectral Density (PSD) results of pressure and OH* signals. When there is no acoustic perturbation, there are no strong narrow-band oscillations can be detected in the heat release oscillation, except the low-frequency (< 20 Hz) oscillations caused by the breathing mode of the burner. It implies that there is no detectable flame oscillation resulting from the chamber modes. Once the perturbation is applied, both the pressure and the flame signals show a narrow-band mode at the perturbation frequency, which is referred to as the fundamental frequency in later sections. Moreover, harmonic modes can also be detected in pressure and flame oscillations. However, the amplitude of the harmonic pressure oscillation in all cases is less than 9 Pa, which is calculated from FFT results. It is too weak to induce the harmonic oscillations found in the current test, because the pressure oscillation needs to be higher than 40 Pa to induce a detectable flame oscillation. Figure 3.3(a2) shows that the relative strength of the first harmonic oscillation to the fundamental oscillation is relatively

weaker than that in the case shown in Figure 3.3(b2), which will be discussed in later sections.

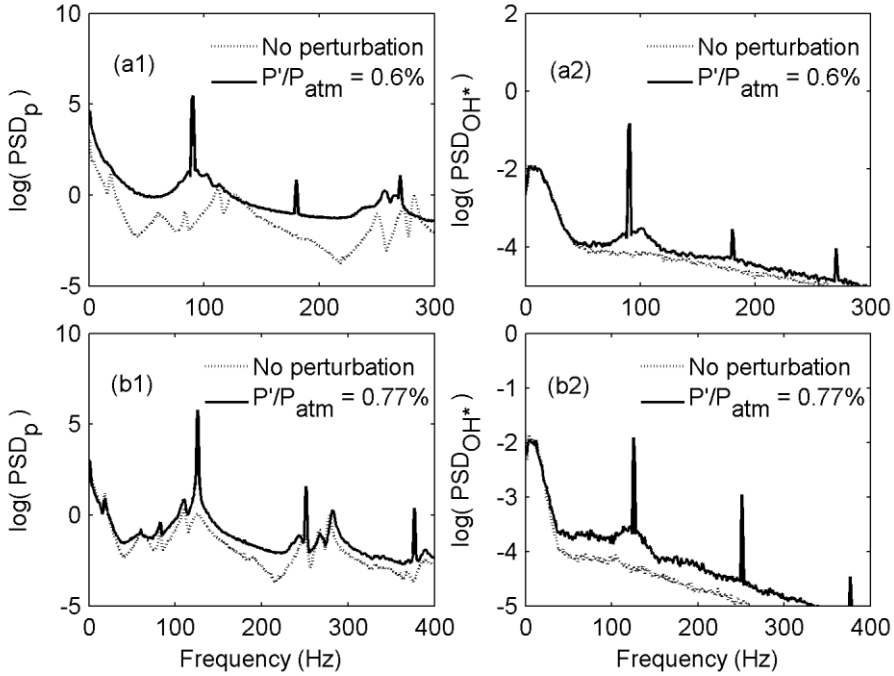

Figure 4.1. Logarithm values of the PSD of the pressure (PSD_P, with units of Pa^2/Hz) and the PSD of OH* chemiluminescence (PSD_{OH*}, with units of V^2/Hz): (a1) and (a2) show the cases with U = 5.4 m/s and f = 90 Hz; (b1) and (b2) show the cases with U = 5 m/s and f = 125.6 Hz.

The fundamental mode of flame oscillation is examined firstly. Figure 4.2 shows the normalized amplitude (OH_f/OH_{mean}), the phase, and the gain of the fundamental oscillation at different perturbation levels. The gain is defined as,

$$Gain = \frac{OH_f / OH_{mean}}{P' / P_{atm}} \tag{4.2}$$

where OH_f is the amplitude of the fundamental oscillation and OH_{mean} is the mean OH* value.

In Figure 4.2(a1) and (b1), the amplitude curves of those cases with the same Strouhal number show notable similarities. Although the absolute value is not the same,

the relative trend is characterized by the Strouhal number. Figure 4.2 (a1) and (b1) show that the cases with *St* = 0.91 have the largest amplitude and consequently have the highest gain. Among all the cases, the amplitude only changes approximately linearly when *St* = 0.32, which can be validated by the fact that the gain shown in Figure 4.2(a3) and (b3) is almost constant. In contrast, other cases all show nonlinear trends, especially when *St* = 0.64 and *St* = 0.5.

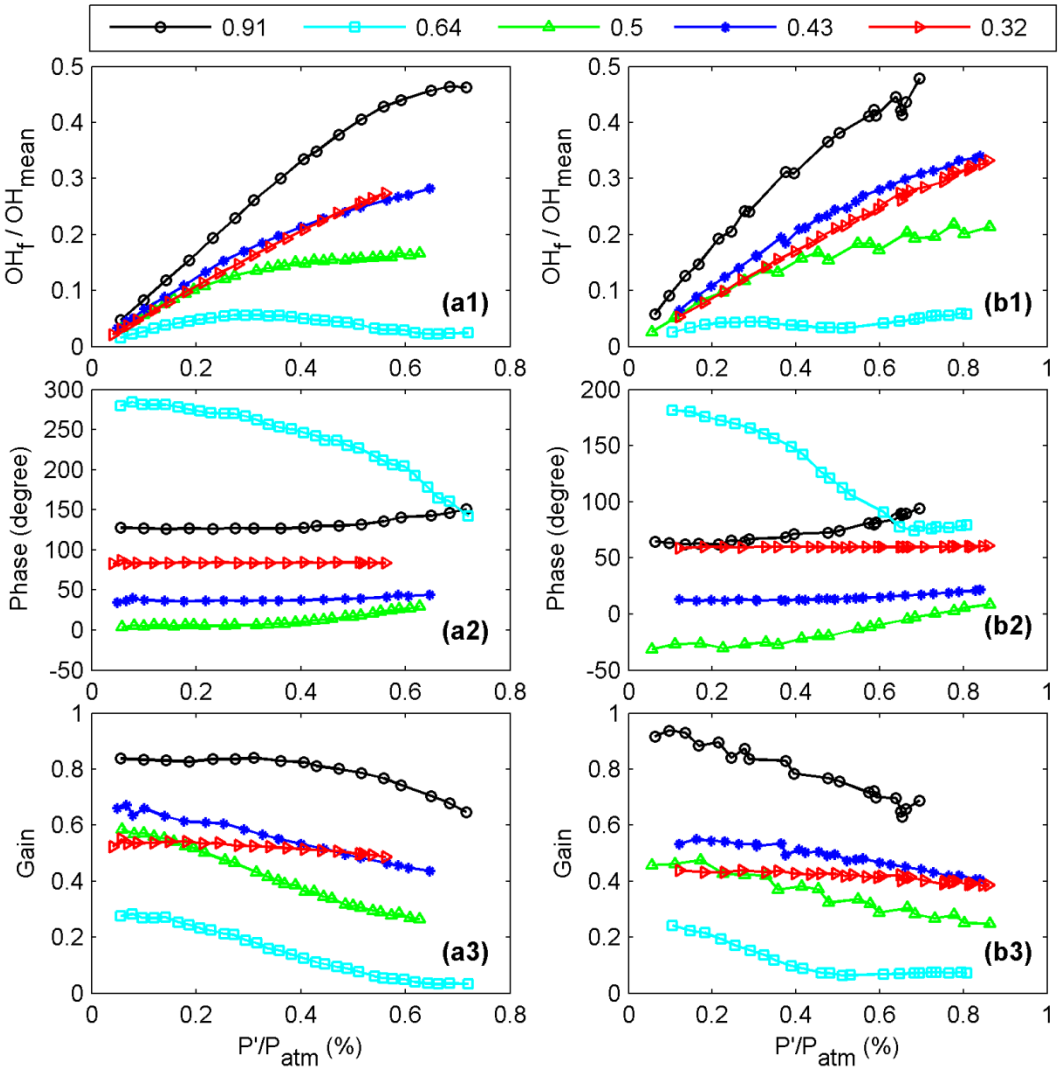

Figure 4.2. Global response of the fundamental oscillation to the acoustic perturbation with different levels, *f* = 90 Hz (left), *f* = 125.6 Hz (right).

The amplitude shows a strong dependence on *St* at the same perturbation level can be examined. When *St* decreases from 0.91 to 0.64, the amplitude drops significantly. The amplitude then increases with the decreasing St until it declines to 0.43. Following that, the amplitude only decreases slightly in the early perturbation stage when the *St* decreases from 0.43 to 0.32.

Figure 4.2(a2) and (b2) show that the Strouhal number can also generally characterize the relative positions and trends of phase curves. At *St* = 0.43 and 0.32, the phase of the fundamental oscillation is relatively stable when the perturbation level changes. Cases with *St* = 0.91 and 0.5 experience minor changes in the phase, whereas the phase changes notably when *St* = 0.64. However, Strouhal number cannot characterize the instability trend. In other words, the cases with the same Strouhal could still have different thermoacoustic instability trend. For example, when *St* = 0.91, the phases in the case with *f* = 90 Hz are larger than 90 degrees and consequently result in negative Rayleigh indexes, whereas the phases of cases with *f* = 125.6 would induce positive Rayleigh indexes when the perturbation level is less than 0.67%.

Based on the work of Balachandran [16], the energy leaking to harmonic oscillations could be one of the reasons that are responsible for the nonlinear behavior of the fundamental amplitude. Chapter 2 also demonstrated strong local harmonic oscillations in local amplitude maps. To examine the role of the first harmonic oscillation, which is the strongest in current cases, the amplitude of the first harmonic oscillation was extracted from FFT results. Figure 3.4(a1) and (b1) show the normalized amplitude of the first harmonic oscillation with respect to the mean OH* value (OH_{h1}/OH_{mean}), and Figure 3.4(a2) and (b2) show the ratio between the first harmonic oscillation and the

fundamental oscillation (OH_{h1}/OH_f). Cases have the highest value of OH_{h1}/OH_{mean} when St = 0.91, whereas the highest ratio of OH_{h1}/OH_f found in the cases with St = 0.64. The amplitudes of the harmonic oscillation are generally low when compared with that of fundamental oscillations. However, in cases with St = 0.64 first harmonic oscillation is non-negligible because its strength is comparable with that of the fundamental oscillation.

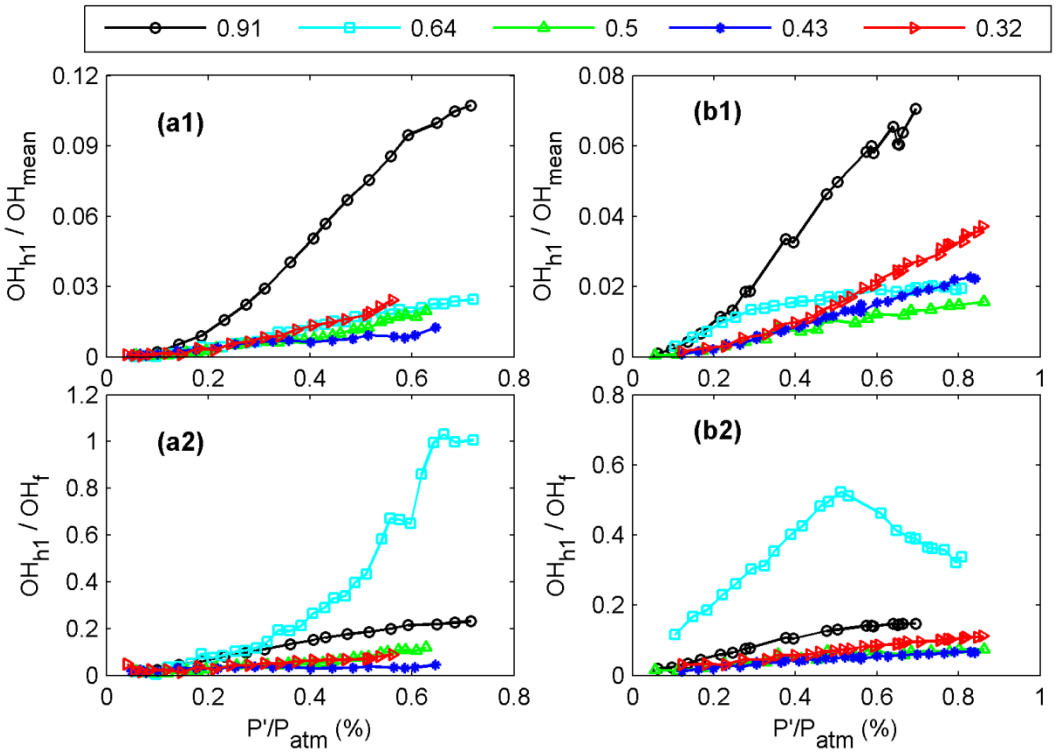

Figure 4.3. Global response of the first harmonic oscillation to the acoustic perturbation with different perturbation levels: f = 90 Hz (left), f = 125.6 Hz (right).

4.4 Flame Dynamics

Phase averaged FSD results of the cases with a perturbation frequency of 125.6 Hz were used as representatives to show the flame dynamics at different Strouhal numbers. Figure 4.4 demonstrates the results with low-level perturbations, and Figure 4.5 shows the cases with relatively high-level perturbations. The bottom of each image stands for the burner outlet. Each image has a size of 50 mm × 80 mm.

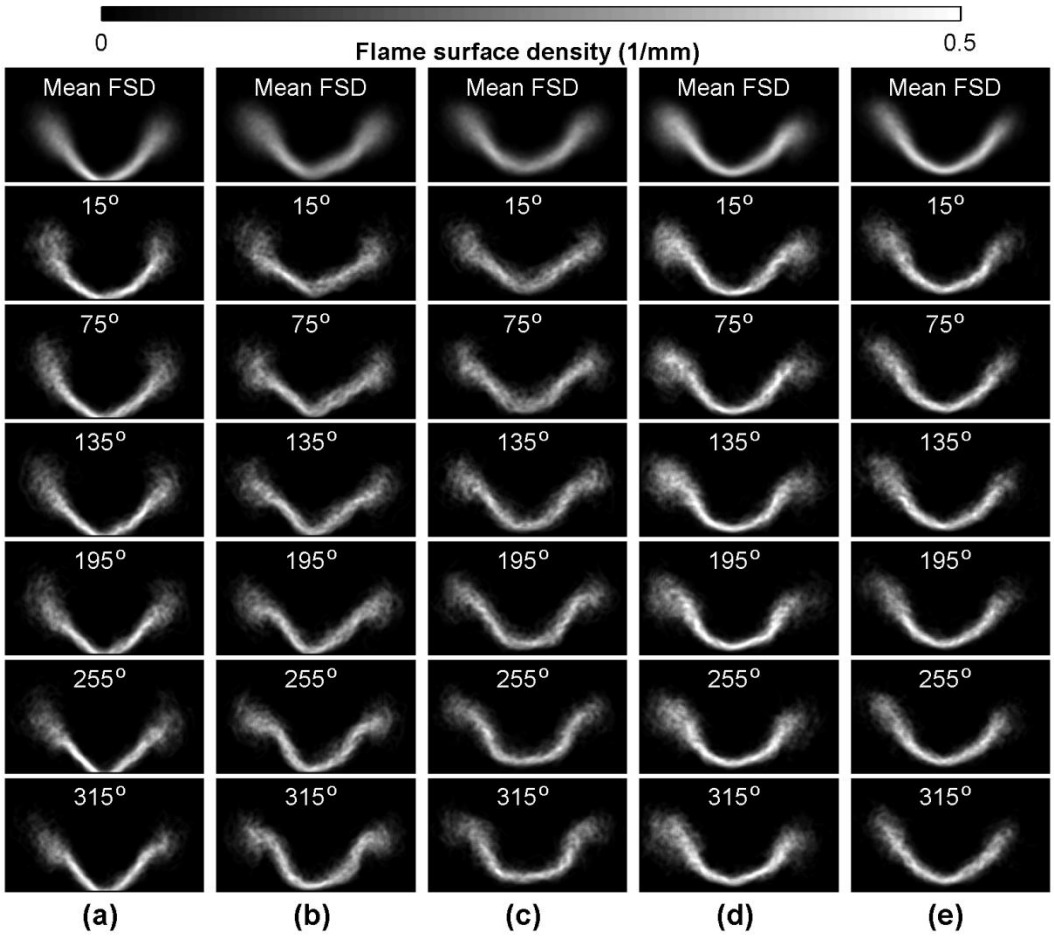

Figure 4.4. Phase-averaged FSD images of the cases with different Strouhal numbers: (a) St = 0.91, U = 3.5 m/s, P'/P_{atm} = 0.16%; (b) St = 0.64, U = 5 m/s, P'/P_{atm} = 0.18%; (c) St = 0.5, U = 6.4 m/s, P'/P_{atm} = 0.17%; (d) St = 0.43, U = 7.5 m/s, P'/P_{atm} = 0.17%; (e) St = 0.32, U = 10 m/s, P'/P_{atm} = 0.14%.

Figure 4.4 shows that when the perturbation level is relatively low, flames all oscillate mildly without significant shape deformations. The mean FSD images illustrate that the shapes of flame are similar in all cases. In contrast, Figure 4.5 illustrates that significant flame shape deformations can be detected except the case with St = 0.32. Furthermore, flames are oscillating distinctively at different Strouhal numbers. When St = 0.91, the flame shape near the burner outlet is still similar to the low perturbation case shown in Figure 4.4(a), whereas the downstream flame shape is significantly broadened.

The flame is notably enlarged when *St* = 0.64 and 0.5, which is the result of the flame roll-up process shown in Figure 4.5(b) and (c). In contrast, the flame shape is relatively less enlarged when *St* = 042, which is because the flame deformation is weaker than that of the cases with *St* = 0.64 and 0.5.

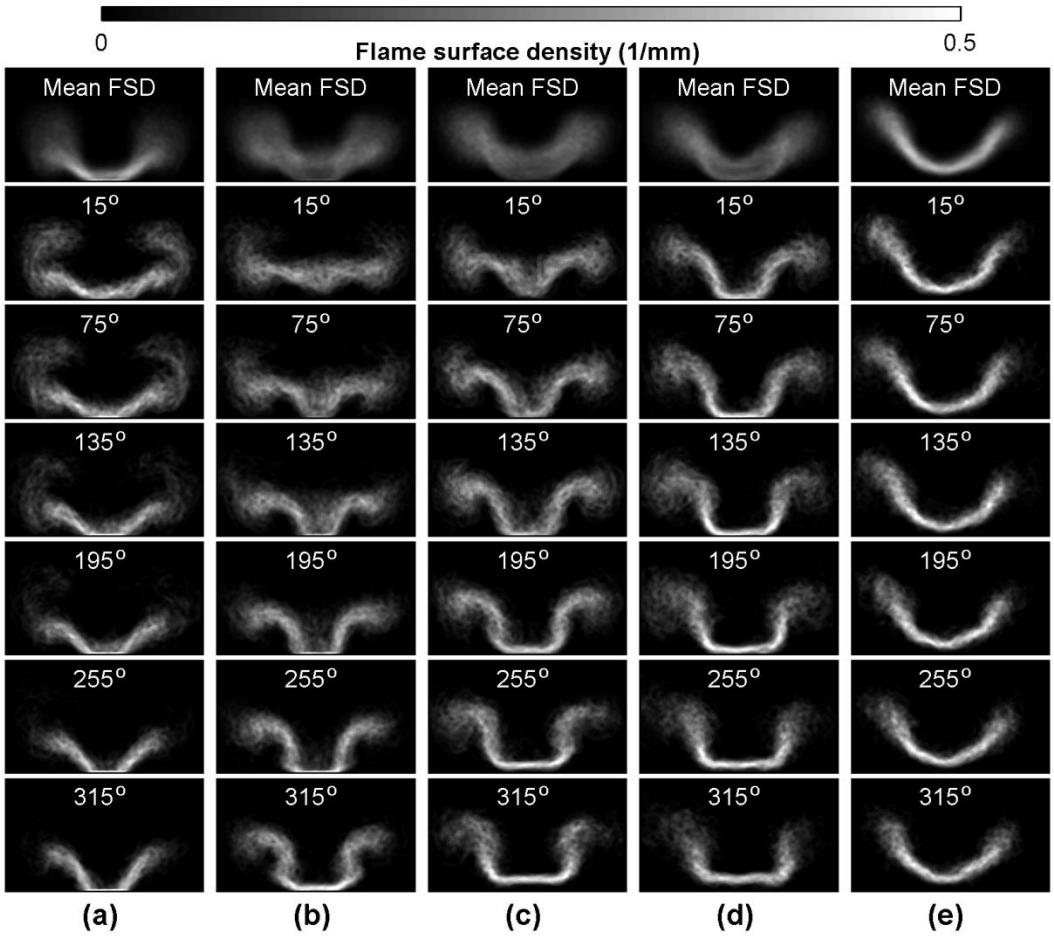

Figure 4.5. Phase-averaged FSD images of the cases with different Strouhal numbers: (a) *St* = 0.91, *U* = 3.5 m/s, P'/P_{atm} = 0.66%; (b) *St* = 0.64, *U* = 5 m/s, P'/P_{atm} = 0.78%; (c) *St* = 0.5, *U* = 6.4 m/s, P'/P_{atm} = 0.8%; (d) *St* = 0.43, *U* = 7.5 m/s, P'/P_{atm} = 0.84%; (e) *St* = 0.32, *U* = 10 m/s, P'/P_{atm} = 0.75%.

One interesting phenomenon to notice is that although the cases with St = 0.64 and 0.5 show significant shape deformations, the global flame oscillations are relatively weak in these two cases shown in Figure 4.2(a1). This phenomenon will be analyzed in

detail in a later section. Beyond the phase-averaged results, two single-shot OH-PLIF images are illustrated in Figure 4.6 to show that the enhanced acoustic perturbation can induce flame front roll-up when St = 0.64. The flow field measurements of the low swirl burner have demonstrated clear shear layers along the flame edge [73], which implies that the flame deformation found in the current study is likely caused by vortices induced by shear layer instability.

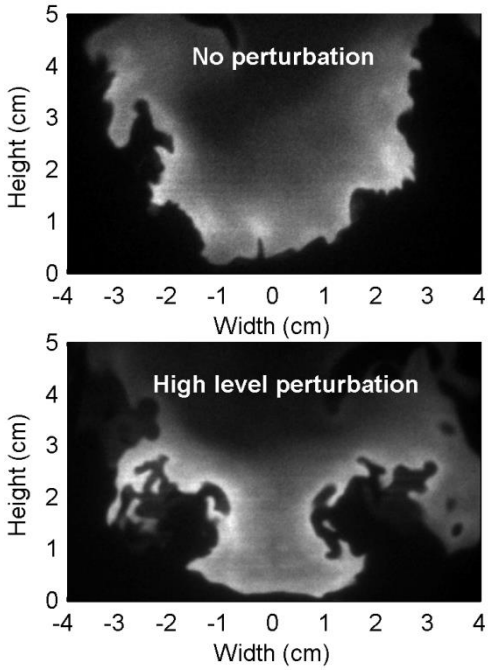

Figure 4.6. Single-shot OH-PLIF images: (top) from the U = 5 m/s cases under no acoustic perturbation condition, (bottom) from the 105 degree phase-bin of the case with U = 5 m/s, f = 125.6 Hz, and P'/P_{atm} = 0.78%.

Based on the analysis of flame dynamics, the assumption that the current flame experiences axisymmetric disturbance can be further verified. It shows that the frequency of the flame roll-up is approximately the same as the perturbation frequency. This implies that the vortex shedding frequency, which is determined by the acoustic forcing, dominates the flame roll-up process. Although the azimuthal disturbance (e.g., with an azimuthal wavenumber = 2) could also generate symmetric structures, the rotational

frequency of the vortex does not have a clear relationship with the longitudinal perturbation frequency. Therefore, the flame doesn't experience a strong azimuthal disturbance in the current tests. One of the reasons is that the longitudinal forcing can inhibit the asymmetric oscillations in the flame [33].

The current flame shape deformation is also most likely related to the convection velocity of the vortex. When the vortex moves faster in high-velocity cases, it will transfer out of the combustion region without significantly affecting the flame height. Otherwise, slow vortex convection velocity will result in a longer resident time and subsequently induce a notable height variation and a higher level of oscillation. Similar results have also been demonstrated in the work of P. Palies [45].

4.5 Local Analysis Based on POD Analysis

Figure 4.7 shows the local amplitude and phase maps of the fundamental oscillation of the cases with a forcing frequency of 125.6 Hz. In the phase maps, values between $-3\pi/2$ and $-\pi/2$ can result in negative Rayleigh indexes, whereas phases between $-\pi/2$ and $\pi/2$ induce positive Rayleigh indexes. The forcing level (P'/P_{atm}) of each case locates in the upper-left corner of each image.

Figure 4.7(a) illustrates that the flame broadens when the perturbation level increases. When P'/P_{atm} = 0.16%, the amplitude maps demonstrate a two-layer structure separated by a node region that is similar to the flame shape. Meanwhile, a boundary can be detected between the positive and negative coupling phases around the same location where the node exists. Nevertheless, in phase maps, the phase distribution of the upstream is different from that of the downstream. In the upstream region with a vertical position less than approximately 2 cm, phases are different in each oscillation layer, whereas the

downstream phases are relatively uniform. It is because the flame front bending induces upstream oscillation; however, the flame height oscillation dominates the downstream oscillation.

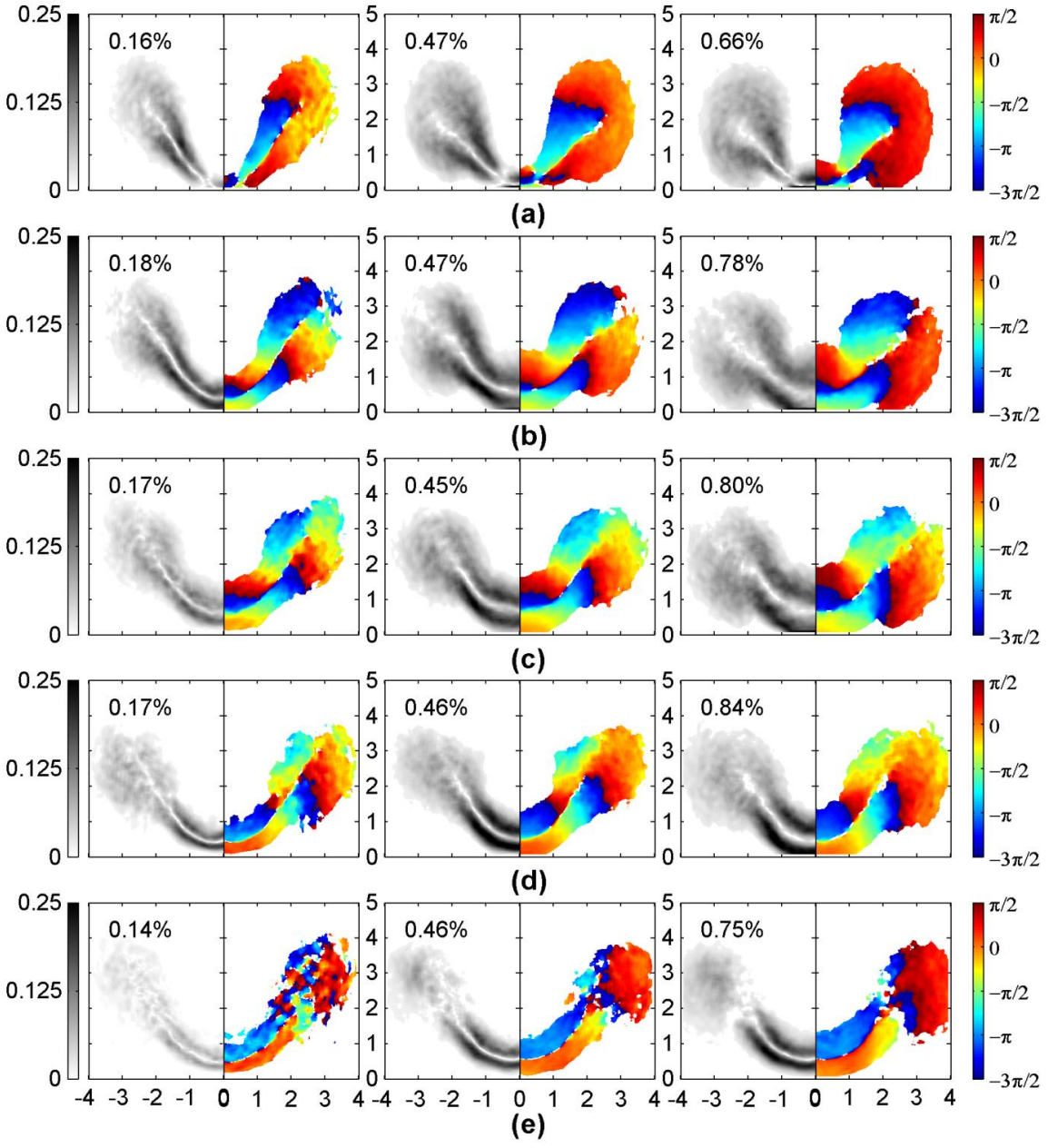

Figure 4.7. Local amplitude (left in each image, with units of mm^{-1}) and phase (right in each image) maps of the fundamental oscillation of the cases with different Strouhal numbers: (a) *St* = 0.91; (b) *St* = 0.64; (c) *St* = 0.5; (d) *St* = 0.43; (e) *St* = 0.32.

Figure 4.7(b) and (c) show the local results of cases with *St* = 0.64 and 0.5, respectively. A node region that separates two oscillation layers is also shown in amplitude maps. Moreover, phase maps illustrate periodically distributed regions in each layer. It indicates that the flame front bends to different directions at different locations instead of moving as a whole. Figure 4.7(a) - (d) illustrates that at low perturbation levels, the amplitude maps demonstrate similar shapes. It is because the flame still oscillates around its neutral position without significant front roll-up.

Figure 4.7(e) shows the local amplitude and phase maps when *St* = 0.32. Phase distributions with similar shapes are detected under different levels of forcing. It is because that the flame tends to oscillate as a whole without a notable bending of the flame front. Furthermore, it can be noticed that the negative coupling phase region is weaker than the positive coupling phase region, which results in the positive coupling dominates the flame response when *St* = 0.32.

When *St* = 0.32 and *St* = 0.91, the phase distribution is relatively uniform in each layer found in the amplitude map. On the other hand, when *St* = 0.43, 0.5 and 0.64, the region with positive coupling phases and the region with negative coupling phases distribute periodically in each layer. The difference in the phase distribution can be used to explain the difference found with the amplitude curves illustrated in Figure 4.2. Global heat release oscillations based on FSD results were rebuilt to show the contribution of local oscillations to the global fluctuation. Only the cases shown in the third column of Figure 4.7 were used. Based on Figure 4.5, the current flame oscillation can be assumed to be quasi-symmetric. Subsequently, the global fluctuation was calculated with the local oscillation that was weighted by the distance from the local position to the center of the

flame. Three types of global oscillations were rebuilt based on the phase map: Σ'_p was calculated from the local oscillations that have positive coupling phases, Σ'_n was calculated from the local oscillations with negative coupling phases, and Σ'_{total} is the total FSD oscillation that equals the summation of Σ'_n and Σ'_p. Then all the results were normalized with Σ_{mean} that was calculated from the mean FSD image.

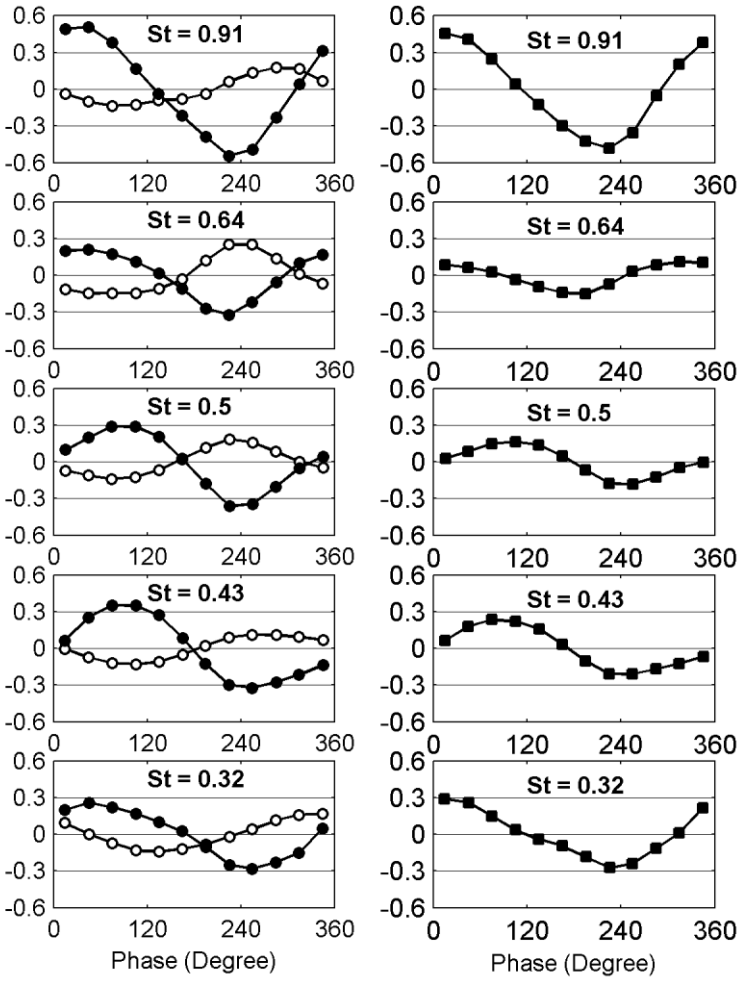

Figure 4.8. Global fundamental oscillations calculated from phase average FSD: (left) closed circles stand for Σ'_p/Σ_{mean}, open circles denote for Σ'_n/Σ_{mean}; (right) $\Sigma'_{total}/\Sigma_{mean}$.

Figure 4.8 shows the rebuilt global FSD oscillations. When St = 0.91, Σ'_p/Σ_{mean} has a much higher amplitude than that of Σ'_n/Σ_{mean}, which causes the positive coupling oscillation dominates the global oscillation. On the other hand, values of Σ'_p/Σ_{mean} are

comparable in the rest cases. Therefore, $\Sigma'_{total}/\Sigma_{mean}$ is mainly affected by the amplitude and phase of Σ'_n/Σ_{mean}. At St = 0.64, these two types of oscillation are nearly out-of-phase and have comparable amplitudes, so the global oscillation shows the lowest amplitude. This can explain the phenomenon that the local oscillation is intense, but the global oscillation is weak. Nevertheless, when St = 0.32, these two types of oscillation have comparable amplitudes, but the phase difference is less than that of the case with St = 0.64, so the global amplitude is stronger than that of the case with St = 0.64. When St = 0.5 and 0.43, although the two types of oscillation are approximately out-of-phase, Σ'_p/Σ_{mean} is stronger than Σ'_n/Σ_{mean}, which results in a moderate oscillation level. A similar analysis has been demonstrated in the work of Palies [45], which shows that the phase difference between the upper flame and lower flame oscillations plays an important role in determining the amplitude of the global heat release oscillation.

Local harmonic oscillation maps of the cases with f = 125.6 Hz were shown in Figure 4.9. It can be noticed that strong harmonic oscillations mainly exist in the cases with relatively high Strouhal numbers and high perturbation levels. When the perturbation level is low (< 0.18%), most of the detected harmonic oscillations are likely to be the noise induced by turbulence. It appears that strong harmonic oscillations are also closely associated with the deformation of the flame shape. Furthermore, as shown in Figure 4.9(b-d), the most intense harmonic oscillations mainly exist near the node region found in the amplitude maps of the fundamental oscillations. The contribution of local harmonic oscillations to global harmonic oscillation could also be affected by the phase distribution, but it hasn't been quantitatively analyzed because it is unclear that whether the harmonic oscillations are symmetric or not. Compared with the local fundamental

oscillation, the strength of the local first harmonic oscillation is relatively weak. It implies that the harmonic mode is less likely be the main factor affecting the fundamental oscillation. However, the role of the harmonic oscillation becomes non-negligible when intense local oscillations tend to cancel each other out. The formation of the harmonic oscillation is still not clear. It could be related to the harmonic oscillation associating with the flow field, or is caused by the way in which the flame oscillates.

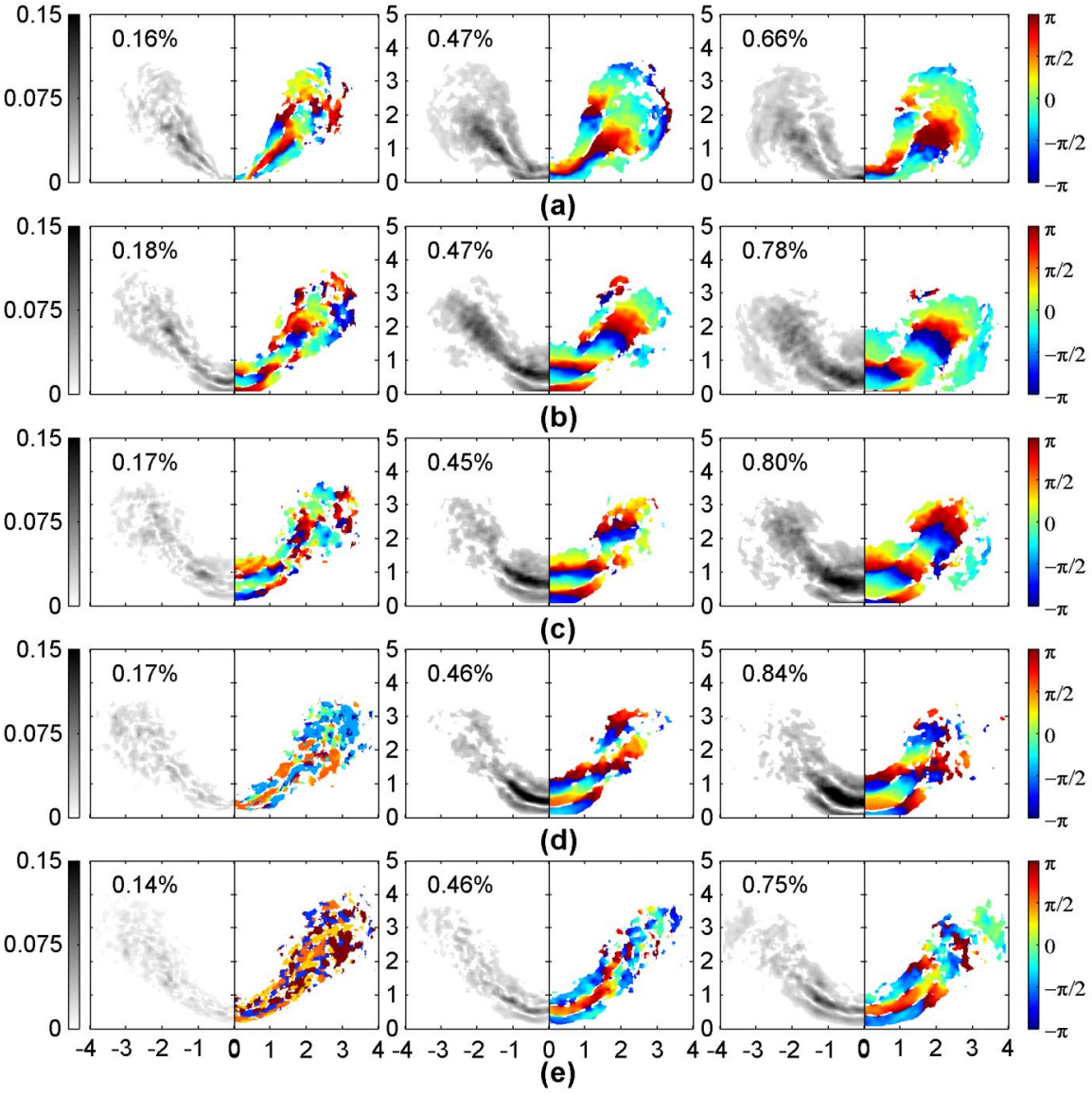

Figure 4.9. Local amplitude (left in each image, with units of mm^{-1}) and phase (right in each image) maps of the local first harmonic oscillation: (a) *St* = 0.91; (b) *St* = 0.64; (c) *St* = 0.5; (d) *St* = 0.43; (e) *St* = 0.32.

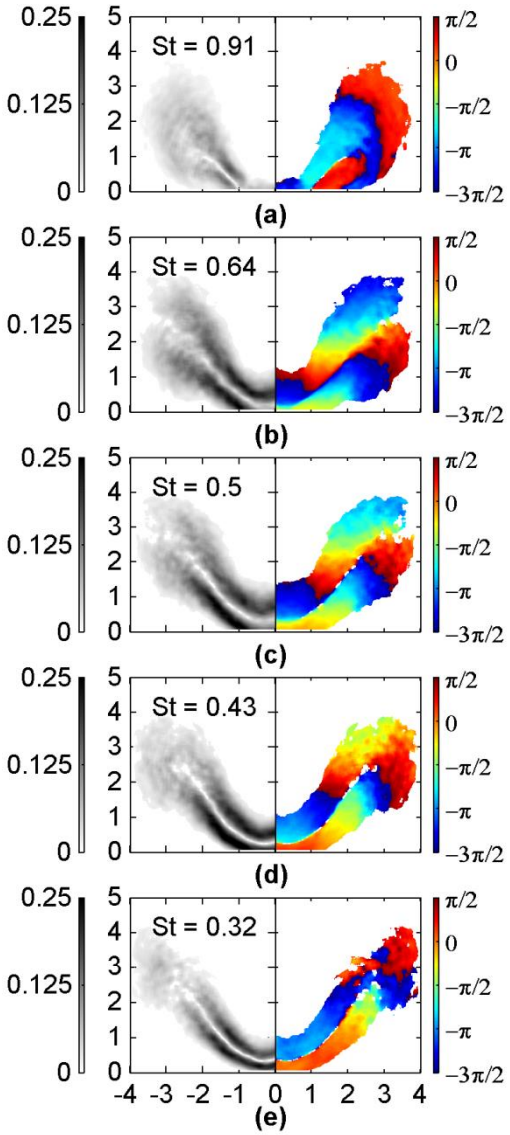

Figure 4.10. The local amplitude and phase maps of cases with a perturbation frequency of 90 Hz: (a) P'/P_{atm} = 0.47%; (b) P'/P_{atm} = 0.48%; (c) P'/P_{atm} = 0.47%; (d) P'/P_{atm} = 0.46%; (e) P'/P_{atm} = 0.47%.

Finally, Figure 4.10 shows the local maps of the cases with f = 90 Hz. Compared to the maps shown in the second column of Figure 4.7, similar amplitude and phase distributions are found in all cases except the case with St = 0.91. The similarity explains the trends observed in Figure 4.2 between the cases with f = 125.6 Hz and the cases with f = 90 Hz. The difference in cases with St = 0.91 mainly exists in phase maps, which is that

the oscillation in the out-layer shown in Figure 4.7(a) is not dominated by a single type of phase. This phenomenon is consistent with the phase differences found in Figure 4.2(a) and (b) when St = 0.91.

4.6 Conclusions

The current study has examined the global and local flame responses to acoustic perturbations with cases at different Strouhal numbers. Both local and global analyses illustrate that the Strouhal number is useful in characterizing the trend of the global and local flame oscillations, especially the oscillation amplitude. Flame dynamics analysis demonstrates that the flame deformation shows notable differences among the cases with different Strouhal numbers when the perturbation level is high. The flame shows significant changes in the mean shape when intense flame roll-up is detected; otherwise, the flame only shows a weak shape deformation.

The local analysis demonstrates that large scale flame deformations can result in intense local fundamental oscillations with high amplitude. However, the contribution of the local oscillation to global fluctuation is affected by the phase distribution that is characterized by the Strouhal number. With the assistance of the local phase map, the global oscillation with negative coupling phases and the global oscillation with positive coupling phases were rebuilt. These two types of oscillation tend to cancel each other if they are out-of-phase and have a comparable strength, which subsequently results in a low-amplitude global oscillation; otherwise, the amplitude of the global oscillation is relatively high.

The strength of the first harmonic oscillation increases globally and locally with the perturbation level. The intensity of local harmonic oscillations closely associates with

the scale of flame deformation. However, its global strength is much weaker than that of the fundamental oscillation. Only when the perturbation level is sufficiently high, the first harmonic mode could have a comparable level with that of the fundamental oscillation if the local fundamental oscillations tend to cancel each other out.

CHAPTER 5
SELF-EXCITED THERMOACOUSTIC INSTABILITY

Previous work employed the artificial acoustic perturbation to decouple the dependence of pressure oscillation on heat release fluctuation. It gives us the advantage to focus on the flame to understand how flame shape deformation affects the heat release oscillation. However, the pressure oscillation and heat release oscillation are highly coupled when real thermoacoustic instability occurs. Acoustic modes related to the combustor geometry got lots of attention in many previous works, but they haven't examined the role of flame in detail. Recent studies have demonstrated that the oscillation modes are strongly dependent on flame characteristics, such as the fuel type [23]. However, the effect of flame features has still not been fully examined. Therefore, the current study will focus on the instability trend associated with flame features. To change the flame feature, the method used in the current study is blending hydrogen with methane, which has been shown to be an efficient way in previous works. The first part of this chapter will talk about an experimental study of the self-excited thermoacoustic instability.

The other part of this chapter talks about predicting the unstable modes of the combustor with a one-dimensional model. An n-τ model is utilized to represent heat release oscillation. The particular focus is on examining the effect of flame gain (n) and the delay (τ) on the oscillation mode. Furthermore, this chapter will also discuss the advantages and the disadvantages of the current heat release mode.

5.1 Experimental Configuration

Figure 5.1 shows the schematic of the experimental configuration designed for examining the self-excited thermoacoustic instability. The current experiment used a low swirl burner (LSB), which is the same one used in acoustic perturbation studies. The following is a detailed description of the test configuration.

5.1.1 Combustor

The main part of the test configuration is a combustor. When using the plate for burner installation as a reference location, the combustor can be divided into an upstream section and a downstream section. The combustor is designed for three main goals. The first is that the combustor should enable successful self-excited thermoacoustic instability while minimizing the effect on the flame stabilization mechanism. The second one is that the natural acoustic modes of the combustor should be able to change, which allows the features of the flame-acoustic interaction to be examined in a relatively wider range. The third goal is that the combustor should have clearly defined acoustic boundary conditions, which will provide a great convenience for one-dimensional modeling analysis.

Lots of effort had been contributed to achieving the first goal. It was found that the inner diameter of the downstream chamber plays an important role in determining whether the instability will happen or not. A chamber with a large inner diameter could not have oscillations because the high dissipation of acoustic energy, which subsequently causes a failure of triggering thermoacoustic instability. Moreover, a chamber with a small inner diameter should also be avoided because it will introduce a strong flame-wall interaction, which substantially changes the flame stabilization mechanism. After a series

of tests, tubes with an inner diameter of 101.6 mm (4 inches) was chosen for use in the current test.

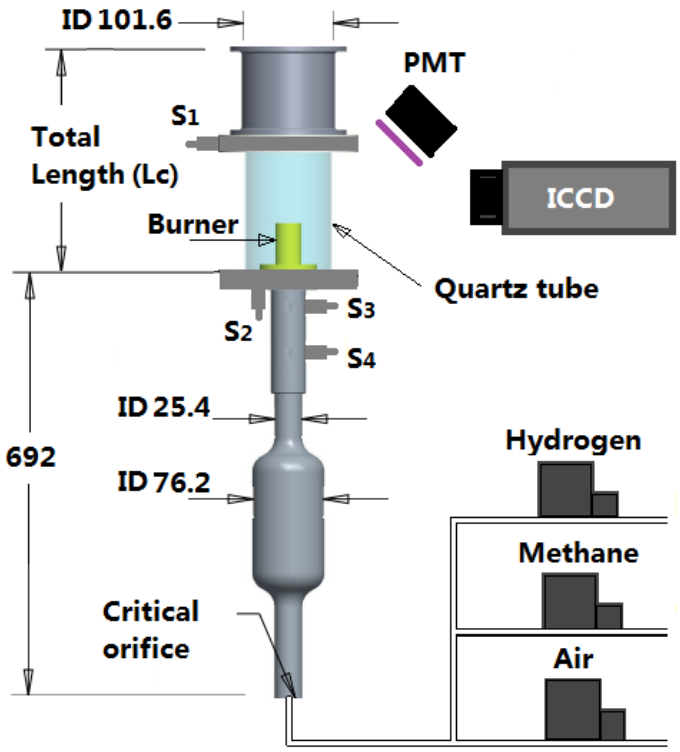

Figure 5.1. Schematic view of the experimental configuration.

The upstream section of the combustor has a fixed length of 692 mm, so the natural acoustic modes of the chamber are only changed by varying the downstream chamber length (L_c). In the downstream section, a quartz tube with an inner diameter of 101.6 mm and a length of 300 mm is used for flame imaging. The total length of the downstream part (L_c) varies by connecting steel tubes with different lengths to the quartz tube section. In the current study, five steel tubes with different lengths were used. The lengths of the metal tubes are 200, 250, 300, 350, and 400 mm. Therefore, L_c can change from 300 mm up to 1800 mm. However, limited by the height of the roof, the maximum L_c used is 1300 mm.

The current combustor design also facilitates the one-dimensional thermoacoustic modeling that is based on the one-dimensional acoustic modeling. Tubes were selected for use because they are axisymmetric about the center axis, and the geometry is suitable for the one-dimensional assumption. Moreover, the combustor has clearly defined acoustic boundary conditions. The upstream section uses a critical orifice as the inlet to provide a closed-end acoustic boundary condition, under which the velocity oscillation is negligible. Besides, the pressure fluctuation is assumed to be zero at the chamber outlet that is connected to atmosphere, which is considered as an open-end boundary condition.

5.1.2 Diagnostics

Four piezoelectric pressure sensors (PCB 112A) are installed at four different locations. The pressure sensors were operating with a sampling rate of 20 kHz, a sensitivity of 0.16 mV/psi, and a resolution of 0.028 kPa. A photomultiplier module (Hamamatsu H8249-101) equipped with a narrow bandpass filter (308 ± 10 nm) was utilized to record the global OH* chemiluminescence at the same sampling rate as the pressure sensor. An ICCD camera (Princeton Instruments) equipped with a bandpass ultraviolet (UV) filter was employed to capture OH* chemiluminescence images. The ICCD camera was set to capture images in a 103 mm × 103 mm region with a resolution of 512 × 512 pixels. When images were processed, only a 50 mm × 67.4 mm region was used because the flame length was less than 50 mm in current tests.

5.1.3 Flow Control

Methane and air flows were controlled with Hastings flow controllers with an accuracy of 0.2% of full scale plus 0.5% of reading values. The hydrogen flow was adjusted with an Omega mass flow controller (Omega 5400) with an accuracy of ±1.5%.

The fuel blends and the air were mixed in a pipe with a length of 500 mm and then flew through the critical orifice that has an inner diameter of 2.54 mm (0.1 inches). In the current study, the fuel blends and the air are considered as fully premixed, so the equivalence ratio oscillation in the test section is negligible.

5.2 Operating Conditions

The operating conditions are listed in Table 5.1. The equivalence ratio was kept at 0.7, and the bulk velocity was maintained at 5.5 m/s.

During the test, the percentage of hydrogen was carefully adjusted to avoid flame attachment to the burner and flashback, which may happen when the hydrogen percentage (η_H) is sufficiently high.

Table 5.1 Operating conditions

L_c (mm)	Hydrogen Percentage, η_H (%)
300	0, 5, 10, 15, 20, 25, 30 ,35, 40
500	0, 5, 10, 15, 20, 25, 30 ,35, 40
700	0, 5, 10, 15, 20, 25, 30 ,35, 40
900	0, 5, 10, 15, 20, 25, 30 ,35, 40
1000	0, 5, 10, 15, 20, 25, 30 ,35, 40, 45, 50, 55
1100	0, 5, 10, 15, 20, 25, 30 ,35, 40, 50

It can be noticed that the cases with L_c = 1000 mm and 1100 mm have a maximum η_H of 50% and 55%, respectively, which is for examining the high-frequency modes detected at L_c = 1000 mm and 1100 mm. In contrast, the other cases only use a maximum η_H of 40% for safety concerns.

5.3 Experiment Results

5.3.1 Flame Structure

Figure 5.2 illustrates averaged OH* chemiluminescence images of stable flames with the hydrogen percentage of 0%, 10%, 20%, 30%, and 40%. It can be noticed that the flame length decreases with an increasing hydrogen percentage. Furthermore, the local OH* intensity increases when more hydrogen is added. Similar phenomena are also detected in the research of Cheng, et al. [82]. Even though the shape is changed, the OH* distribution still shows a bowl-like shape in all cases, which is important because it can be assumed that the flame stabilization mechanism is still the same.

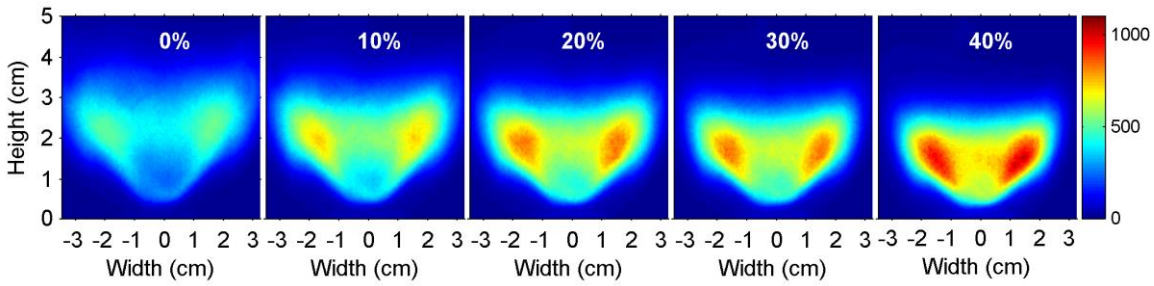

Figure 5.2. Averaged OH* chemiluminescence images under stable conditions (Abele transfer needed).

5.3.2 Pressure Oscillation

Figure 5.3 shows the power spectral density of the pressure oscillation at different chamber lengths. In the current study, there is no thermoacoustic instability when L_c = 500 mm, so the results are not shown here. Figure 5.3(a) shows that when L_c = 300 mm, the only notable pressure oscillation is detected at η_H = 40%. When L_c changes to 700 mm, intense oscillations are detected in all cases when the η_H is larger than 10%. Figure 5.3(c) illustrates that instability is detected in all cases when L_c = 900 mm. Similarly, a higher hydrogen percentage tends to inhibit pressure oscillation when L_c =

1000 and 1100 mm. When L_c = 1000 mm the pressure oscillation is only detected when the hydrogen percentage is less than 30%.

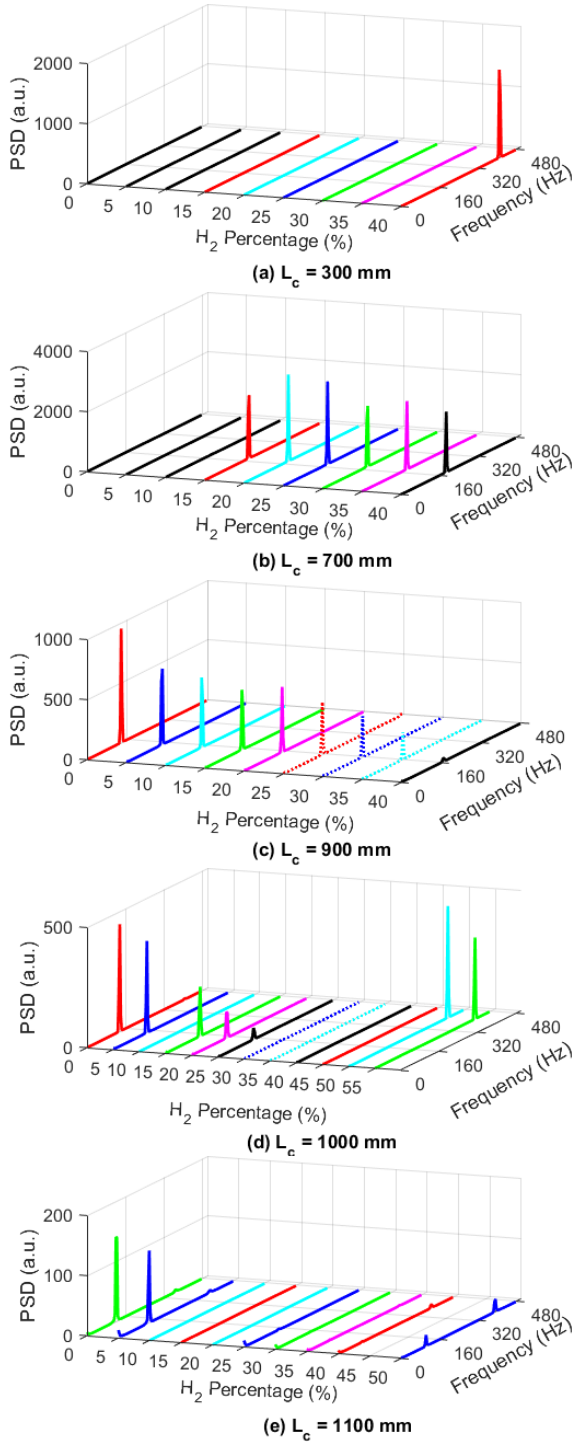

Figure 5.3. Power spectral density (PSD) of the pressure oscillation at different tube lengths.

However, when the hydrogen percentage increases to 50%, strong high acoustic modes are detected at 411 Hz and 415 Hz. Similar to the trend found in the case with L_c = 1000 mm, results with L_c = 1100 mm demonstrate detectable oscillations when η_H is either low (< 10%) or high (> 40%). In contrast, the oscillation strength is weaker in the cases with L_c = 1100 mm than that of the cases with L_c = 1000 mm. When L_c = 1100 mm, it is also interesting to notice that there are two oscillation modes (104 Hz and 392 Hz) excited at η_H = 50%. Results of pressure spectrum demonstrate that the hydrogen proportion is not only critical in determining whether the instability is excited or inhibited, but also plays an important role in affecting the oscillation frequency and amplitude.

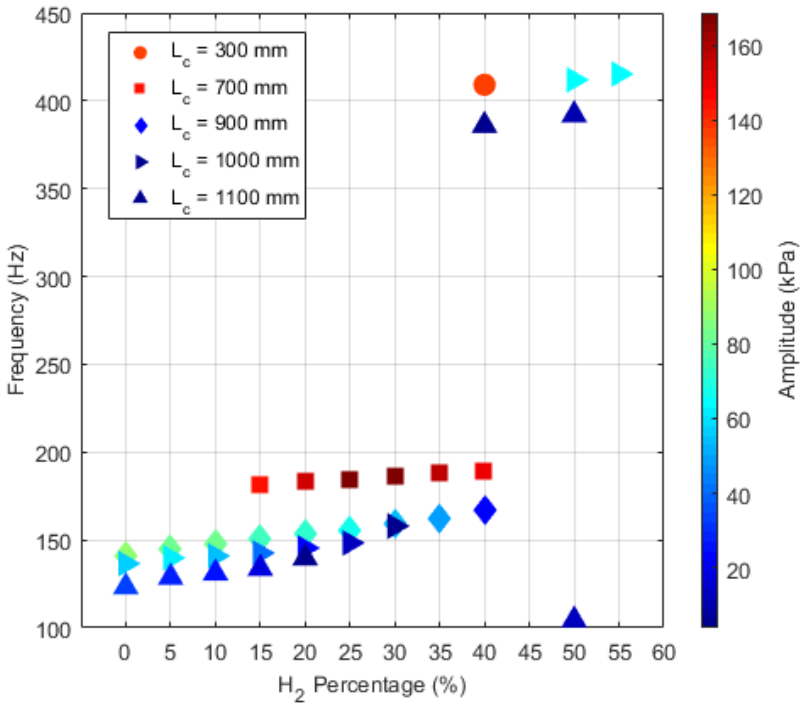

Figure 5.4. The pressure oscillation frequency and amplitude.

For cases with a detectable pressure oscillation, the oscillation frequency and amplitude are shown in Figure 5.4. In general, the oscillation frequency drops when the chamber length increases. It can be noticed that the strongest oscillation occurs at L_c = 700 mm. One the other hand, the weakest oscillation is found at L_c = 1100 mm. For a fixed chamber length, the oscillation frequency tends to increase with the increasing hydrogen percentage. Figure 5.5 shows a more detailed trend of the cases with L_c = 700 mm and 900 mm. When L_c = 700 mm, the oscillation amplitude increases in the beginning and then drops with an increasing hydrogen percentage. In contrast, the amplitude keeps declining when the hydrogen percentage increase at L_c = 900 mm. In both cases, the oscillation frequency increases with an increasing hydrogen percentage.

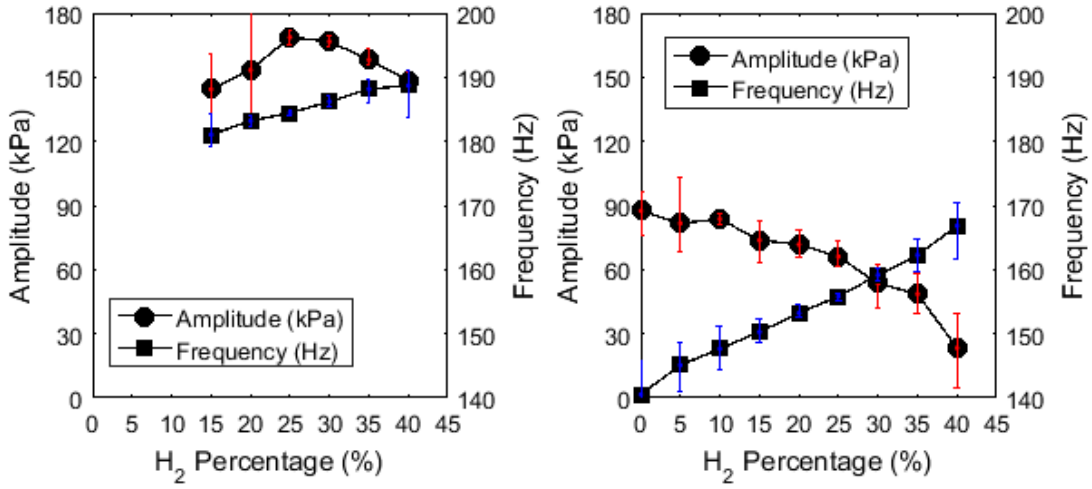

(a) L_c = 700 mm (b) L_c = 900 mm

Figure 5.5. Pressure oscillation amplitude and frequency.

It is shown in Figure 5.4 and Figure 5.5 that when the chamber length changes, cases with the same hydrogen percentage still show a significant difference in the oscillation amplitude.

5.3.3 Flame Structure and Dynamics

This section talks about the flame shape deformation associated with the self-excited thermoacoustic instability of the cases with different chamber lengths.

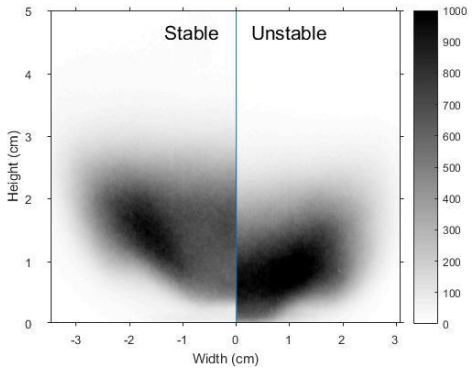

Figure 5.6. Mean OH* at L_c = 300 mm and 40% H_2.

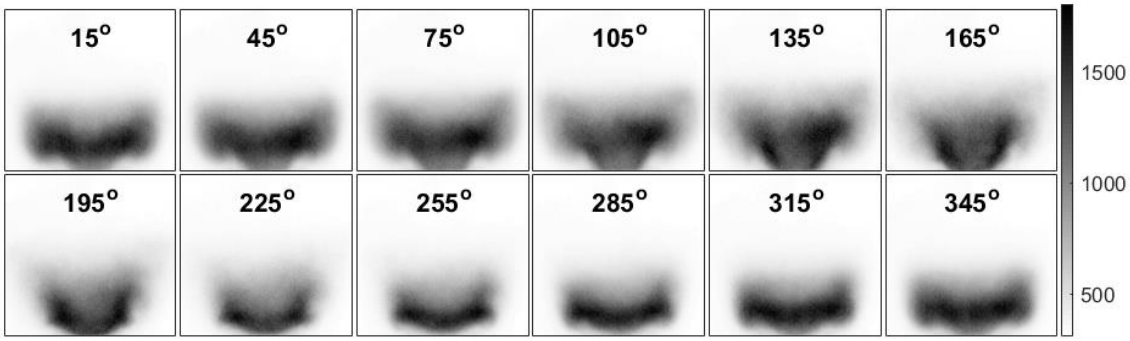

Figure 5.7. Phase averaged OH* at L_c = 300 mm and 40% H_2.

Figure 5.6 shows the mean OH* chemiluminescence of the cases under stable and unstable conditions. The flame shape experiences a notable change when thermoacoustic instability occurs. Phase-averaged results shown in Figure 5.7 illustrate that the flame experience size variation; however, no notable flame roll-up is detected. The Strouhal number of the current case is approximately 1.9, which implies that the current result is consistent with the conclusion in Chapter 4, which states that the flame roll-up is not the dominant mechanism for high Strouhal number cases.

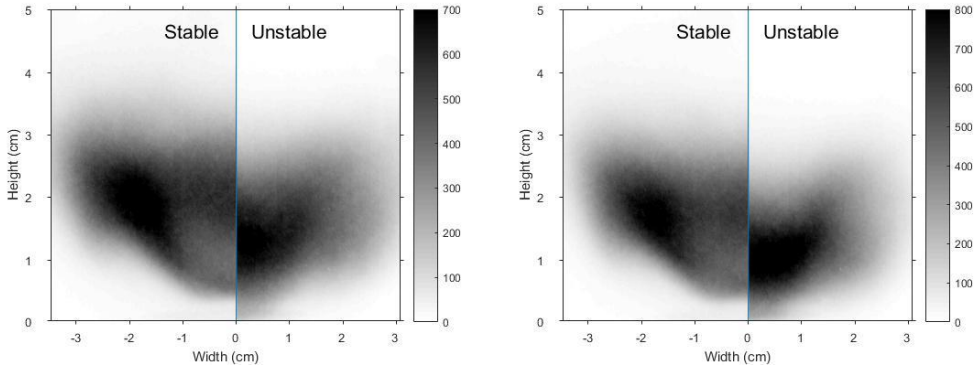

Figure 5.8. Mean OH* at L_c = 700 mm, 15% H_2 (left) and 30% H_2 (right).

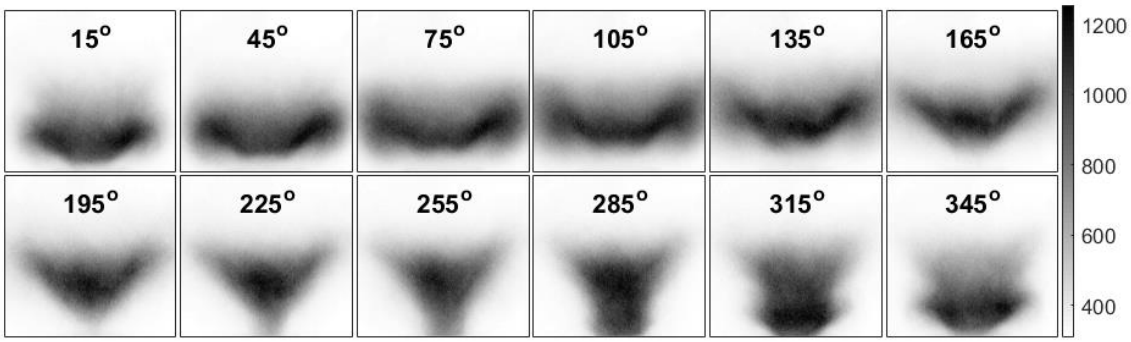

(a)

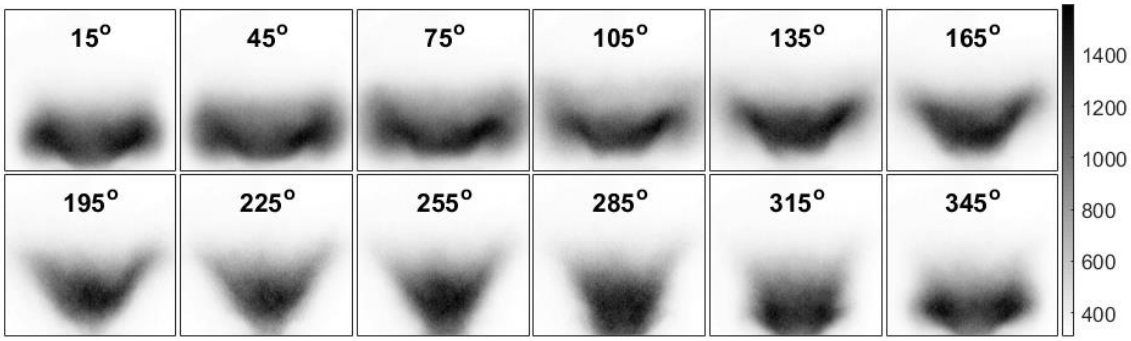

(b)

Figure 5.9. Phase averaged OH* at L_c = 700 mm, 15% H_2 (a) and 30% H_2 (b).

Figure 5.8 demonstrates the comparison of mean OH* images between unstable and stable cases. It can be noticed that flames under unstable conditions are more distributed than that without shape deformation. It results from the flame roll-up illustrated in Figure 5.9. Moreover, Figure 5.9 shows that the flame oscillation shows a

very similar trend in both cases. It is reasonable because both cases have similar oscillation frequency and oscillation amplitude.

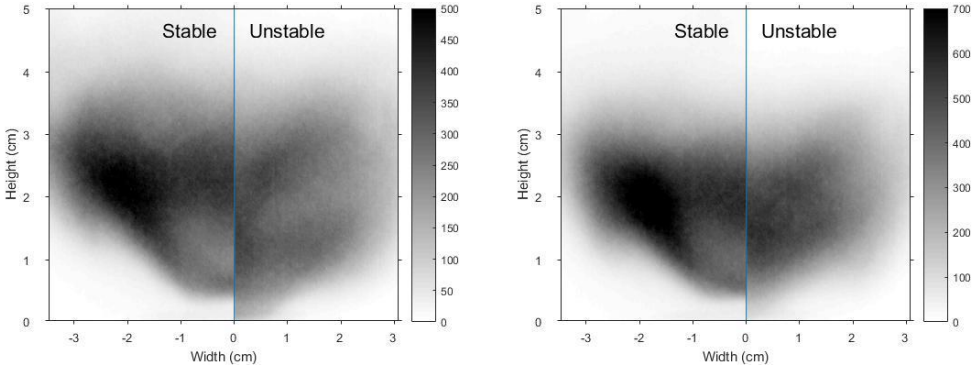

Figure 5.10. Mean OH* at L_c = 900 mm, 0% H_2 (left) and 15% H_2 (right).

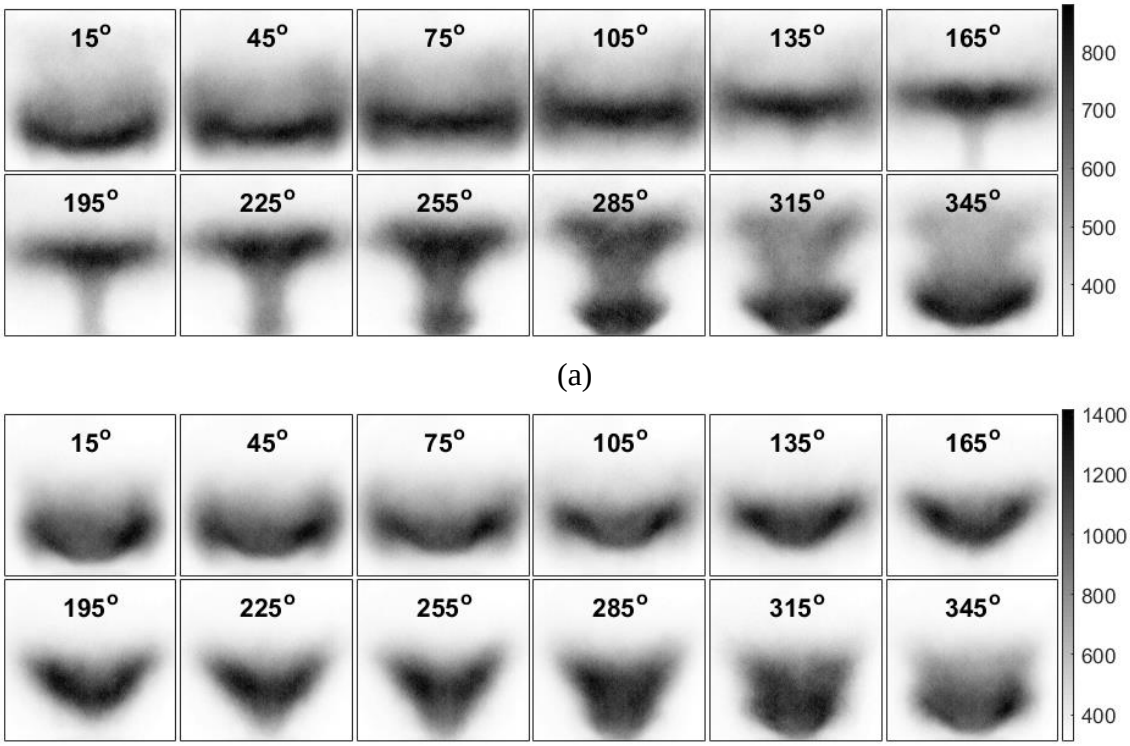

Figure 5.11. Phase averaged OH* at L_c = 900 mm, 15% H_2 and 30% H_2.

Figure 5.10 shows that the case with pure CH_4 has a stronger shape deformation and weaker local value than that of the case with 15% H_2. It is because the pressure

oscillation is stronger in the case with 0% H_2. A significant shape deformation associated with flame roll-up can be noticed in Figure 5.11. By comparing with the result shown in Figure 5.9, it shows that the oscillation scale is larger in the case with 0% H_2. However, Figure 5.3 shows that the acoustic oscillation, in fact, is stronger in the case with a relatively weaker shape deformation. It is caused by the cancellation between the local oscillations with different phases, which will be discussed in detail in a later section.

The flame oscillation shows a similar behavior when the chamber length increases to 1000 mm and 1100 mm. The result of the case with L_c = 1100 mm is provided in Appendix A.

5.3.4 Rayleigh Index Analysis

The Rayleigh Index map is calculated based the equation,

$$R^*(x,y) = \frac{1}{P_{RMS}\overline{OH^*}} \sum_{i=1}^{n} P' \cdot (OH^*)'(x,y) \tag{5.1}$$

where $R^*(x,y)$ is the local Rayleigh Index, P_{RMS} is the RMS pressure, $\overline{OH^*}$ is the averaged OH^* chemiluminescence, P' is the pressure oscillation, $(OH^*)'(x,y)$ is the local OH^* chemiluminescence oscillation, n is the total phase number, and subscript i represents the i^{th} phase. It has been shown in Chapter 3 that the local Rayleigh Index can be useful in demonstrating the general information of local flame-acoustic coupling.

Figure 5.12(a) shows that the positive Rayleigh Index dominates the local response. Figure 5.12(b) illustrates that the Rayleigh Index distribution is similar in both cases with L_c = 700 mm, whereas the stronger Rayleigh indexes can be noticed when the hydrogen percentage is 30%. Figure 5.12(c) shows result at L_c = 900 mm. It can be noticed that the positive Rayleigh index region is larger and stronger when no hydrogen

addition than that of the case with a hydrogen percentage of 30%. It means a stronger positive Rayleigh index tends to result in a stronger pressure oscillation. Moreover, relatively stronger negative zones are also detected, especially in the downstream region. By comparing Figure 5.12(b) and Figure 5.12(c), it shows that the negative zone can play an important role in canceling the effect of the positive zone. As a result, a stronger shape deformation not necessary results in a more intense global oscillation.

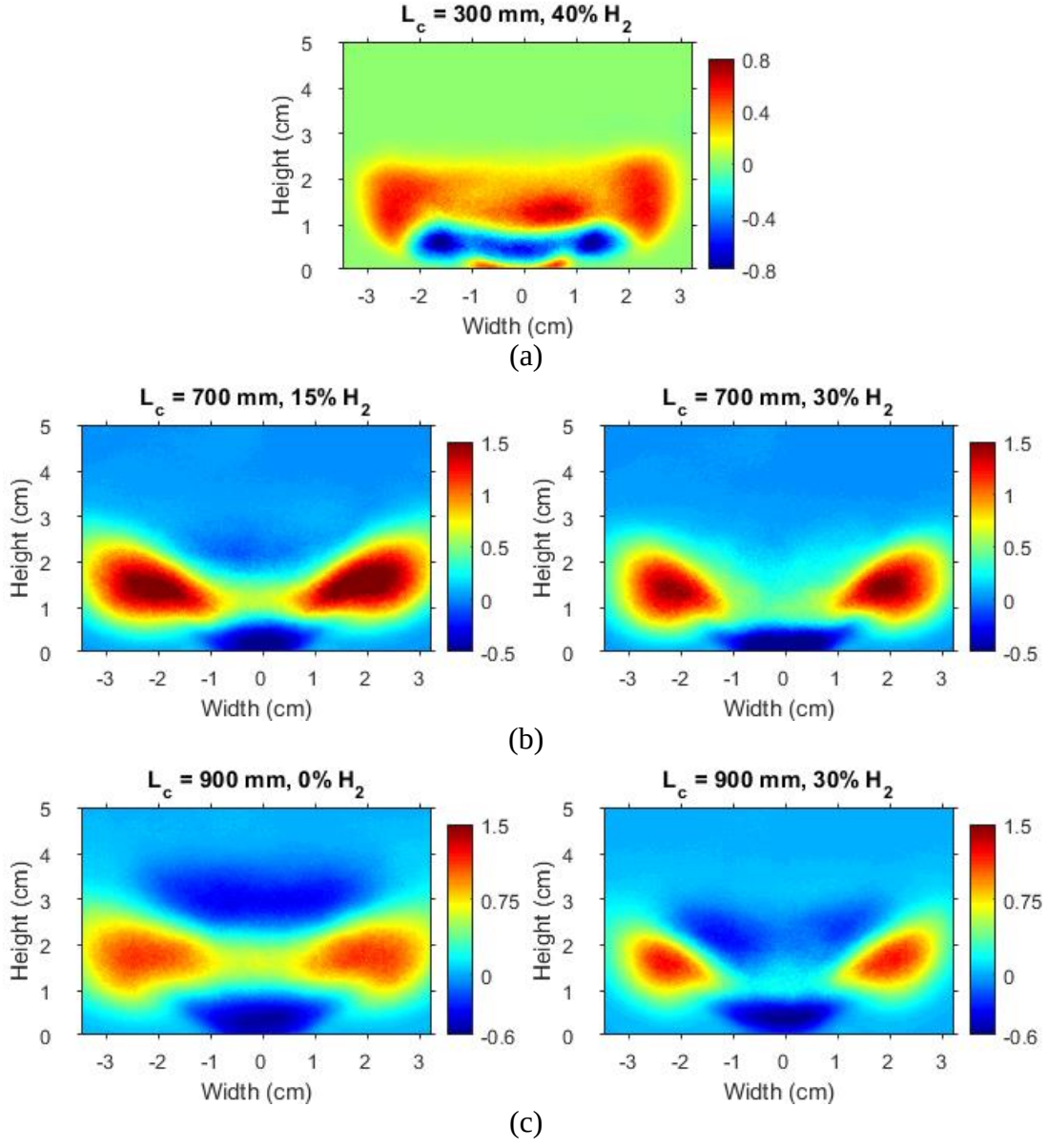

Figure 5.12. Rayleigh index maps of cases with different hydrogen concentrations.

Furthermore, all Rayleigh Index maps show a quasi-symmetric structure, which illustrates that the positive and negative zones are periodically distributed along the flow direction. It implies that the longitudinal oscillation mode still plays the dominant role in both low frequency and high-frequency modes.

5.4 Self-excited Thermoacoustic Instability Modeling

5.4.1 Basic modeling equations

For inviscid flow, the mass, momentum, and energy conservation equations are,

$$\frac{D\rho}{Dt} + \rho\nabla\cdot\vec{u} = 0 \tag{5.2}$$

$$\rho\frac{D\vec{u}}{Dt} + \nabla p = 0 \tag{5.3}$$

$$\rho\frac{D}{Dt}\left(e + \frac{1}{2}\vec{u}^2\right) + \nabla\cdot(P\vec{u}) = q + \nabla\cdot(K\nabla T) \tag{5.4}$$

where ρ is the density, $\vec{u}$ is the velocity, p is the pressure, t is the time, e is the internal energy, T is the temperature, q is the rate of the heat added per unit volume, and K is the conductivity. The detailed deduction can be found in the work of Dowling [64].

For an unsteady system, all flow variables can be divided into a mean value part and a part represents the oscillation,

$$p(\vec{x},t) = \bar{p} + p'(\vec{x},t) \tag{5.5}$$

$$\vec{u}(\vec{x},t) = \bar{\vec{u}} + \vec{u}'(\vec{x},t) \tag{5.6}$$

$$\rho(\vec{x},t) = \bar{\rho} + \rho'(\vec{x},t) \tag{5.7}$$

Finally, the fundamental equations 5.2 -5.4 can change to,

$$\frac{\bar{D}\rho'}{Dt} + \bar{\rho}\nabla \cdot \vec{u}' = 0 \tag{5.8}$$

$$\bar{\rho}\frac{\bar{D}\vec{u}}{Dt} + \nabla p' = 0 \tag{5.9}$$

$$\frac{1}{\bar{c}^2}\frac{\bar{D}^2 p'}{Dt^2} - \nabla^2 p' = \frac{\gamma - 1}{\bar{c}^2}\frac{\bar{D}q'}{Dt} \tag{5.10}$$

where the operator $\bar{D}/Dt = \partial/\partial t + \bar{u}$ and $\bar{c}$ is the mean speed of sound. γ is the specific heat ratio that is defined as c_p/c_v, where c_p is the specific heat at constant pressure and c_v is the specific heat at constant volume.

5.4.2 1D Model

The modeling work is based on a 1D acoustic model described in the work of Poinsot, et al. [7]

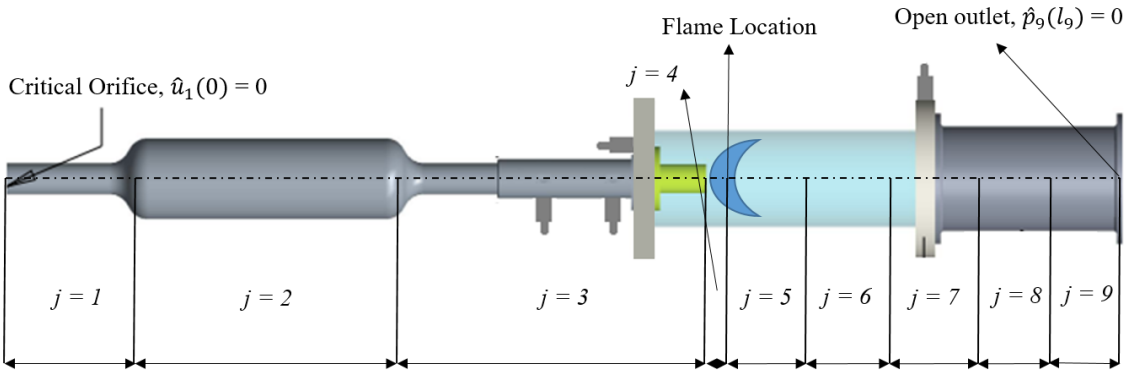

Figure 5.13. Section distribution.

The dimension of the model is shown in Figure 5.13. The pressure and acoustic velocity are described as,

$$p'(x,t) = \left(A^+ e^{ik^+ x} + A^- e^{ik^- x}\right)e^{-i\omega t} \tag{5.11}$$

$$u'(x,t) = \frac{1}{\rho c}\left(A^+ e^{ik^+ x} - A^- e^{ik^- x}\right)e^{-i\omega t} \tag{5.12}$$

where x is the location, t is the time, $p(x,t)$ is the pressure, $u(x,t)$ is the velocity, A^+ is the complex amplitude of the downstream traveling wave, A^- is the complex amplitude of the upstream traveling wave, k^+ is the wavenumber of the downstream traveling wave, k^- is the wavenumber of the upstream traveling wave, ω is the angular frequency, ρ is the density, and c is the speed of sound.

In the equation 5.11 and 5.12, $k^+ = k/(1+M)$ and $k^- = -k/(1-M)$, where M is the Mach number. Since the velocity in current tests is much smaller than the speed of sound, $M \approx 0$. As a result, $k^+ = k = -k^-$. Therefore, the equation can be re-written as,

$$p'(x,t) = \left(A^+ e^{ikx} + A^- e^{-ikx}\right) e^{-\omega t} = \hat{p}(x) e^{-i\omega t} \tag{5.13}$$

$$u'(x,t) = \frac{1}{\rho c}\left(A^+ e^{ikx} - A^- e^{-ikx}\right) e^{-\omega t} = \hat{u}(x) e^{-i\omega t} \tag{5.14}$$

In each section, the equation can be shown as,

$$\hat{p}_j(x) = A_j^+ e^{ik_j x} + A_j^- e^{-ik_j x}, x \in (0, l_j) \tag{5.15}$$

$$\hat{u}_j(x) = \frac{1}{\rho_j c_j}\left(A_j^+ e^{ik_j x} - A_j^- e^{-ik_j x}\right), x \in (0, l_j) \tag{5.16}$$

where the subscript j represents the section number and l_j denotes the length of the j^{th} section.

5.4.3 Transfer Matrix for the Sections without Flame

At the interface (except the one where the flame is located) between j^{th} and $(j+1)^{th}$ sections, the pressure and the mass flow rate of j^{th} section are considered as the same of that in the $(j+1)^{th}$ section, which can be shown as,

$$\hat{p}_j(l_j) = \hat{p}_{j+1}(0) \tag{5.17}$$

$$S_j \rho_j \hat{u}_j(l_j) = S_{j+1} \rho_{j+1} \hat{u}_{j+1}(0) \tag{5.18}$$

where S_j and S_{j+1} are the areas of j^{th} and $(j+1)^{th}$ *sections*, respectively.

Substitute equations 5.17 and 5.18 in equations 5.15 and 5.16,

$$A_j^+ e^{ik_j l_j} + A_j^- e^{-ik_j l_j} = A_{j+1}^+ + A_{j+1}^- \tag{5.19}$$

$$\frac{S_j}{\rho_j c_j}\left(A_j^+ e^{ik_j l_j} - A_j^- e^{-ik_j l_j}\right) = \frac{S_{j+1}}{\rho_{j+1} c_{j+1}}\left(A_{j+1}^+ - A_{j+1}^-\right) \tag{5.20}$$

Then, A_{j+1}^+ and A_{j+1}^- can be expressed in the terms of A_j^+ and A_j^-,

$$A_{j+1}^+ = \frac{1}{2}\left[\left(1+\beta_j\right)A_j^+ e^{ik_j l_j} + \left(1-\beta_j\right)A_j^- e^{-ik_j l_j}\right] \tag{5.21}$$

$$A_{j+1}^- = \frac{1}{2}\left[\left(1-\beta_j\right)A_j^+ e^{ik_j l_j} + \left(1+\beta_j\right)A_j^- e^{-ik_j l_j}\right] \tag{5.22}$$

where $\beta_j = S_j \rho_{j+1} c_{j+1} / S_{j+1} \rho_j c_j$.

A transfer matrix can be created based on equations 5.21 and 5.22,

$$\begin{bmatrix} A_{j+1}^+ \\ A_{j+1}^- \end{bmatrix} = \frac{1}{2}\begin{bmatrix} \left(1+\beta_j\right)e^{ik_j l_j} & \left(1-\beta_j\right)e^{-ik_j l_j} \\ \left(1-\beta_j\right)e^{ik_j l_j} & \left(1+\beta_j\right)e^{-ik_j l_j} \end{bmatrix}\begin{bmatrix} A_j^+ \\ A_j^- \end{bmatrix} \tag{5.23}$$

5.4.4 Transfer Matrix Considering the Flame

The effect of flame on the transfer matrix needs to be considered. Across the flame, the pressure and velocity difference can be derived from the energy and momentum equations,

$$p'(l_f^+) - p'(l_f^-) = 0 \tag{5.24}$$

$$u'(l_f^+) - u'(l_f^-) = \frac{\gamma - 1}{\gamma \bar{p}} \int \dot{q}' dx \tag{5.25}$$

where l_f^+ denotes the downstream side of the flame, l_f^- represents the upstream side of the flame, $\dot{q}'$ is the heat release rate oscillation per unit length, and $\bar{p}$ is the mean pressure.

The heat release rate can be expressed with an n-τ model [63],

$$\dot{q}' = \rho_u c_p (T_b - T_u) n u'(x, t-\tau)\delta(x - l_f) \tag{5.26}$$

where ρ_u is the density of the unburned gas, T_b is the temperature of the burned gas, T_u is the temperature of the unburned gas, and τ is the time delay between velocity and heat release rate oscillation. n is the gain of the heat release-velocity transfer function that is defined as,

$$n = \frac{\hat{q}/\bar{q}}{\hat{u}/\bar{u}} \tag{5.27}$$

where $\hat{q}$ is the amplitude of the heat release rate oscillation and $\bar{q}$ is the mean heat release rate.

Substitute equation to the integral in Equation 5.25, the velocity change can be expressed as,

$$\hat{u}_j(0) = \hat{u}_j(l_f)\left(1 + \left(\frac{T_b}{T_u} - 1\right) n e^{i\omega\tau}\right) \tag{5.28}$$

The pressure at the interface is,

$$\hat{p}_j(l_j) = \hat{p}_{j+1}(0) \tag{5.29}$$

By substituting equation 5.28 and 5.29 to equation 5.15 and 5.16,

$$A_j^+ e^{ik_j l_j} + A_j^- e^{-ik_j l_j} = A_{j+1}^+ + A_{j+1}^- \tag{5.30}$$

$$\frac{1}{\rho_j c_j}\left(1 + \left(\frac{T_b}{T_u} - 1\right) n e^{i\omega\tau}\right)\left(A_j^+ e^{ik_j l_j} - A_j^- e^{-ik_j l_j}\right) = \frac{1}{\rho_{j+1} c_{j+1}}\left(A_{j+1}^+ - A_{j+1}^-\right) \tag{5.31}$$

Then the transfer matrix can be defined as,

$$\begin{bmatrix} A_{j+1}^{+} \\ A_{j+1}^{-} \end{bmatrix} = \frac{1}{2}\begin{bmatrix} (1+\alpha_j)e^{ik_j l_j} & (1-\alpha_j)e^{-ik_j l_j} \\ (1-\alpha_j)e^{ik_j l_j} & (1+\alpha_j)e^{-ik_j l_j} \end{bmatrix}\begin{bmatrix} A_j^{+} \\ A_j^{-} \end{bmatrix} \tag{5.32}$$

where α_j is expressed as,

$$\alpha_j = \frac{\rho_{j+1}c_{j+1}}{\rho_j c_j}\left(1+\left(\frac{T_b}{T_u}-1\right)ne^{i\omega\tau}\right) \tag{5.33}$$

In the heat release rate model, n and τ are the two critical parameters that can determine the instability trend of a specific mode.

5.4.5 Boundary Conditions

Once all transfer matrices are obtained, the A^+ and A^- in the last section (N) can be related to the first section by,

$$\begin{bmatrix} A_N^{+} \\ A_N^{-} \end{bmatrix} = \left(\frac{1}{2}\right)^{N-1}\begin{bmatrix} (1+\beta_1)e^{ik_1 l_1} & (1-\beta_1)e^{-ik_1 l_1} \\ (1-\beta_1)e^{ik_1 l_1} & (1+\beta_1)e^{-ik_1 l_1} \end{bmatrix}[\ddots]\bullet\bullet\bullet\begin{bmatrix} A_1^{+} \\ A_1^{-} \end{bmatrix} \tag{5.34}$$

Then, a global transfer matrix can be expressed as,

$$\begin{bmatrix} A_N^{+} \\ A_N^{-} \end{bmatrix} = \begin{bmatrix} G_{11} & G_{12} \\ G_{21} & G_{22} \end{bmatrix}\begin{bmatrix} A_1^{+} \\ A_1^{-} \end{bmatrix} \tag{5.35}$$

Considering the boundary conditions at the inlet and outlet of the combustor,

$$\hat{p}_N(l_N) = A_N^{+}e^{il_N x_N} + A_N^{-}e^{-ik_N l_N} = 0 \tag{5.36}$$

$$\hat{u}_1(0) = \frac{1}{\rho_1 c_1}\left(A_1^{+} - A_1^{-}\right) = 0 \tag{5.37}$$

Then,

$$A_7^{+} / A_7^{-} = -e^{-2ik_N l_N} \tag{5.38}$$

$$A_1^{+} / A_1^{-} = -1 \tag{5.39}$$

Substitute into the global transfer matrix and find this,

$$G_{11}\frac{A_1^+}{A_1^-}+G_{12}-\frac{A_N^+}{A_N^-}\left(G_{21}\frac{A_1^+}{A_1^-}+G_{22}\right)=0 \tag{5.40}$$

The complex angular frequency can be found by solving equation 5.40. The system is unstable when the imaginary part is positive; otherwise, the system is stable.

5.4.6 Temperature Distribution

The temperature plays an important role in determining the acoustic properties of the system. For example, the temperature can significantly affect the speed of sound. In the current work, the 1D temperature distribution is computed in two steps. Firstly, the temperature at the location of the flame is calculated from a one-step chemical reaction. The heat loss is then determined from a heat transfer analysis to compute the temperature drop along the combustor axis.

The temperature at the location of the flame is determined by the heat release from the chemical reaction,

$$\begin{aligned} &n_f CH_4 + n_H H_2 + n_a(O_2 + 3.76N_2) = \\ &(2n_f + n_H)H_2O + n_f CO_2 + 3.76n_a N_2 + (n_a + 2n_f - \frac{n_H}{2})O_2 \end{aligned} \tag{5.41}$$

where n_f, n_H, and n_a are the mole number of CH_4, H_2, and O_2, respectively.

The temperature is determined by building the enthalpy balance between the reactions and products,

$$\sum n_P(\bar{h}_f^0 + \bar{h}_T - \bar{h}^0)_P = \sum n_R(\bar{h}_f^0 + \bar{h}_T - \bar{h}^0)_R \tag{5.42}$$

In the current study, the reference temperature is 298 K. The enthalpy values of $\bar{h}_f^0$ and $\bar{h}^0$ at 298 K are listed in Table 5.2 Enthalpy values.

Table 5.2 Enthalpy values

Gas	$\bar{h}_f^0$ (kJ/kmol)	$\bar{h}^0$ (kJ/kmol)
CH_4	-74850	--
H_2	0	--
O_2	0	--
N_2	0	8682
CO_2	-393520	8669
H_2O (gas)	-241820	9904

The term $\bar{h}_T$ is the enthalpy at a given temperature T. $\bar{h}_T$ can be expressed in terms of temperature linearly for different gases by using tables in [83]. For example, $\bar{h}_T$ of O2 can be written as,

$$(\bar{h}_T)_{O_2} = a_{h_{O_2}} + b_{h_{O_2}} T \tag{5.43}$$

The values for a_h and b_h for different gases are shown in Table 5.3.

Table 5.3. Coefficients for a_h and b_h in equation 5.43

gas	a_h	b_h
H_2O	-8430.9	44.63
CO_2	-13544	56.623
O_2	-4337.4	35.848
N_2	-3662.9	33.938

The curve fittings results are attached in Appendix B.

The calculated flame temperature for different hydrogen percentages is shown in Table 5.4.

Table 5.4. Calculated flame temperature

H_2 percentage	0%	10%	20%	30%	40%	50%
T (K)	1851.8	1857.7	1864.5	1872.7	1882.5	1894.6

The result of pure methane is compared with the simulation results considering complex reaction steps [84]. It is found the error is less than 1%, so the current results with simple reactions are considered as valid. Another thing can be noticed is that the temperature only varies in a limited range that is less than 50 K, which is believed to have a minor influence on the simulation; therefore, a mean temperature value of 1870.3 K is used for all cases.

The temperature in the chamber will decline due to the heat loss through the chamber wall. The heat loss is determined with a simple heat transfer network of heat resistance shown in Figure 5.14.

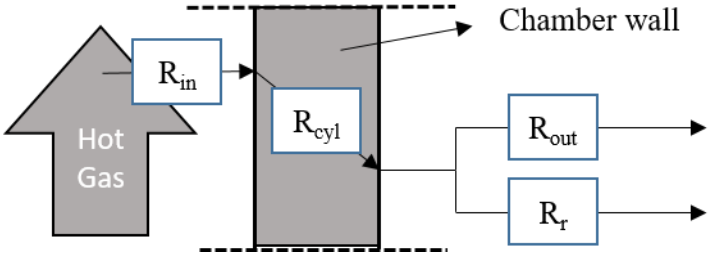

Figure 5.14. Heat transfer network.

The total heat resistance R_{total} can be expressed as,

$$R_{total} = R_{in} + R_{cyl} + 1/(1/R_{out} + 1/R_r) \quad (5.44)$$

where R_{in}, R_{cyl}, R_{out}, and R_r are the convection resistance inside the chamber, the conduction resistance through the wall, the convection resistance outside the chamber, and the radiation resistance outside the chamber, respectively.

The R_{in} is the convection resistance inside the chamber. Because the Reynolds number is less than 2300, the flow in the chamber is considered as laminar. As a result, Nu_{in} = 4.36 and the convection coefficient and convection resistance are expressed as,

$$h_{in} = \frac{Nu_{in} * K_{in}}{D_{c1}} \tag{5.45}$$

$$R_{in} = \frac{1}{2\pi r_{in} L h_{in}} \tag{5.46}$$

where K_{in} is the conductivity of the gas inside the chamber, D_{c1} is the inner diameter of the chamber, $r_{in} = D_{c1}/2$ is the inside radius, L is the length used for calculation and h_{in} is the convection coefficient of the inside of the wall.

The conduction resistance is calculated as,

$$R_{cyl} = \frac{ln(r_{in}/r_{out})}{2\pi L K_w} \tag{5.47}$$

where r_{out} is the outside radius, K_w is the conductivity of the chamber wall.

The convection coefficient and convection resistance of the outside wall are expressed as,

$$R_{out} = \frac{1}{2\pi r_{out} L h_{out}} \tag{5.48}$$

$$h_{out} = \frac{Nu_{out} * K_{out}}{D_{c2}} \tag{5.49}$$

where K_{out} is the conductivity of the gas outside the chamber, $D_{c2} = 2r_{out}$ is the outer diameter of the chamber, and h_{out} is the convection coefficient of the outside of the wall. The free convection outside the chamber can be calculated with empirical equations of Nusselt number and Rayleigh number (*Ra*),

$$Ra = \frac{g\beta(T_{out} - T_{\infty})}{\nu^2} Pr \tag{5.50}$$

$$Nu = \left\{ 0.825 + \frac{0.387 Ra^{\frac{1}{6}}}{\left[1 + \left(0.492 / Pr \right)^{9/16} \right]^{8/27}} \right\}^2 \tag{5.51}$$

where g is the gravity acceleration, β = 1/T, ν is the kinematic viscosity, T_{out} is the temperature of the outside wall, T_{∞} is the temperature of the surrounding environment, and Pr is the Prandtl number.

Table 5.5. Values of different variables

Variables	Value	Note
D_{c1} (m)	0.1016	
D_{c2} (m)	0.1143	
K_w (W/m·K)	1.4 for quartz tube 49.8 for steel	[85]
σ (W/m^2·K^4)	5.67 × 10^{-8}	
ε	0.93 for quartz tube 0.79 for steel	[85]
T_{∞} (K)	298	
g (m/s^2)	9.8	
ν (m^2/s)	5E-11T^2 + 9E-08T - 2E-05	Appendix B
c_p (W/kg·K)	-5E-05T^2 + 0.2756T + 914.26	Appendix B
K (W/m·K)	-1E-08T^2 + 7E-05T + 0.0057	Appendix B
ρ (kg/m^3)	352.79T^{-1}	Appendix B

The radiation resistance is determined as,

$$R_r = \frac{1}{2\pi r_{out} L h_r} \tag{5.52}$$

where the radiation heat transfer coefficient is defined as,

$$h_r = \varepsilon\sigma(T^2{}_{out} + T_\infty^2)(T_{out} + T_\infty) \tag{5.53}$$

where ε is the emissivity of the wall and σ is the *Stefan-Boltzmann* constant.

The values of all dimensions and material properties used in the current study are listed in Table 5.5.

5.4.7 Determination of *n* and τ

The delay time τ is determined by the method proposed in the work of Driscoll [60]. The equation is,

$$\tau = \frac{H_l}{S_T} \tag{5.54}$$

where H_l is the lift distance of the flame from the burner and S_T is the turbulent flame speed. In the current study, the H_l is modified as an effective lift distance, which is calculated as the averaged lift distance from different locations of the flame. The calculation of H_l is schematically shown in Figure 5.15.

The value of St is computed based on the equation suggested in Cheng's study that used a similar low swirl burner,

$$S_T = 1 + K_{H_2} \cdot \frac{u'_{RMS}}{S_L} \tag{5.55}$$

where K_{H_2} is the coefficient determined by the hydrogen percentage, u'_{RMS} is the axial root mean square (RMS) velocity that is estimated as 0.586 m/s based on reference [86],

and S_L is the laminar flame speed. S_L is computed with the empirical equation suggested by Sarli and Benedetto [87],

$$S_L = 0.38\varphi_F^{-0.35} exp[-5.5(\varphi_F - 1.1)^2] + 0.84R_H \tag{5.56}$$

$$\varphi_F = \frac{C_F / [C_A - C_H / (C_H / C_A)_{st}]}{(C_F / C_A)_{st}} \tag{5.57}$$

$$R_H = \frac{C_H + C_H / (C_H / C_A)_{st}}{C_F + [C_A - C_H / (C_H / C_A)_{st}]} \tag{5.58}$$

where C_A is the mole fraction of air, C_F is the mole fraction of methane, and C_H is the mole fraction of hydrogen. The subscript 'st' represents the stoichiometric condition.

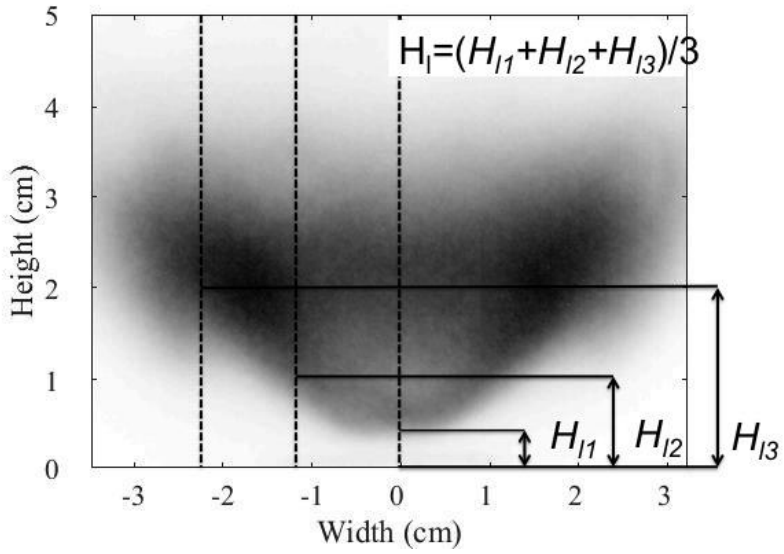

Figure 5.15. Definition of the effective lift distance.

The estimated values of S_L, S_T, H_l and are listed in Table 5.6 Results show that a higher η_H will subsequently result in a shorter delay time. Moreover, the effective distance only shows minor variations, which implies that the turbulent flame speed plays a critical role in determining the delay time.

There are still no effective methods to calculate n for the low-swirl burner. In the current study, the effect of n on the oscillation modes is examined at different delay times.

Table 5.6. Values of estimated properties of the flame

η_H (%)	S_L (m/s)	S_T (m/s)	H_l (m)	τ (s)
0	0.179	1.193	0.0075	0.0063
10	0.196	1.293	0.0077	0.0062
20	0.217	1.398	0.0076	0.0059
30	0.244	1.508	0.0076	0.0054
40	0.279	1.626	0.0073	0.00485

5.4.8 Simulation Results

First of all, the role of the flame gain (n) was examined. The simulation was carried out with the value of n changes from 0.1 to 1. Figure 5.16 shows the predicted modes with the largest growth rate of the cases at L_c = 300 mm and L_c = 1100 mm. We noticed that n does not have a significant effect on the mode determination when the value is larger than 0.4. Moreover, when n is less than 0.4, the oscillation modes found in the simulation are significantly different from the experiment results. A further examination shows that the solution didn't show notable differences once $n \geq 0.41$. Therefore, the current work chose n = 0.41 as the flame gain.

Figure 5.17 shows the detected modes of the case with different chamber lengths. It can be noticed that there is a group of low-frequency modes in the range of 140 – 200 Hz. Moreover, a group of high-frequency modes is found with a value large than 370 Hz.

For low-frequency modes, the modeling results consistent with the experimental data. However, the performance of the simulation in the high-frequency range is not accurate. It is believed that the high-frequency modes are also the natural mode of the combustor, but they won't be triggered when the delay time is long (or when η_H is small). A consideration of the acoustic damping and detailed flame dynamics could be useful in eliminating the ′unrealistic′ oscillation modes.

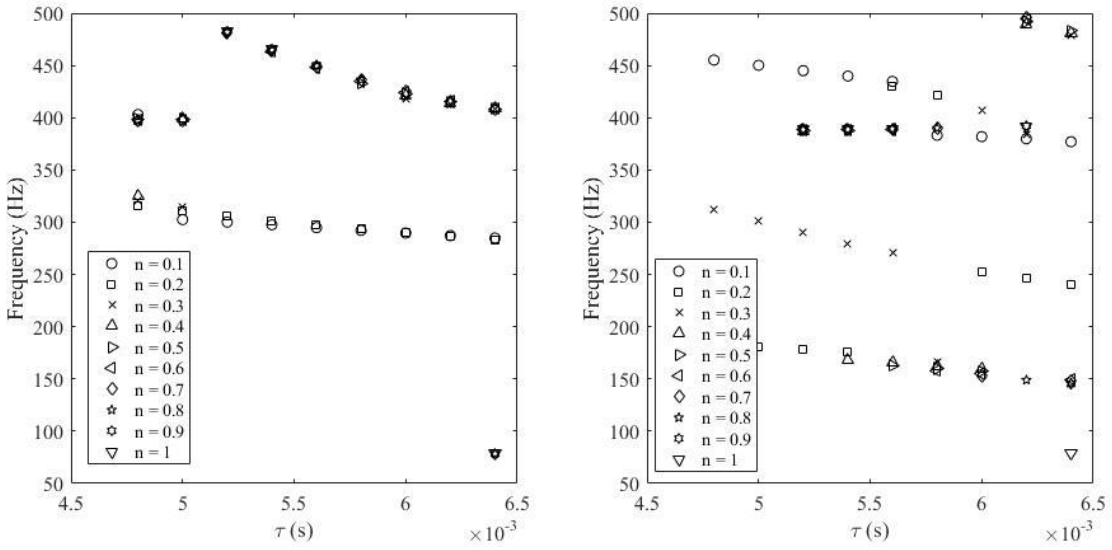

Figure 5.16. Detected oscillation modes with different values of n, L_c = 300 mm (left), L_c = 1100 mm (right).

A more detailed comparison between simulation and experiment results in the low-frequency range are shown in Figure 5.17. Although the absolute values still show some difference, the general trend is captured by the simulation results. It can be noticed that the oscillation frequency decreases with the increasing delay time in all cases. In the current study, the turbulent flame speed is the critical parameter that affects the delay time. Therefore, we believe the turbulent flame speed the key parameter that determines the instability trend in the current study.

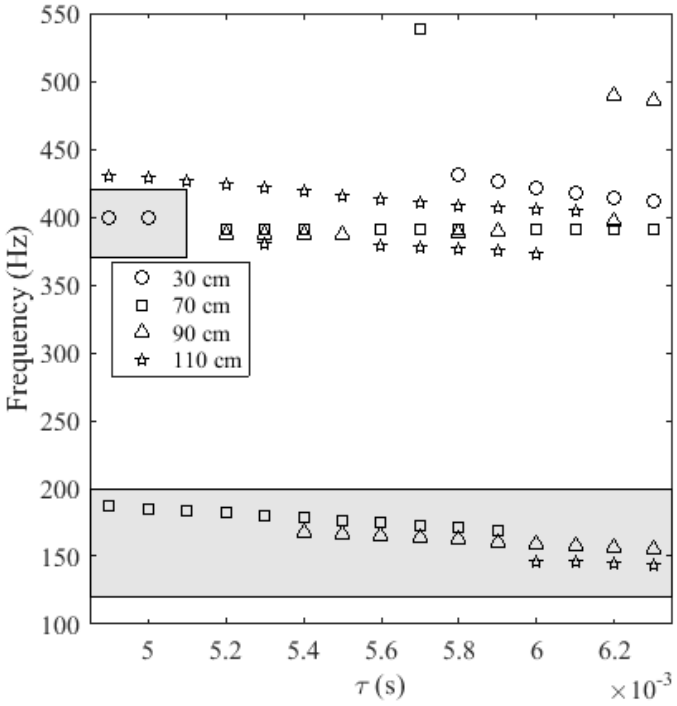

Figure 5.17. Predicted oscillation modes of cases with different chamber lengths (the gray area represents the oscillation range detected with experiment).

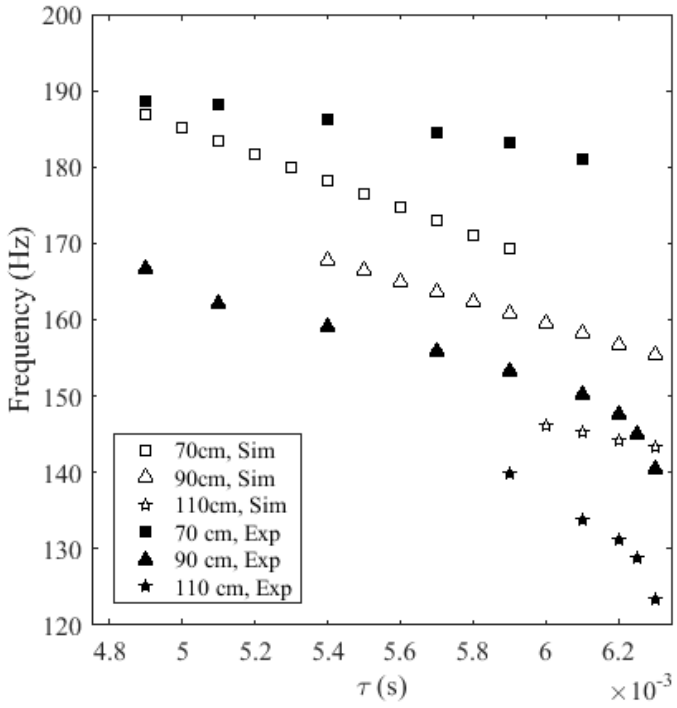

Figure 5.18. Comparison between simulation and experiment results.

5.4.9 Discussion

The 1D model is useful to predict the potential oscillation modes of the combustor. However, it still cannot accurately estimate the unstable modes because of the lack of a reliable heat release mode.

As demonstrated in the simulation results, the value of flame gain (n) is still dependent on the empirical value, which is hard to be related to the physical features of the flame. Furthermore, the current heat release mode cannot reveal the relationship between the delay time (τ) and the phase delay between heat release and pressure oscillations.

The major problem of the current heat release model is the lack of consideration of the flame structure. Results of acoustic-induced and self-excited instability have demonstrated that the flame shape deformation plays a critical role in determining the global instability trend. Therefore, a heat release model considering the flame structure is needed for characterizing the flame-acoustic interaction.

5.5 Conclusions

The current study shows the effect of hydrogen addition on the flame shape and the frequency and amplitude of pressure oscillation. OH* chemiluminescence images show that an increase in hydrogen percentage can result in a more condensed flame. Furthermore, a power spectral density analysis shows that hydrogen concentration is critical in determining the instability trend. Low frequency modes (120 – 200 Hz) are mainly triggered when the hydrogen concentration is low, whereas high frequency oscillations (~ 400 Hz) tend to occur in cases with a high hydrogen percentage (> 40%).

Results also demonstrate that both the oscillation amplitude and frequency are affected by hydrogen addition. In the low frequency range, the oscillation frequency tends to increase with an increasing hydrogen percentage. However, the effect of hydrogen addition to the oscillation amplitude is not monotonic. A Rayleigh index analysis shows that the current oscillation is still triggered by longitudinal modes. It also demonstrates that a larger positive Rayleigh index tends to result in a stronger pressure oscillation.

The modeling work based on the 1D acoustic model was conducted to predict the unstable modes of the combustor. In the 1D model, an n-τ model was utilized to represent the heat release oscillation. Results show that the model can reasonably predict the oscillation modes in the low-frequency range, whereas the high frequency oscillation range is over predicted. Moreover, it was found that the delay time, which is majorly affected by S_T, plays a critical role in determining the changing trend of the oscillation frequency.

CHAPTER 6
SUMMARY AND FUTURE WORK

6.1 Summary

The current work examined flame behaviors with acoustic perturbation and self-excited thermoacoustic instability. The aim of the work is trying to relate the global flame features with the local flame behaviors. Moreover, the current work tried to use flame-dependent, rather than burner-dependent, parameters to predict the instability trend.

The acoustic chamber, diagnostic system, and the method for calculating FSD were introduced through Chapter 1. Chapter 1 examined the effects of the elevated pressure on the flame response to acoustic perturbations. This chapter firstly introduced the idea of analyzing the global of local heat release oscillation together. Results showed that when the heat release oscillation was approximately in phase with the pressure fluctuation, the elevated pressure tended to amplify the fundamental oscillation. On the other hand, the elevated pressure tended to inhibit the fundamental oscillation when the heat release oscillation was approximately out-of-phase with the acoustic perturbation. Analysis of flame dynamics and local flame structures demonstrated that the phase difference among different cases was caused by the delay in the different types of flame rollup. Moreover, the OH-PLIF images showed that the influence of the pressure on flame propagation was strongly phase-dependent. Besides the global analysis, the local analysis revealed the amplitude and phase distribution of the local heat release oscillation. The local analysis implied that the effect of the pressure on the distribution was the main way through which the pressure affected the global heat release oscillation.

Chapter 2 introduced the Rayleigh criterion and a POD method to examine the local thermoacoustic features. Rayleigh criterion analysis illustrated that the perturbation strength could significantly change the intensity and shape of local flame-acoustic coupling, which showed a notable spatial variation. To investigate the effect of flame deformation on the local flame response, a POD method was proposed to decompose the phase-averaged FSD into fundamental and harmonic oscillation. The local analysis demonstrated that the fundamental oscillation dominated the flame response, whereas the harmonic oscillation affected the flame response by sharing oscillation energy. We believed that The POD-based local analysis is not limited to the LSB but is applicable in other cases whenever the sinusoidal pressure oscillation information can be identified. Consequently, the current method can be useful in capturing accurate spatial information for heat release oscillations in flames.

Chapter 3 examined the global and local flame responses to acoustic perturbations with cases at different Strouhal numbers. Both local and global analyses illustrated that the Strouhal number was useful in characterizing the changing trend of the oscillation amplitude. Flame dynamics analysis demonstrated that the flame shape deformation was strongly dependent on Strouhal numbers when the perturbation level was high. The intense flame roll-up is believed to be the main reason cause flame shape deformation in current cases.

Chapter 3 also showed that large-scale flame deformations could result in intense local fundamental oscillations. However, the contribution of the local oscillation to the global fluctuation was affected by the phase distribution that was characterized by the Strouhal number. The local oscillations tended to cancel each other if they are out-of-

phase and have a comparable strength, which subsequently resulted in a low-amplitude global oscillation; otherwise, the amplitude of the global oscillation was relatively high. Furthermore, Chapter 3 demonstrated that the intensity of local harmonic oscillations also associated with the scale of flame deformation. Generally, the global strength of the fundamental modes is much weaker than that of the fundamental oscillation. Only when the perturbation level is sufficiently high, the first harmonic mode could have a comparable level with that of the fundamental oscillation if the local fundamental oscillations tend to cancel each other out. The result implies that the energy leakage to the harmonic mode is less likely the main reason causes the weakened fundamental mode.

Besides the acoustic perturbation study, Chapter 5 talked about the experimental and modeling work on self-excited thermoacoustic instability. Hydrogen was blended with methane to examine how the change in fuel properties affected the instability trend. The study examined the effect of hydrogen addition on the flame shape and the frequency and amplitude of pressure oscillation. Results showed that a more condensed flame would result with a higher hydrogen concentration. Moreover, it was found that Low frequency modes (120 – 200 Hz) were excited when the hydrogen concentration was low, whereas high frequency oscillations (~ 400 Hz) tended to occur in cases with a high hydrogen percentage (> 40%). Results also demonstrated that both the oscillation amplitude and frequency are affected by the hydrogen addition. A Rayleigh index analysis shows that the current oscillation is still triggered by longitudinal modes.

Another important part of Chapter 5 is the modeling work based on the 1D acoustic model. In the 1D model, the heat release oscillation was represented with an n-τ model. Results found that the delay time, which is majorly affected by S_T, plays a critical

role in determining the changing trend of the oscillation frequency. Results also showed that the model was limited in predicting the high frequency mode detected in the experiment. It implies that the acoustic damping and detailed flame dynamics need to be considered.

6.2 Future Work

The previous work revealed that the local information and flame dynamics are the key factors that play critical roles in determining the instability trend. Moreover, the turbulent flame speed is the key parameter that affects the changing trend of the self-excited thermoacoustic instability. I would recommend several topics that could be used to understand the mechanism of thermoacoustic instability further.

1. A combined velocity field and local flame structure examination. It would used to quantify the dependence of flame oscillation on the larger coherence structures in the flow field.

2. More detailed study on the effect of the ambient pressure on the flame oscillation trend. The particular focus can be on the flame wrinkling that shows a strong dependence on the oscillation phase. If possible, the velocity measurement is highly recommended.

3. Flame dynamics modeling with the consideration on flame structures. The current modeling work showed that the modeling couldn't accurately predict all oscillation modes because of the lack of the knowledge of flame structure.

REFERENCES

[1] Lieuwen, T. C., and Yang, V. *Combustion instabilities in gas turbine engines : operational experience, fundamental mechanisms and modeling*. Reston, VA: American Institute of Aeronautics and Astronautics, 2005.

[2] Zhang, J., and Ratner, A. "Effect of pressure variation on acoustically perturbed swirling flames," *Proceedings of the Combustion Institute* Vol. 36, No. 3, 2017, pp. 3881-3888.

[3] Zhang, J., and Ratner, A. "Experimental Study of the Global and Local Flame Responses to Acoustic Perturbation," *Journal of Propulsion and Power*, 2016.

[4] Rayleigh, J. "The explanation of certain acoustical phenomena," *Nature* Vol. 18, No. 455, 1878, pp. 319-321.

[5] Culick, F. E. C. "A Note on Rayleigh's Criterion," *Combustion Science and Technology* Vol. 56, 1987, pp. 159-166.

[6] Tachibana, S., Kanai, K., Yoshida, S., Suzuki, K., and Sato, T. "Combined effect of spatial and temporal variations of equivalence ratio on combustion instability in a low-swirl combustor," *Proceedings of the Combustion Institute* Vol. 35, No. 3, 2015, pp. 3299-3308.

[7] Poinsot, T. J., Trouve, A. C., Veynante, D. P., Candel, S. M., and Esposito, E. J. "Vortex-Driven Acoustically Coupled Combustion Instabilities," *Journal of Fluid Mechanics* Vol. 177, 1987, pp. 265-292.

[8] Hathout, J. P., Fleifil, M., Annaswamy, A. M., and Ghoniem, A. F. "Combustion instability active control using periodic fuel injection," *Journal of Propulsion and Power* Vol. 18, No. 2, 2002, pp. 390-399.

[9] Mcmanus, K. R., Vandsburger, U., and Bowman, C. T. "Combustor Performance Enhancement through Direct Shear-Layer Excitation," *Combustion and Flame* Vol. 82, No. 1, 1990, pp. 75-92.

[10] Coats, C. M. "Coherent structures in combustion," *Progress in Energy and Combustion Science* Vol. 22, No. 5, 1996, pp. 427-509.

[11] Smith, D. A., and Zukoski, E. E. "Combustion instability sustained by unsteady vortex combustion," *AIAA/SAE/ASME/ASEE 21st Joint Propulsion Conference*. California, 1985.

[12] Candel, S. M. "Combustion instabilities coupled by pressure waves and their active control," *Symposium (International) on Combustion* Vol. 24, No. 1, 1992, pp. 1277-1296.

[13] Schadow, K. C., and Gutmark, E. "Combustion Instability Related to Vortex Shedding in Dump Combustors and Their Passive Control," *Progress in Energy and Combustion Science* Vol. 18, No. 2, 1992, pp. 117-132.

[14] Rogers, D. E., and Marble, F. E. "A Mechanism for High-Frequency Oscillation in Ramjet Combustors and Afterburners," *Jet Propulsion* Vol. 26, No. 6, 1956, pp. 456-464.

[15] Shanbhogue, S., Shin, D.-H., Hemchandra, S., Plaks, D., and Lieuwen, T. "Flame-sheet dynamics of bluff-body stabilized flames during longitudinal acoustic forcing," *Proceedings of the Combustion Institute* Vol. 32, No. 2, 2009, pp. 1787-1794.

[16] Balachandran, R., Ayoola, B. O., Kaminski, C. F., Dowling, A. P., and Mastorakos, E. "Experimental investigation of the nonlinear response of turbulent premixed flames to imposed inlet velocity oscillations," *Combustion and Flame* Vol. 143, No. 1-2, 2005, pp. 37-55.

[17] Armitage, C., Balachandran, R., Mastorakos, E., and Cant, R. "Investigation of the nonlinear response of turbulent premixed flames to imposed inlet velocity oscillations," *Combustion and Flame* Vol. 146, No. 3, 2006, pp. 419-436.

[18] Liang, H. Z., and Maxworthy, T. "An experimental investigation of swirling jets," *Journal of Fluid Mechanics* Vol. 525, 2005, pp. 115-159.

[19] Gallaire, F., and Chomaz, J. M. "Mode selection in swirling jet experiments: a linear stability analysis," *Journal of Fluid Mechanics* Vol. 494, 2003, pp. 223-253.

[20] Ballachey, G. E., and Johnson, M. R. "Prediction of blowoff in a fully controllable low-swirl burner burning alternative fuels: Effects of burner geometry, swirl, and fuel composition," *Proceedings of the Combustion Institute* Vol. 34, 2013, pp. 3193-3201.

[21] Huang, Y., Wang, S. W., and Yang, V. "Systematic analysis of lean-premixed swirl-stabilized combustion," *AIAA Journal* Vol. 44, No. 4, 2006, pp. 724-740.

[22] Stone, C., and Menon, S. "Swirl control of combustion instabilities in a gas turbine combustor," *Proceedings of the Combustion Institute* Vol. 29, No. 1, 2002, pp. 155-160.

[23] Davis, D. W., Therkelsen, P. L., Littlejohn, D., and Cheng, R. K. "Effects of hydrogen on the thermo-acoustics coupling mechanisms of low-swirl injector flames in a model gas turbine combustor," *Proceedings of the Combustion Institute* Vol. 34, No. 2, 2013, pp. 3135-3143.

[24] Markovich, D. M., Abdurakipov, S. S., Chikishev, L. M., Dulin, V. M., and Hanjalic, K. "Comparative analysis of low- and high-swirl confined flames and jets by proper orthogonal and dynamic mode decompositions," *Physics of Fluids* Vol. 26, No. 6, 2014.

[25] Kang, D. M., Culick, F. E. C., and Ratner, A. "Combustion dynamics of a low-swirl combustor," *Combustion and Flame* Vol. 151, No. 3, 2007, pp. 412-425.

[26] Moeck, J. P., Bourgouin, J.-F., Durox, D., Schuller, T., and Candel, S. "Tomographic reconstruction of heat release rate perturbations induced by helical modes in turbulent swirl flames," *Experiments in fluids* Vol. 54, No. 4, 2013, pp. 1-17.

[27] Moeck, J. P., Bourgouin, J. F., Durox, D., Schuller, T., and Candel, S. "Nonlinear interaction between a precessing vortex core and acoustic oscillations in a turbulent swirling flame," *Combustion and Flame* Vol. 159, No. 8, 2012, pp. 2650-2668.

[28] Huang, Y., Sung, H. G., Hsieh, S. Y., and Yang, V. "Large-eddy simulation of combustion dynamics of lean-premixed swirl-stabilized combustor," *Journal of Propulsion and Power* Vol. 19, No. 5, 2003, pp. 782-794.

[29] Steinberg, A. M., Arndt, C. M., and Meier, W. "Parametric study of vortex structures and their dynamics in swirl-stabilized combustion," *Proceedings of the Combustion Institute* Vol. 34, 2013, pp. 3117-3125.

[30] O'Connor, J., and Lieuwen, T. "Disturbance Field Characteristics of a Transversely Excited Burner," *Combustion Science and Technology* Vol. 183, No. 5, 2011, pp. 427-443.

[31] Huang, Y., and Ratner, A. "Experimental Investigation of Thermoacoustic Coupling for Low-Swirl Lean Premixed Flames," *Journal of Propulsion and Power* Vol. 25, No. 2, 2009, pp. 365-373.

[32] Kim, K. T., and Hochgreb, S. "The nonlinear heat release response of stratified lean-premixed flames to acoustic velocity oscillations," *Combustion and Flame* Vol. 158, No. 12, 2011, pp. 2482-2499.

[33] Paschereit, C. O., Gutmark, E., and Weisenstein, W. "Excitation of thermoacoustic instabilities by interaction of acoustics and unstable swirling flow," *Aiaa Journal* Vol. 38, No. 6, 2000, pp. 1025-1034.

[34] Therkelsen, P. L., Littlejohn, D., Cheng, R. K., Portillo, J. E., and Martin, S. M. "Effect of Combustor Inlet Geometry on Acoustic Signature and Flow Field Behavior of the Low Swirl Injector," *ASME Turbo Expo 2010: Power for Land, Sea, and Air*. American Society of Mechanical Engineers, 2010, pp. 1183-1194.

[35] Paschereit, C. O., Flohr, P., and Gutmark, E. J. "Combustion control by vortex breakdown stabilization," *Journal of Turbomachinery-Transactions of the Asme* Vol. 128, No. 4, 2006, pp. 679-688.

[36] Kobayashi, H., Nakashima, T., Tamura, T., Maruta, K., and Niioka, T. "Turbulence measurements and observations of turbulent premixed flames at elevated pressures up to 3.0 MPa," *Combustion and Flame* Vol. 108, No. 1–2, 1997, pp. 104-117.

[37] Kobayashi, H., Tamura, T., Maruta, K., Niioka, T., and Williams, F. A. "Burning velocity of turbulent premixed flames in a high-pressure environment," *Symposium (International) on Combustion* Vol. 26, No. 1, 1996, pp. 389-396.

[38] Boxx, I., Slabaugh, C., Kutne, P., Lucht, R. P., and Meier, W. "3 kHz PIV/OH-PLIF measurements in a gas turbine combustor at elevated pressure," *Proceedings of the Combustion Institute* Vol. 35, No. 3, 2015, pp. 3793-3802.

[39] Bunce, N., Lee, J. G., Quay, B. D., and Santavicca, D. A. "Mixture-forced flame transfer function measurements and mechanisms in a single-nozzle combustor at elevated pressure," *ASME 2011 Turbo Expo: Turbine Technical Conference and Exposition*. American Society of Mechanical Engineers, 2011, pp. 1317-1326.

[40] Cheung, W., Sims, G., Copplestone, R., Tilston, J., Wilson, C., Stow, S. R., and Dowling, A. P. "Measurement and analysis of flame transfer function in a sector combustor under high

pressure conditions," *ASME Turbo Expo 2003, collocated with the 2003 International Joint Power Generation Conference*. American Society of Mechanical Engineers, 2003, pp. 187-194.

[41] Huang, Y. "Combustion dynamics of swirl-stabilized lean premixed flames in an acoustically-driven environment," 2008.

[42] Lee, J. G., and Santavicca, D. A. "Experimental diagnostics for the study of combustion instabilities in lean premixed combustors," *Journal of Propulsion and Power* Vol. 19, No. 5, 2003, pp. 735-750.

[43] Lee, S. Y., Seo, S., Broda, J. C., Pal, S., and Santoro, R. J. "An experimental estimation of mean reaction rate and flame structure during combustion instability in a lean premixed gas turbine combustor," *Proceedings of the Combustion Institute* Vol. 28, 2000, pp. 775-782.

[44] Najm, H. N., Paul, P. H., Mueller, C. J., and Wyckoff, P. S. "On the Adequacy of Certain Experimental Observables as Measurements of Flame Burning Rate," *Combustion and Flame* Vol. 113, No. 3, 1998, pp. 312-332.

[45] Palies, P., Durox, D., Schuller, T., and Candel, S. "The combined dynamics of swirler and turbulent premixed swirling flames," *Combustion and Flame* Vol. 157, No. 9, 2010, pp. 1698-1717.

[46] Yoon, J., Kim, M.-K., Hwang, J., Lee, J., and Yoon, Y. "Effect of fuel–air mixture velocity on combustion instability of a model gas turbine combustor," *Applied Thermal Engineering* Vol. 54, No. 1, 2013, pp. 92-101.

[47] Ayoola, B. O., Balachandran, R., Frank, J. H., Mastorakos, E., and Kaminski, C. F. "Spatially resolved heat release rate measurements in turbulent premixed flames," *Combustion and Flame* Vol. 144, No. 1-2, 2006, pp. 1-16.

[48] Schimek, S., Moeck, J. P., and Paschereit, C. O. "An experimental investigation of the nonlinear response of an atmospheric swirl-stabilized premixed flame," *Journal of Engineering for Gas Turbines and Power* Vol. 133, No. 10, 2011, p. 101502.

[49] Hanson, R. K., Seitzman, J. M., and Paul, P. H. "Planar Laser-Fluorescence Imaging of Combustion Gases," *Applied Physics B-Photophysics and Laser Chemistry* Vol. 50, No. 6, 1990, pp. 441-454.

[50] Boxx, I., Stöhr, M., Carter, C., and Meier, W. "Temporally resolved planar measurements of transient phenomena in a partially pre-mixed swirl flame in a gas turbine model combustor," *Combustion and Flame* Vol. 157, No. 8, 2010, pp. 1510-1525.

[51] Nguyen, Q. V., and Paul, P. H. "The time evolution of a vortex-flame interaction observed via planar imaging of CH and OH," *Twenty-Sixth Symposium (International) on Combustion* Vol. 26, No. 1, 1996, pp. 357-364.

[52] Frank, J. H., Kalt, P. A. M., and Bilger, R. W. "Measurements of conditional velocities in turbulent premixed flames by simultaneous OH PLIF and PIV," *Combustion and Flame* Vol. 116, No. 1–2, 1999, pp. 220-232.

[53] Lee, G. G., Huh, K. Y., and Kobayashi, H. "Measurement and analysis of flame surface density for turbulent premixed combustion on a nozzle-type burner," *Combustion and Flame* Vol. 122, No. 1–2, 2000, pp. 43-57.

[54] Shepherd, I. G., and Cheng, R. K. "The burning rate of premixed flames in moderate and intense turbulence," *Combustion and Flame* Vol. 127, No. 3, 2001, pp. 2066-2075.

[55] Allison, P. M., Chen, Y., Ihme, M., and Driscoll, J. F. "Coupling of flame geometry and combustion instabilities based on kilohertz formaldehyde PLIF measurements," *Proceedings of the Combustion Institute* Vol. 35, No. 3, 2015, pp. 3255-3262.

[56] Steinberg, A. M., Boxx, I., Stöhr, M., Carter, C. D., and Meier, W. "Flow–flame interactions causing acoustically coupled heat release fluctuations in a thermo-acoustically unstable gas turbine model combustor," *Combustion and Flame* Vol. 157, No. 12, 2010, pp. 2250-2266.

[57] Caux-Brisebois, V., Steinberg, A. M., Arndt, C. M., and Meier, W. "Thermo-acoustic velocity coupling in a swirl stabilized gas turbine model combustor," *Combustion and Flame* Vol. 161, No. 12, 2014, pp. 3166-3180.

[58] Worth, N. A., and Dawson, J. R. "Cinematographic OH-PLIF measurements of two interacting turbulent premixed flames with and without acoustic forcing," *Combustion and Flame* Vol. 159, No. 3, 2012, pp. 1109-1126.

[59] Ma, L., Wu, Y., Lei, Q., Xu, W., and Carter, C. D. "3D flame topography and curvature measurements at 5 kHz on a premixed turbulent Bunsen flame," *Combustion and Flame* Vol. 166, 2016, pp. 66-75.

[60] Chen, Y., and Driscoll, J. F. "A multi-chamber model of combustion instabilities and its assessment using kilohertz laser diagnostics in a gas turbine model combustor," *Combustion and Flame* Vol. 174, 2016, pp. 120-137.

[61] Temme, J. E., Allison, P. M., and Driscoll, J. F. "Combustion instability of a lean premixed prevaporized gas turbine combustor studied using phase-averaged PIV," *Combustion and Flame* Vol. 161, No. 4, 2014, pp. 958-970.

[62] Schuller, T., Durox, D., Palies, P., and Candel, S. "Acoustic decoupling of longitudinal modes in generic combustion systems," *Combustion and Flame* Vol. 159, No. 5, 2012, pp. 1921-1931.

[63] Hong, S., Shanbhogue, S. J., Speth, R. L., and Ghoniem, A. F. "On the phase between pressure and heat release fluctuations for propane/hydrogen flames and its role in mode transitions," *Combustion and Flame* Vol. 160, No. 12, 2013, pp. 2827-2842.

[64] Dowling, A. P., and Stow, S. R. "Acoustic analysis of gas turbine combustors," *Journal of Propulsion and Power* Vol. 19, No. 5, 2003, pp. 751-764.

[65] Schuller, T., Durox, D., and Candel, S. "A unified model for the prediction of laminar flame transfer functions," *Combustion and Flame* Vol. 134, No. 1, 2003, pp. 21-34.

[66] Preetham, R., Santosh, H., and Lieuwen, T. "Dynamics of Laminar Premixed Flames Forced by Harmonic Velocity Disturbances," *Journal of Propulsion and Power* Vol. 24, No. 6, 2008, pp. 1390-1402.

[67] Fleifil, M., Annaswamy, A. M., Ghoneim, Z. A., and Ghoniem, A. F. "Response of a laminar premixed flame to flow oscillations: A kinematic model and thermoacoustic instability results," *Combustion and Flame* Vol. 106, No. 4, 1996, pp. 487-510.

[68] Dowling, A. P. "A kinematic model of a ducted flame," *Journal of Fluid Mechanics* Vol. 394, 1999, pp. 51-72.

[69] Kerstein, A. R., Ashurst, W. T., and Williams, F. A. "Field equation for interface propagation in an unsteady homogeneous flow field," *Physical Review A* Vol. 37, No. 7, 1988, pp. 2728-2731.

[70] Hemchandra, S., Peters, N., and Lieuwen, T. "Heat release response of acoustically forced turbulent premixed flames—role of kinematic restoration," *Proceedings of the Combustion Institute* Vol. 33, No. 1, 2011, pp. 1609-1617.

[71] Fairweather, M., Ormsby, M. P., Sheppard, C. G. W., and Woolley, R. "Turbulent burning rates of methane and methane-hydrogen mixtures," *Combustion and Flame* Vol. 156, No. 4, 2009, pp. 780-790.

[72] Littlejohn, D., and Cheng, R. K. "Fuel effects on a low-swirl injector for lean premixed gas turbines," *Proceedings of the Combustion Institute* Vol. 31, 2007, pp. 3155-3162.

[73] Cheng, R. K., Littlejohn, D., Nazeer, W. A., and Smith, K. O. "Laboratory studies of the flow field characteristics of low-swirl injectors for adaptation to fuel-flexible turbines," *Journal of Engineering for Gas Turbines and Power-Transactions of the Asme* Vol. 130, No. 2, 2008, p. 021501.

[74] Kang, D. M. "Measurements of combustion dynamics with laser-based diagnostic techniques," *Engineering and Applied Science*. California Institute of Technology, California, 2006.

[75] Lachaux, T., Halter, F., Chauveau, C., Gökalp, I., and Shepherd, I. G. "Flame front analysis of high-pressure turbulent lean premixed methane–air flames," *Proceedings of the Combustion Institute* Vol. 30, No. 1, 2005, pp. 819-826.

[76] Holmes, P. *Turbulence, coherent structures, dynamical systems and symmetry*. New York: Cambridge University Press, 2012.

[77] Sirovich, L. "Turbulence and the dynamics of coherent structures. Part I: Coherent structures," *Quarterly of applied mathematics* Vol. 45, No. 3, 1987, pp. 561-571.

[78] Freymuth, P. "On Transition in a Separated Laminar Boundary Layer," *Journal of Fluid Mechanics* Vol. 25, 1966, pp. 683-&.

[79] Stohr, M., Sadanandan, R., and Meier, W. "Phase-resolved characterization of vortex-flame interaction in a turbulent swirl flame," *Experiments in Fluids* Vol. 51, No. 4, 2011, pp. 1153-1167.

[80] Oberleithner, K., Sieber, M., Nayeri, C. N., Paschereit, C. O., Petz, C., Hege, H. C., Noack, B. R., and Wygnanski, I. "Three-dimensional coherent structures in a swirling jet undergoing vortex breakdown: stability analysis and empirical mode construction," *Journal of Fluid Mechanics* Vol. 679, 2011, pp. 383-414.

[81] Cundy, H. M., and Rollett, A. P. *Mathematical models*: Oxford, 1961.

[82] Cheng, R. K., Littlejohn, D., Strakey, P. A., and Sidwell, T. "Laboratory investigations of a low-swirl injector with H2 and CH4 at gas turbine conditions," *Proceedings of the Combustion Institute* Vol. 32, No. 2, 2009, pp. 3001-3009.

[83] Moran, M. J. "Engineering thermodynamics," *The CRC Handbook of Mechanical Engineering, Second Edition*. CRC Press, 2004.

[84] Abdellatif, B., Mohammed, A., El Houssine, A., and El Houssine, C. "CH 4/NO x Reduced Mechanisms Used for Modeling Premixed Combustion," *Energy and Power Engineering* Vol. 2012, 2012.

[85] Cengel, Y. A., and Ghajar, A. "Heat and mass transfer (a practical approach, SI version)." McGraw-Hill Education, 2011.

[86] Cheng, R., and Littlejohn, D. "Effects of combustor geometry on the flowfields and flame properties of a low-swirl injector," *ASME Turbo Expo 2008: Power for Land, Sea, and Air*. American Society of Mechanical Engineers, 2008, pp. 393-407.

[87] Di Sarli, V., and Di Benedetto, A. "Laminar burning velocity of hydrogen–methane/air premixed flames," *International Journal of Hydrogen Energy* Vol. 32, No. 5, 2007, pp. 637-646.

APPENDIX A

The Appendix A demonstrates the mean and phase-averaged OH* chemiluminescence images.

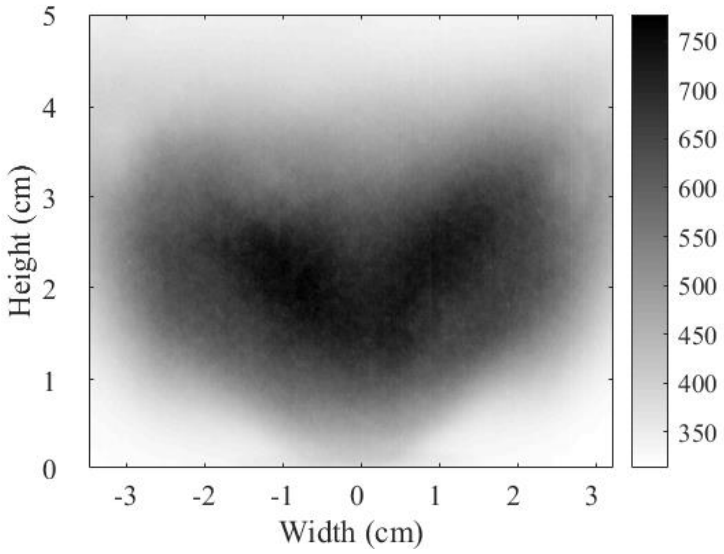

Figure A. 1. Mean OH* of the case with L_c = 1100mm and η_H = 0%.

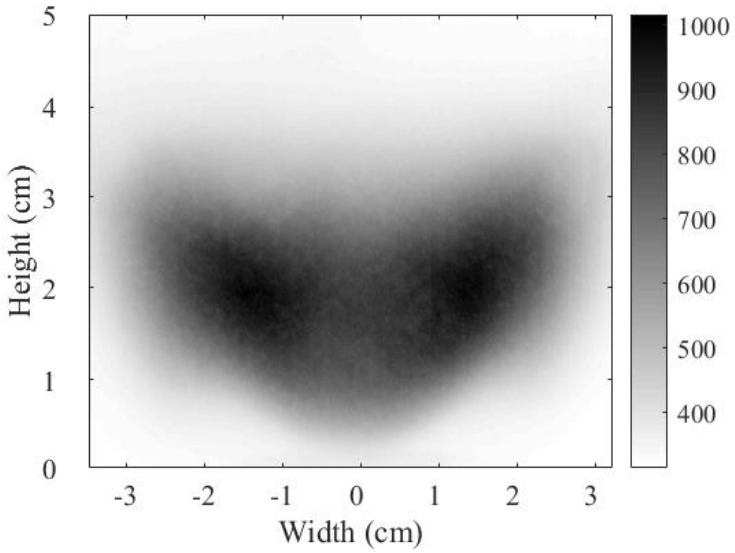

Figure A. 2. Mean OH* of the case with L_c = 1100mm and η_H = 15%.

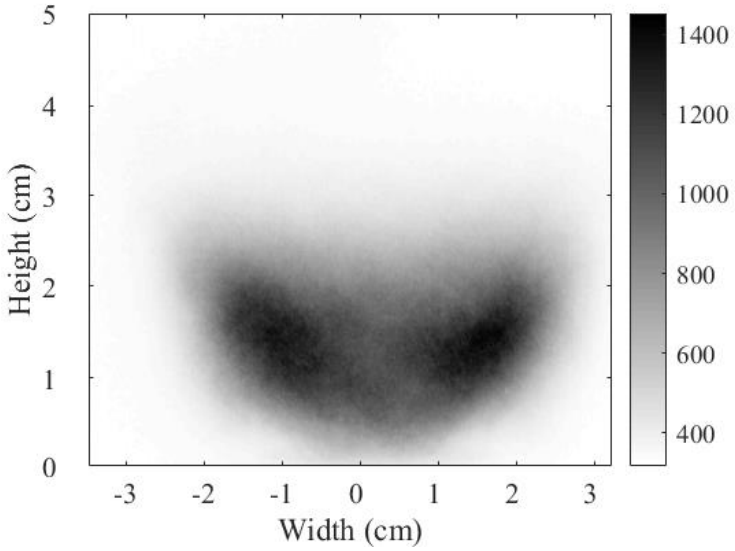

Figure A. 3. Mean OH* of the case with L_c = 1100mm and η_H = 50%.

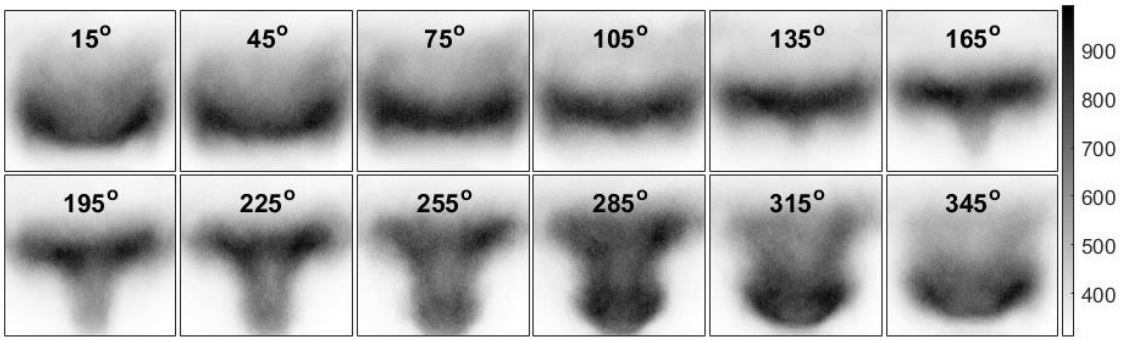

Figure A. 4. Phase-averaged OH* of the case with L_c = 1100mm and η_H = 0%.

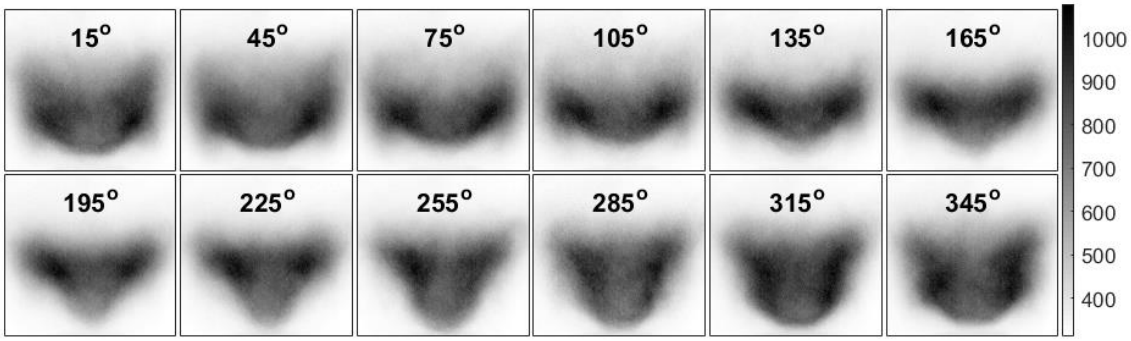

Figure A. 5. Phase-averaged OH* of the case with L_c = 1100mm and η_H = 15%.

APPENDIX B

The Appendix B shows the curve fitting results of the properties of different gases.

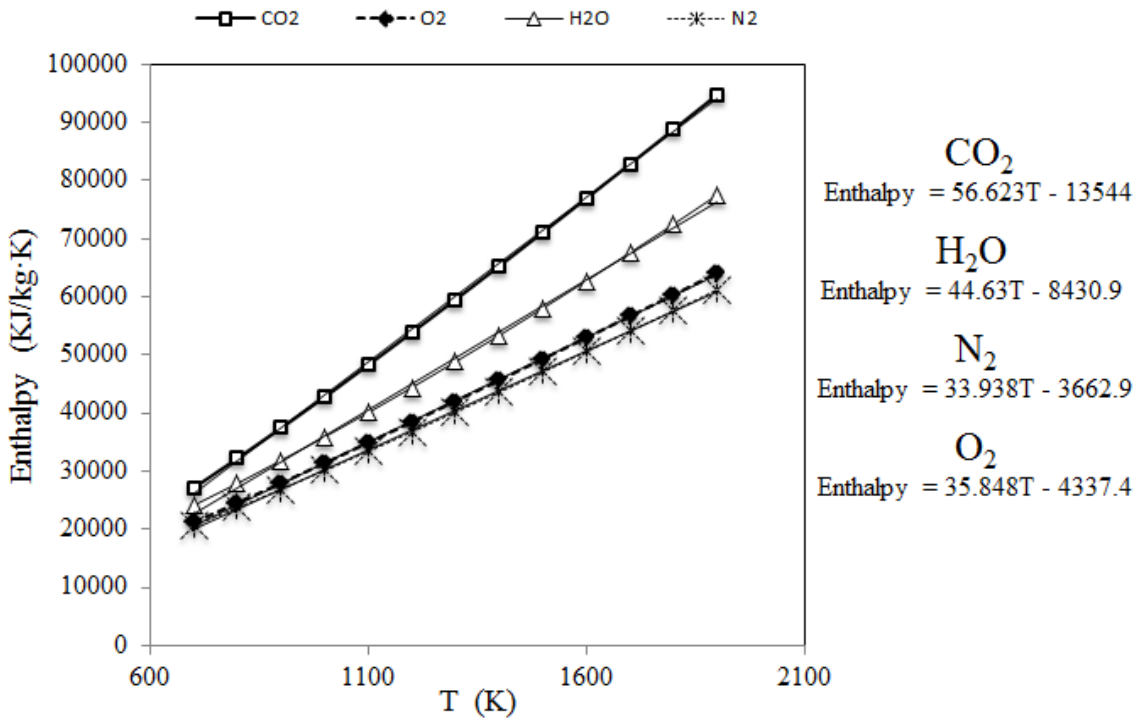

Figure B. 1. Curve fitting of the enthalpy of different gases.

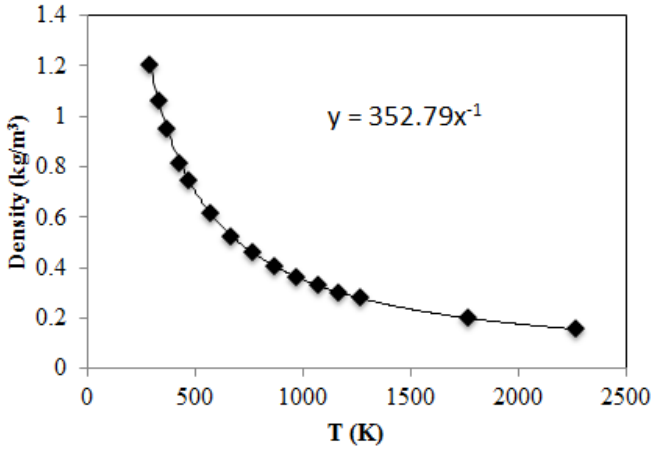

Figure B. 2. Curve fitting of the density of air.

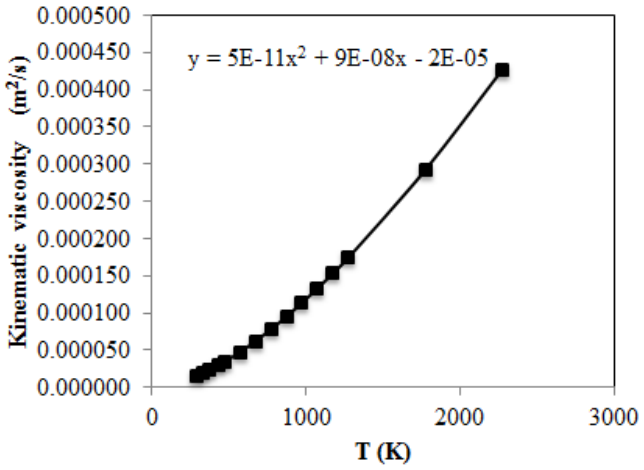

Figure B. 3. Curve fitting of the kinematic viscosity of air.

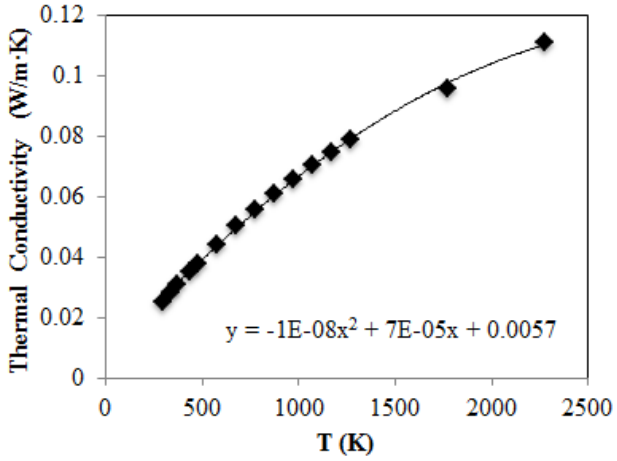

Figure B. 4. Curve fitting of the thermal conductivity of air.

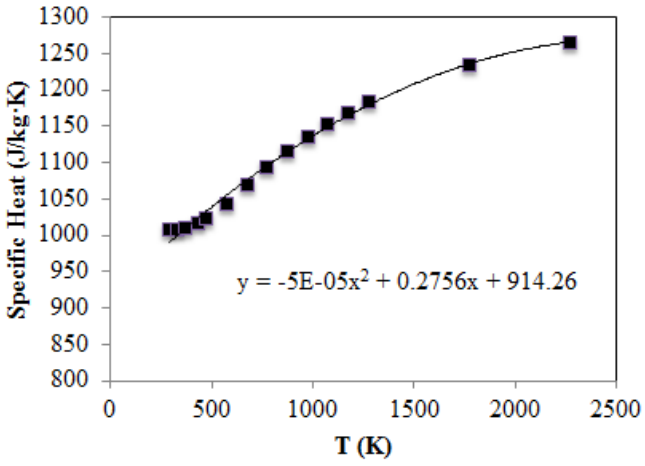

Figure B. 5. Curve fitting of the specific heat of air.